Print edition ISSN 2615-5109
Electronic edition ISSN 2621-0541

Publisher:
Center of Technology, Fakultas Teknik, Universitas Hasanuddin

Address:
Engineering Faculty Campus, Hasanuddin University
Jl. Poros Malino km. 6, Bontomarannu
Kabupaten Gowa, Sulawesi Selatan, Indonesia, 92171
Email : epi-ije@unhas.ac.id
Website : cot.unhas.ac.id/journals/index.php/epiije
Telp/Fax : +62-(0)411-58601

EPI International Journal of Engineering
Editorial Board

Foreword

It is our pleasure to introduce Volume 8, Number 1, February 2025 of the EPI International Journal of Engineering (EPI-IJE). This edition presents a collection of insightful studies that reflect the dynamic progress of engineering research and its growing relevance in addressing real-world challenges. The contributions in this issue demonstrate how diverse engineering approaches continue to evolve, providing innovative solutions across multiple domains.

The papers featured in this volume explore a wide range of topics with practical and theoretical significance. From the evaluation of indoor thermal comfort in tropical university classrooms to the application of computational fluid dynamics in optimizing drying machine performance, the issue highlights how engineering methodologies can enhance both human well-being and industrial efficiency.

Further contributions examine critical aspects of mining and energy systems, including the analysis of fuel consumption in articulated dump trucks influenced by haul road geometry, as well as the preliminary design of mobile floating structures for offshore wind turbines—an emerging solution with strong potential for renewable energy development in Indonesia.

Advancements in structural and industrial engineering are also presented. One study focuses on optimizing the vibrational performance of quasi-isotropic rectangular plates, offering valuable insights for structural design and materials engineering. Another addresses supply chain challenges through inventory model simulation, aiming to reduce the bullwhip effect and improve overall system stability and efficiency.

Collectively, these studies reflect the breadth of contemporary engineering research and its crucial role in supporting sustainable development and technological innovation. We extend our sincere gratitude to all authors, reviewers, and contributors whose dedication has made this publication possible. It is our hope that this issue will inspire further exploration, collaboration, and advancement within the global engineering community.

Sincerely,

Dr. Faisal Mahmuddin
Editor-in-Chief of EPI-IJE

TABLE OF CONTENTS

EPI International Journal of Engineering
Volume 8, Number 1, February 2025, pp. 1-8
DOI: 10.25042/epi-ije.022025.01

*p*ISSN 2615-5109
*e*ISSN 2621-0541

The Assessment of Indoor Thermal Comfort of University Classrooms in Hot and Humid Areas

Rahmi Andarini[a,*], Muhammad Dzaky Al-Haidar[b], Vincentius Rayza Lee[c]

[a]Engineering Physics Department, Faculty of Engineering and Informatics, Universitas Multimedia Nusantara.
Email: rahmi.andarini@lecturer.umn.ac.id
[b]Engineering Physics Department, Faculty of Engineering and Informatics, Universitas Multimedia Nusantara.
Email: muhammad.dzaky1@student.umn.ac.id
[c]Engineering Physics Department, Faculty of Engineering and Informatics, Universitas Multimedia Nusantara.
Email: vincentius.rayza@student.umn.ac.id

Abstract

Thermal comfort is a description of the mental satisfaction experienced by humans regarding the temperature conditions in the surrounding environment. Appropriate thermal comfort conditions will have a positive influence on the occupant such as increasing productivity. This research was carried out to determine the level of thermal comfort in classrooms of the Universitas Multimedia Nusantara. There are two methods applied in this study: firstly, by measuring indoor air quality parameters, and the second method is by surveying the occupants' acceptance of the indoor air condition. The measurement of indoor air parameters consists of two different methods those are by installing Internet of Things monitoring systems and manual measurement. There were 2 classrooms and 1 student lounge surveyed, and the measured parameters were indoor air temperature and relative humidity. The results of the measurements show that the average indoor air temperature of the conditioned classrooms was 26^{O}C and the average temperature of the student lounge during unconditioned was 29^{O}C. In the same condition, the measured relative humidity in the classrooms was found to be 55%, and the student lounge was at 70%. Regarding the thermal comfort condition, 68% of occupants of the Student Lounge felt just comfortable, 17% felt very comfortable, and 15% felt uncomfortable. The opinion regarding this choice is affected by the sitting position of the respondents. In classrooms D1509 and D1510, 64% of the respondents felt just comfortable, 28% felt very comfortable, and 8% felt uncomfortable, meaning that most of the respondents felt comfortable.

Keywords: Indoor air condition; measurement; thermal comfort

1. Introduction

A university is a formal educational institution that functions as a means of creating a generation that has knowledge, attitudes, and skills. Apart from preparing learning that is appropriate to educational institutions, universities must provide conducive and comfortable learning spaces that comply with Indonesian National Standards [1]. Several aspects that can be considered before creating a comfortable classroom consist of comfort, flexibility, and the use of communication technology. Aspects like this are essential in order to increase the effectiveness of learning in the classroom [2].

Thermal comfort is a state of mind and satisfaction that can be expressed in a thermal or comfortable state in the surrounding environment. This means that thermal comfort is greatly influenced by human conditions and their environment. Clothing and activities are the main human factors that determine the thermal comfort conditions in a room. Meanwhile, the environment has several factors such as: air temperature, relative humidity of the air flow, and surface temperature [3].

Thermal comfort refers to the subjective satisfaction or dissatisfaction of an individual with the thermal environment they are in. Each person has their own unique preferences and tolerances for thermal conditions around them. In recent years thermal comfort has been emphasized as one of the important factors when planning or maintaining a building. Especially in educational settings, providing optimal thermal comfort plays an important part in ensuring students' productivity and concentration [4].

The impact of thermal comfort cannot be neglected. It can affect various aspects such as productivity, concentration, and the wellbeing of an individual. Indoor air quality has become very important considering that the majority of our time is spent indoors, and especially for the education sector, indoor air quality conditions can affect student stress levels [5]. Previous research showed that when people are in a thermally comfortable environment, their performance, concentration, and productivity increase. The incapability to provide a thermally comfortable environment can lead to

*Corresponding author. Tel.: +62-812-3300-726
Engineering Physics, Universitas Multimedia Nusantara, Tangerang, Indonesia, 15810

discomfort, reduced productivity, concentration, and performance, and can cause health issues such as fatigue and stress [6].

Maintaining conducive and comfortable conditions is an essential factor of a university environment, specifically the thermal comfort condition of the classrooms, as indoor comfort condition has a significant impact on users' health, productivity, and psychology [7] [8]. Factors that can maintain conducive and comfortable indoor conditions are the buildings' indoor air condition that comply with Indonesian National Standards and installing artificial cooling, such as air conditioning system and mechanical ventilation [2]. The air conditioning system must satisfy the occupants' thermal comfort requirement [9], which is recommended by the Indonesian National Standard [10], that the indoor air temperature is maintained at 25.5ºC ± 1.5ºC and relative humidity of 60% ± 5%. The recommendation for indoor air conditioning is shown in Table 1.

The American Society of Heating, Refrigerating, and Air-Conditioning Engineers developed the standard for thermal environmental conditions, known as ASHRAE Standard 55. A method used to calculate and assess the thermal comfort level experienced by occupants in a particular environment, such as inside a room or building, and following set by ASHRAE Standards [3]. This standard establishes guidelines for indoor thermal comfort parameters, such as temperature, humidity, air speed, and other factors.

ASHRAE also provided a psychrometric chart that can be used to analyze the relationships between various properties of air, including temperature, humidity, and enthalpy. By utilizing the psychrometric chart [12] it can determine whether the thermal conditions in a room or building are within the acceptable comfort level, as shown in Fig. 1.

Table 1. Recommendation of indoor air condition [11]

Category	Air Temperature (TE)	Relative Humidity (RH)
Cool Comfortable	20.5^{O}C – 22.8^{O}C	50 %
Upper Threshold	24^{O}C	80 %
Comfortable	22.8^{O}C – 25.8^{O}C	70 %
Optimal Upper Threshold	28^{O}C	
Warm Comfortable	25.8^{O}C – 27^{O}C	60 %
Optimal Upper Threshold	31^{O}C	

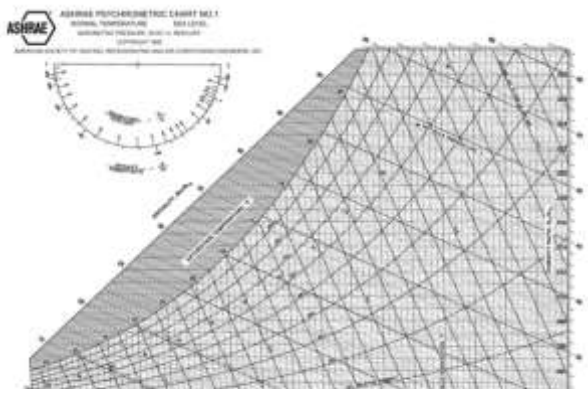

Figure 1. Psychrometric chart

Predicted Mean Value (PMV) is a method used to calculate and assess the thermal comfort level experienced by occupants in a particular environment, such as inside a room or building. PMV models take into account various factors, including air temperature, relative humidity, air velocity, activity level, radiant temperature, clothing insulation, and personal presence. This index used a scale ranging from -3 to +3, where negative values indicate a feeling of cold and the positive value indicates a feeling of warmth a person felt. The PMV model can predict the average thermal sensation felt by a group of people and determine the Predicted Percentage of Dissatisfied (PPD). Predicted Percentage of Dissatisfied is the prediction of the percentage of people who feel dissatisfied with the condition of the room [13].

The indoor air condition of Universitas Multimedia Nusantara has already been monitored in some places such as the library [14], classrooms and corridors [15] using the Internet of Things (IoT). The monitored parameter consists of indoor air temperature, relative humidity and CO_2 level. The developed intelligent system consists of several components, namely: Internet of Things (IoT) based sensors and smart thermostat using ESP32 board, MQTT broker using Raspberry Pi 4 board, MERN (MongoDB, Express JS, React JS and Node JS) Stack, and intelligent controller. In this stage, the system functions to monitor the condition of the room and its environment.

This research was carried out by taking manual measurements of the classrooms that have been installed in the monitoring system and distributing questionnaires to occupants of the classrooms. The measurement of indoor air conditioning was carried out in 3 (three) classrooms, namely D1509, D1510, and Student Lounge. The results of measurement will be compared to those of monitoring system values to ensure that the data logged by the monitoring system are accurate. The occupants' survey was carried out to confirm that the indoor thermal condition of the classrooms was acceptable.

The objective of this research is to assess the indoor air condition of classrooms of Universitas Multimedia Nusantara and to gather the occupant satisfaction level regarding indoor air condition. The occupant survey results regarding the comfort levels in the classrooms will be compared with the measured parameters.

2. Method

The methods applied in this research consist of 3 (three) main activities, such as

- measuring indoor air condition parameters (temperature and relative humidity) of the classrooms
- comparing the measured parameter with the data collected by the monitoring system with the purpose to ensuring that the data collected by the monitoring system are accurate
- Conducted occupant survey by distributing an electronic questionnaire to the students who previously had lectures in the classrooms of D1509, D1510, and Student Lounge.

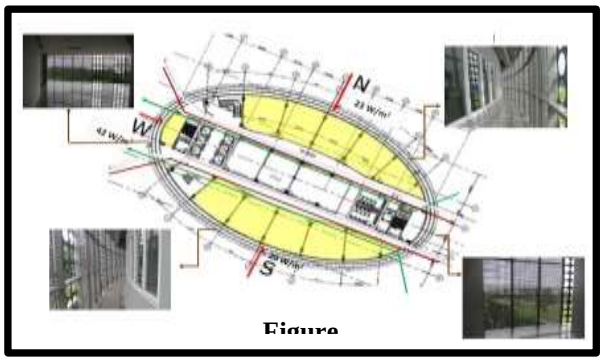

Figure 2. The layout of classrooms at the 15th level of Building D Universitas Multimedia Nusantara

2.1. Characteristics of the classrooms

The location measurement was carried out in the classrooms on the fifteenth floor of Building D of Universitas Multimedia Nusantara, as shown in Fig. 2. The building's mass orientation is designed by considering the sun's trajectory, which is how sunlight affects the building. Hence, solar radiation can be reduced. The shape of the building is an ellipse, and the outside wall is a double façade.

The air conditioning system for Building D uses a centralized chiller, which serves the needs of Building D. However, there is a thermostat installed in each classroom. Hence, the occupant is still able to turn the AC off or on as needed. In addition, the occupant can still set the air temperature and the fan speed. Usually, the AC will be on when there is a lecture in the classrooms, specifically for the Student Lounge, as shown in Fig. 3; it often functions as an event room, such as events by student organizations or lecturers' frequent meetings.

The measurement process and occupants' survey in the Student Lounge were carried out both when the room was conditioned and unconditioned. However, due to the low occupancy of the Student Lounge, most of the indoor air conditioning measurements were taken while the room's air conditioning was off. As the occupants' survey was performed using an e-questionnaire, therefore the respondents were still able to answer outside the measurement time.

Student Lounge is located in the middle of the 15th floor. The west and east walls are made of glass. The length, width, and height of the Student Lounge are 7.5 meters, 25.5 meters, and 3.5 meters, respectively.

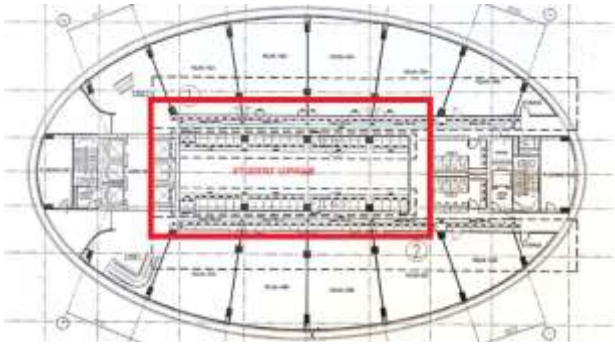

Figure 3. Location of student lounge

Figure 4. Interior condition of student lounge

Figure 5. Points of measurement of student lounge

The total room area is 191.25 m^2, with a capacity of occupants of up to 100 students. The interior condition of the Student Lounge is shown in Figure 4. It can be seen that there is still a possibility of maximizing the use of natural lighting in the Student Lounge even though it is located in the middle of the floorplan.

There are two points of sensors of the monitoring system in the Student Lounge. They are installed in the front and back sides of the room. This monitoring system measured the indoor air temperature, relative humidity, and carbon dioxide level. The monitoring system logs the data every five minutes.

The measurement points of the Student Lounge are shown in Figure 5. There are 6 (six) points of measurement of Student Lounge, namely points A, B, C, D, E, and F. For every point, 10 (ten) measurements were carried out.

The classrooms D1509 and D1510 are located on the southwest side of the building, as depicted in Fig. 6. The dimensions of rooms D1509 and D1510 are 11 meters long by 7.5 meters wide by 3.5 meters high. There are windows on the south side and a glass wall on the north side. Hence, these classrooms have the opportunity to maximize natural lighting entering the rooms. The capacity of each room is 40 students.

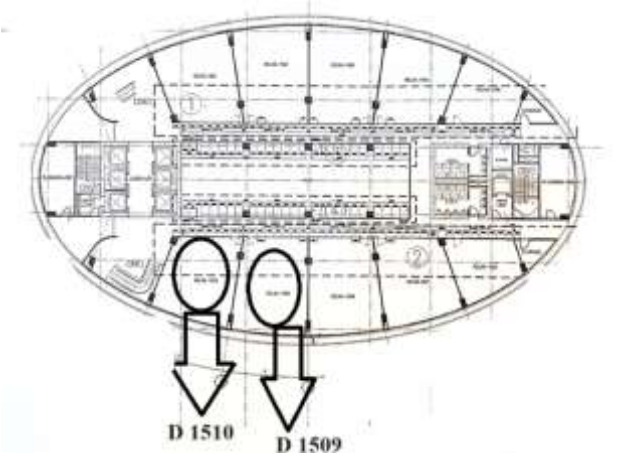

Figure 6. Position of classroom D1509 and D1510

Figure 7. Interior Condition of Classrooms D1509 and D1510

The interior condition of classrooms D1509 and D1510 is shown in Figure 7. The monitoring system is attached to the ceiling, in the front side of the classroom.

The measurement points of classrooms D1509 and D1510 are shown in Figure 8. There are 4 (four) points of measurement in each classroom, namely points A, B, C, and D. For every point, there were 10 (ten) indoor air temperature and relative humidity measurements carried out. The measurements and occupant survey were done while the rooms' air condition was on and the setting temperature was 24^{O}C.

2.2. Monitoring System

The monitoring system that utilizes the DHT22 temperature and humidity sensor, which is a digital temperature and humidity sensor [15]. To monitor the condition of CO_2 levels, the type of CO_2 sensor used is MH-Z19B, which is an infrared gas sensor module. The circuit of monitoring system is depicted in Fig. 9.

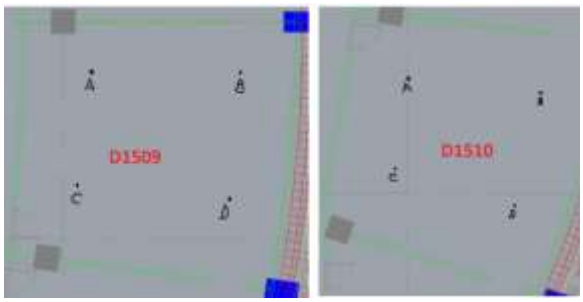

Figure 8. The measurement points of D1509 and D1510

Figure 9. Monitoring system

Figure 9. Calibration

Prior to the installation of the monitoring system, the calibrations were performed in order to ensure that the system worked properly. The calibration method applied was by comparing the reading of the calibrated room thermometer and hygrometer. For the CO_2 level, the type of the sensor is self-calibrating sensor. Figure 9 shows the calibration for temperature and relative humidity sensors.

The calibrations were carried out during 72 hours, with the data logged every 10 minutes. Figure 10 shows the calibration results of temperature and relative humidity sensors. There were 10 sensors calibrated, and the results shows that the sensors work properly and demonstrate similar results of reading. According to previous research [16], the characteristic of DHT22 sensor shows that the allowable average error is 3% for relative humidity and 2.3% for temperature or $\pm$ 5^{O}C.

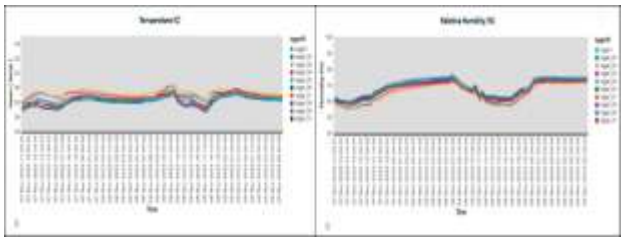

Figure 10. The calibration result

Figure 11. The position of monitoring system [15]

The circuit of the monitoring system is installed at the ceiling with the reason of being close to the electric plug and for security reasons.

2.3. Occupant survey

Occupants' survey was performed with the purpose to confirm the occupant's acceptance regarding the thermal comfort condition of the classrooms. The questionnaire consists of several question such as

- Gender – Male/Female
- Age - < 18 years; 18-25 years; >25 years
- Duration in the classrooms - < 1 hour; 2-3 hours, > 4 hours
- The position of the occupant during in the classroom (select the point)
- The impression regarding indoor temperature condition (-3 = cold; -2 = cool; -1 = slightly cool; 0 = neutral; +1 = slightly warm; +2 = warm; +3 = hot)
- The impression regarding relative humidity (-2 = very dry; -1 = dry; 0 = neutral; +1 = humid; +2 = very humid)
- Overall, how is the occupant's impression regarding the indoor thermal comfort (very comfortable – just comfortable – uncomfortable)

The target respondents for this survey were the students who had experience staying in the selected classrooms within the month of February until May 2024. The e-questionnaire was distributed so that it would be more flexible for the respondent to answer the questions. Some assumptions taken into consideration were consists of clothing value and respondents' activity. The dress worn by the occupants is a casual dress (trousers, short-sleeve shirt) with the clothing value of 0.57 [3]. As most of the respondents are students, light activity it is considered as reading and seated with a metabolic rate of 1.0 met [3].

3. Results and Analysis

3.1. Measurement of indoor air condition

The results of the measurement of indoor air parameters of the Student Lounge during unconditioned, as depicted in Fig. 13, show that the indoor temperature ranges between 28.4ºC to 29.5ºC, and the relative humidity was between 71.9 – 73.9%.

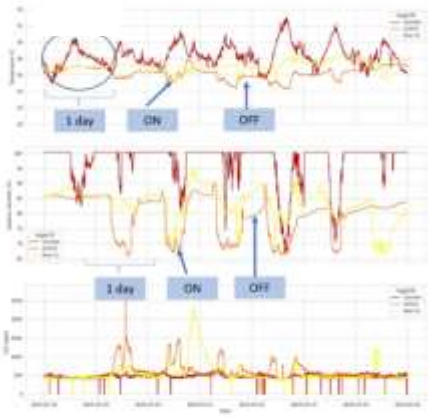

Figure 13. The results of monitoring systems

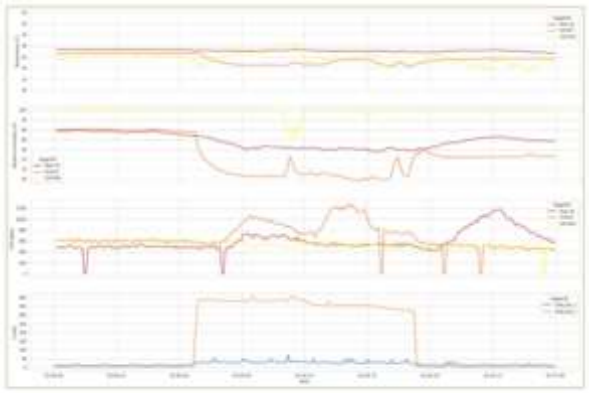

Figure 14. The data logged resulted by monitoring system

In the classrooms, it is found that the indoor temperature ranges between 25.69^{O}C to 26.43^{O}C and relative humidity was between 48.42% to 60.34%.

Figure 14 shows that during unconditioned, the temperature of Student Lounge was constant at 27^{O}C throughout the day and the relative humidity was 80%. The air temperature in the classrooms reported at the average of 24.5^{O}C and the relative humidity of 65%.

During occupied hours where the air conditioned was on, the average indoor air temperature of the Student Lounge was reported at 24^{O}C and the relative humidity of 68% as depicted in Fig. 14. The temperature of the classrooms was around 25^{O}C and relative humidity was between 60% to 75% when there was activity in the classrooms.

From the results of the comparison between data logged by the monitoring system and manual measurement, it is found that there is a 1-2OC difference in indoor air temperature conditions. This difference is still below the allowable error range of 5^{O}C, which means that the data logged by the monitoring system is acceptable [16]. For the relative humidity, there is a 4% difference or 1% higher than that of the sensor data sheet's allowable error range. The difference that occurs between measured data and logged data by the monitoring system is most probably caused by the position and the number of measurement points. There are only two monitoring system sensors installed in the Student Lounge, whereas there are four measurement points. In addition, the position of the sensor is also different. The sensor of the monitoring system is located at a height of about 3.5 m from the floor, and the sensor of the manual environment meter was about 1 m. This situation has also occurred during the measurement process of classrooms D1509 and D1510.

3.2. Occupants' Survey

- Student Lounge

The number of people who answered the survey was 47 respondents, which consists of 33 males (70%) and 14 females (30%). The age of all respondents ranged between 18 and 25 years old. From the survey result, there are 33 respondents who usually stay inside for 2 to 3 hours, 6 respondents stay for 1 to 2 hours and 8 respondents stay more than 4 hours. This finding supports the previous statement that the room is usually functioned as a meeting room or seminar venue.

The likert scale is very useful in determining how or on what scale a person feels regarding the indoor air temperature and relative humidity conditions.

Figure 12 and 13 show the Likert scale of the occupants' impression regarding the indoor air temperature condition. 13 respondents felt slightly cool (-1), and 13 respondents chose neutral (0). There are 10 respondents agreed that the indoor air temperature was slightly warm, 8 respondents felt slightly cool and only 2 respondents felt warm.

Regarding the condition of relative humidity, based on survey results that graphed in Figure 13, most of the respondents felt neutral (0). That is, 33 respondents (70%), 4 (9%) felt dry (-1), and 4 people (9%) felt very dry (-2). There are 5 people (11%) felt humid (+1), and only 1 person felt very humid (+2).

The average temperature and humidity levels, according to the survey, are -0.3 and -0.1, respectively. This means that the occupants felt slightly cool and slightly dry. According to the ASHRAE standard, this value is within the comfort level.

Figure 14 shows that 68% of occupants of the Student Lounge felt just comfortable,17% felt very comfortable, and 15% felt uncomfortable. The opinion regarding this choice is affected by the sitting position of the respondents.

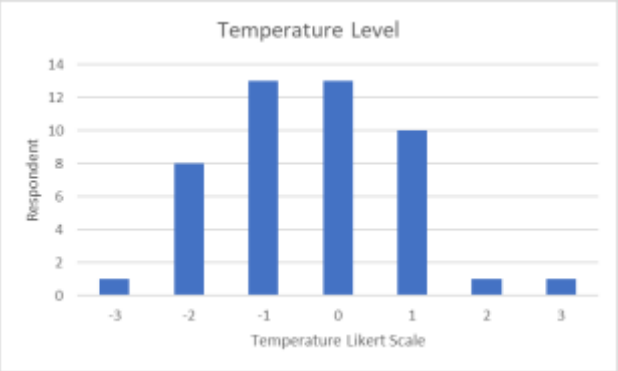

Figure 12. The number of respondent vs impression on the indoor air temperature of student lounge

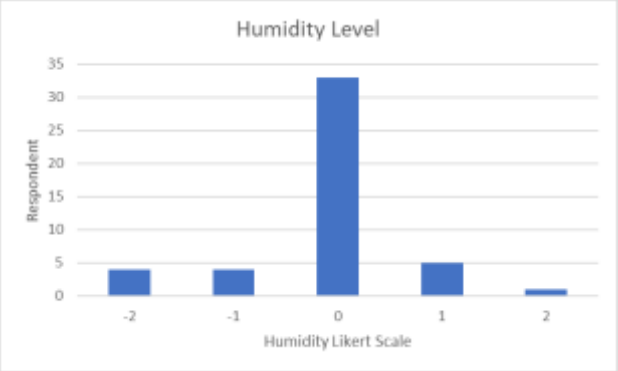

Figure 13. The number of respondent vs impression on the relative humidity of student lounge

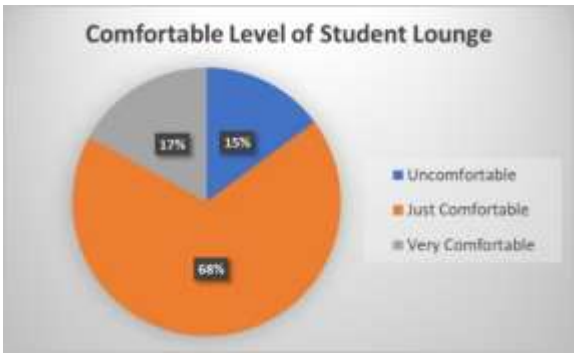

Figure 14. Percentage of comfort level of the occupants of student lounge

Figure 15. Sitting position at student lounge

Figure 16. The sitting position vs comfortable level

The sitting position of the respondents at the Student Lounge is depicted in Figure 15. There 4 (four) segments that define the sitting area. The respondents were asked about their position during their activity in the Student Lounge.

Referring to Figure 16, it can be seen that the most "very comfortable" area is area B, followed by area D, and uncomfortable sitting position is area A. This situation occurs most probably caused by the position of area B and area D are the closest position from the entrance doors, of which according to the average PMV, indoor air condition of Student Lounge is cold and dry, thus, area near the entrances will be slightly warmer as the outdoor of Student Lounge is unconditioned.

Figure 17 shows the Likert scale of the occupants' impression regarding the indoor air temperature condition of classrooms D1509 and D1510. There are 24 respondents felt cool (-2) and 19 respondents choose slightly cool (-1). There are 6 respondents felt neutral (0) and 1 person agreed that the room was cold also 1 person felt hot.

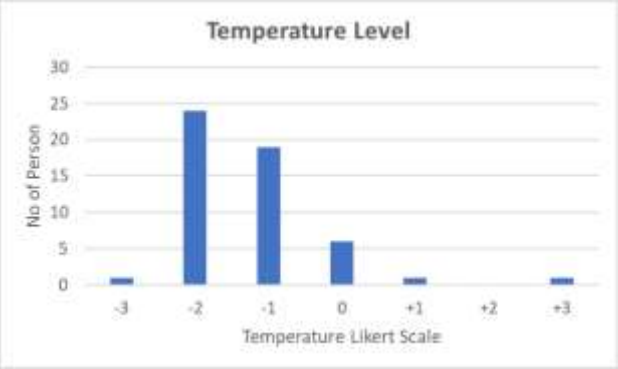

Figure 17. The number of respondents vs impressions on the indoor air temperature of Classrooms D1509 and D1510

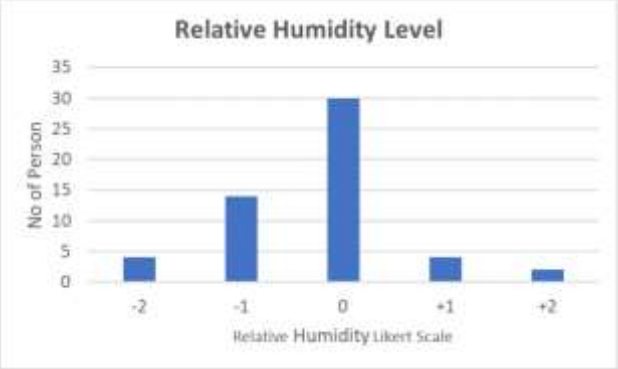

Figure 18. The number of respondent vs impression on the relative humidity of Classrooms D1509 and D1510

According to the survey results related to the relative humidity, graphed in Figure 18 shows that most of the respondents felt neutral (0) that is 30 respondents (56%), 14 (26%) felt dry (-1) and 4 person (7%) felt very dry (-2) and humid, each. There are only 2 person (4%) felt very humid (+2).

Figure 19 shows that 64% of occupants of classrooms D1509 and D1510 felt just comfortable, 28% felt very comfortable, and 8% felt uncomfortable. There was no further observation regarding the seating position of the occupants of the classrooms.

Based on the PMV analysis, the average temperature and humidity levels according to the survey are -1.2 and -0.2, respectively. This means that the occupants felt cold and slightly dry.

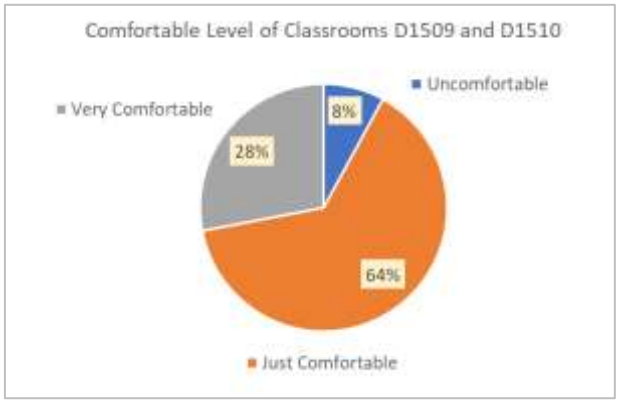

Figure 19. Percentage of Comfort Level of the Occupants of Classrooms D1509 and D510

4. Conclusion and Recommendation

There are some points that can be concluded from the analysis of the results of indoor air condition measurements and occupants' survey:

- From the results of the comparation between data logged by monitoring system and manual measurement, it is found that there is 1-2^{O}C difference of indoor air temperature condition. This difference is still below the allowable error range of 5^{O}C, which means that the data logged by monitoring system is acceptable. For the relative humidity, there is 4% difference or 1% higher than that of sensor data sheet's allowable error range. The difference occurs between measured data and logged data by monitoring system most probably caused by the position and the number of measurement points.
- The average temperature and humidity level according to the occupants' survey at Student Lounge are -0.3 and -0.1, respectively. This means that the occupants felt cold and dry. According to the ASHRAE standard this value is within the comfortable level.
- Regarding the thermal comfort condition, 68% of occupants of Student Lounge felt just comfortable, 17% felt very comfortable and 15% felt uncomfortable. The opinion regarding this choice is affected by the sitting position of the respondents. At the classrooms D1509 and D1510, 64% of the respondents felt just comfortable, 28% felt very comfortable, while only 8% felt uncomfortable. It can be concluded that the majority of the respondents felt comfortable.
- Based on PMV analysis, the average temperature and humidity level according to the survey at Classrooms D1509 and D1510 are -1.2 and -0.2, respectively. This means that the occupants felt cold and slightly dry which shows the temperature condition is considered uncomfortable.

Based on the abovementioned conclusion, it is recommended to add more sensors installed in the rooms so that the results of monitoring systems are more accurate. It is also important to conduct measurements on the CO2 level and compare it to the results of the monitoring system, as this parameter is also significant in determining the indoor comfort level.

Acknowledgements

This research was facilitated under the Merdeka Belajar Kampus Merdeka program and the development of monitoring system was funded by Universitas Multimedia Nusantara through the Internal Research funding Scheme of Universitas Multimedia Nusantara.

References

[1] S. Fatmawati, N., Mappincara, A., & Habibah, "Pemanfaatan Dan Pemeliharaan Sarana Dan Prasarana Pendidikan. (studi kasus SMP Negeri 7 Makassar)," *). J. Ilmu Pendidik. Kegur. dan Pembelajaran*, vol. 3, no. 2, pp. 115–121, 2019, [Online]. Available: https://ojs.unm.ac.id.

[2] M. Muhaimin, "Urgensi Kenyamanan Termal dalam Perspektif Pembelajaran," *Geodika J. Kaji. Ilmu dan Pendidik. Geogr.*, vol. 7, no. 1, pp. 23–32, Jun. 2023, doi: 10.29408/geodika.v7i1.6451.

[3] ASHRAE, "ANSI/ASHRAE Standard 55-2017 : Thermal Environmental Conditions for Human Occupancy," *ASHRAE Inc.*,

vol. 2017, p. 66, 2017.
[4] S. Yarramsetty, N. S. Deka, and M. V. N. Siva Kumar, "Adaptive lighting comfort in the classrooms of educational building and student hostel rooms," *E3S Web Conf.*, vol. 170, no. September 2019, 2020, doi: 10.1051/e3sconf/202017001012.
[5] Z. S. Zomorodian, M. Tahsildoost, and M. Hafezi, "Thermal comfort in educational buildings: A review article," *Renew. Sustain. Energy Rev.*, vol. 59, pp. 895–906, 2016, doi: 10.1016/j.rser.2016.01.033.
[6] A. Vasilev, R. A. Angelova, and R. Velichkova, "Methods for personal cooling in hot environment used in clothing and wearables," *E3S Web Conf.*, vol. 327, 2021, doi: 10.1051/e3sconf/202132703003.
[7] S. S. Y. Lau, J. Zhang, and Y. Tao, "A comparative study of thermal comfort in learning spaces using three different ventilation strategies on a tropical university campus," *Build. Environ.*, vol. 148, pp. 579–599, 2019, doi: 10.1016/j.buildenv.2018.11.032.
[8] G. Papadopoulos, G. Panaras, and E. Tolis, "Thermal comfort and Indoor Air Quality assessment in university classrooms," *IOP Conf. Ser. Earth Environ. Sci.*, vol. 410, no. 1, 2020, doi: 10.1088/1755-1315/410/1/012095.
[9] R. Andarini, M. Widjaja, and D. K. Halim, "Evaluation of Indoor Air Condition of University Building in Tropics using Building Thermal Modeling," *2021 2nd Int. Conf. Smart Cities, Autom. Intell. Comput. Syst.*, pp. 52–57, Oct. 2021, doi: 10.1109/ICON-SONICS53103.2021.9617192.
[10] Standar Nasional Indonesia, "SNI 03 6572 2001 Tata Cara Perancangan Sistem Ventilasi dan Pengkondisian Udara pada Bangunan Gedung," *Tata Cara Peranc. Sist. Vent. dan Pengkondisian Udar. pada Bangunan Gedung*, pp. 1–55, 2001.
[11] Standar Nasional Indonesia, "Tata Cara Perancangan Sistem Ventilasi dan Pengkondisian Udara pada Bangunan Gedung," *Sni 03 - 6572 - 2001*, pp. 1–55, 2001.
[12] ASHRAE, *ASHRAE fundamentals (SI)*. 2017.
[13] W. Van Der Linden, M. Loomans, and J. Hensen, "Adaptive thermal comfort explained by PMV," *Indoor Air*, no. January 2008, p. 8, 2008.
[14] M. Widjaja, D. K. Halim, and R. Andarini, "The Development of an IoT-based Indoor Air Monitoring System Towards Smart Energy Efficient Classroom," *Ultim. Comput. J. Sist. Komput.*, vol. 14, no. 1, pp. 28–35, 2022, doi: 10.31937/sk.v14i1.2565.
[15] R. Andarini, M. Widjaja, and A. Djajadi, "Pemantauan Kualitas Udara dalam Ruang Kelas Berbasis Internet of Things dan Evaluasi Kinerja Energi Sistem Tata Udara di Universitas Multimedia Nusantara," 2023.
[16] F. Puspasari, T. P. Satya, U. Y. Oktiawati, I. Fahrurrozi, and H. Prisyanti, "Analisis Akurasi Sistem Sensor DHT22 berbasis Arduino terhadap Thermohygrometer Standar," *J. Fis. dan Apl.*, vol. 16, no. 1, pp. 1–6, 2020.

EPI International Journal of Engineering
Volume 8, Number 1, February 2025, pp. 9-14
DOI: 10.25042/epi-ije.022025.02

*p*ISSN 2615-5109
*e*ISSN 2621-0541

Computational Fluid Dynamic Analysis on Double-Type Drying Machine Design

Waleed[a], Mona Nur Moulia[b,*], Athoillah Azadi[c]

[a]Department of Agricultural Crop Technology, Indonesian Agricultural Engineering Polytechnic. Email:waleedibra2020@gmail.com
[b]Department of Agricultural Crop Technology, Indonesian Agricultural Engineering Polytechnic. Email: mouliamona@gmail.com
[c]Department of Agricultural Mechanization Technology, Indonesian Agricultural Engineering Polytechnic. Email:athillah.azadi@gmail.com

Abstract

The design of a double-type dryer with tray and rotary will be designed to be able to dry chips and grains commodities in one time process for energy and time-saving. In the designing process, Computational Fluid Dynamic (CFD) simulation is used to analyze the distribution of hot air and minimize failures in the design. The purpose of this study was to determine the pattern of hot air flow distribution and determine the best design of the drying machine. The parameters used in the CFD input have a temperature of 60 ^{o}C, air velocity 1 m/s, and a pressure 1.01325 bar with a constant time. This study used 2 treatments, namely the outlet position parameter (A) with dimension 60 mm x 60 mm and the number of holes in the bulkhead between the tray and rotary have the gap type (L) with dimension 540 mm x 70 mm with a total of 21 treatments. This research begins with pre-processing for made geometry and boundary condition input, next is solver process with average iterations 298 with 36 s interval, and the last is post-processing for having air contour. The results showed that the best treatment based on temperature pattern is the A2L1L2 treatment, with the output A2 and 2 limiting gaps, on gaps 1 and 2. This treatment had an average temperature distribution of 56.69 ^{o}C, deviation 3.55 ^{o}C, air velocity 1.57 m/s, and turbulence 0.021 m/s.

Keywords: CFD; drying; rotary; tray

1. Introduction

Post-harvest processes in agricultural products that play an important role in maintaining product shelf life by reducing mositure content through the drying process. Highest moisture content in the products will cause the products to be susceptible to microorganisms and spoilage [1]. The farmers usually use manual drying with the open sun drying and mechanical drying using a dryer machine.

Drying machines commonly used are trays for drying chips and rotary types for grain. Tray dryer usually have a disadvantage, the process of distributing hot air that is not evenly distributed just tray near with the heater and caused change the tray position. The rotary dryer can only dry certain types of products, but the distribution of hot air produced is evenly distributed over the entire surface of the dried material.

Based on these problems, a dryer is designed that has a dual system that can dry materials with different characteristics in one machine to save time and save energy in the process. The dryer is design have two parts, the top is a rotary and the bottom is a tray. The process of the flow of hot air that is exhaled will flow to thectray and then be directed to the top for the rotarydryer and then exit at the outlet.

The drying machine design process consists of design, simulation, and manufacturing stages. The simulation process plays an important role in the drying machine design process, because the simulation aims to optimize the work and distribution of airflow in the drying chamber which spreads to all parts of the machine to be more efficient and effective and minimize failures in the process [2]. The analysis used to determine the distribution of hot air and fluid distribution is Computational Fluid Dynamics (CFD) analysis because the visualization results can be easily interpreted by researchers [3]. CFD simulation on the drying machine is very necessary to know the environmental conditions and the contours of the hot air in the design of the drying machine, especially for drying food [4]. Airflow distribution simulation has been carried out on a tray-type drying machine using CFD and the analysis is very helpful in the drying machine design process because adjusting the tray position and adjusting the air distribution flow will affect the drying rate [5].

The development of drying technology must continue to be carried out in order to obtain an efficient and effective machine, one of the developments carried out is the development of two types of dryers in one machine. The design of this double-type dryer has a partition that

*Corresponding author. Tel.: +6281373255774
Sinarmas Boulevard Street, Situgadung, Pagedangan Tangerang, Indonesia, 16158

functions to separate the tray and rotary positions. To optimize the temperature distribution from the tray to the rotary, it is necessary to have the right number, position of the gap on the bulkhead and the outlet holes so that hot air is locked for a long time in the chamber before it finally comes out. The purpose of this study was to determine the distribution of hot airflow and the best design for a double-type dryer.

2. Material and Methods

2.1. Experimental set up

This research used SolidWorks 2021 flow simulation software. The machine design have length 1950 mm x 600 mm x 1030 mm (Fig. 1), with silinder diameter 400 mm and length 1120 mm (Fig. 2), and tray length 500 mm x 490 mm x 270 mm (Fig. 3).

The designed process is divided into 3 outlets and 3 gaps positions consists of outlet positions (A) and bulkhead gap (L) (Table 1).

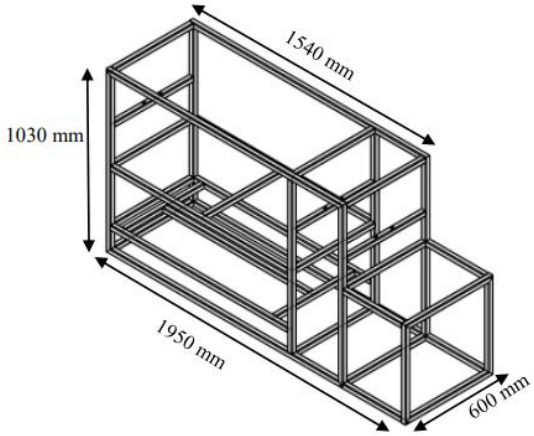

Figure 1. Isometric view machine framework

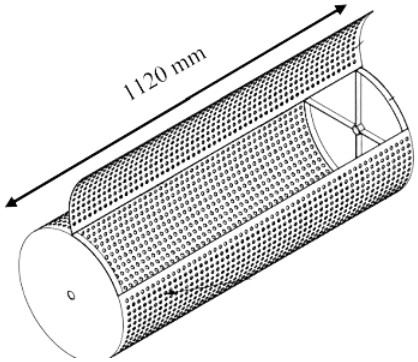

Figure 2. Isometric view silinder

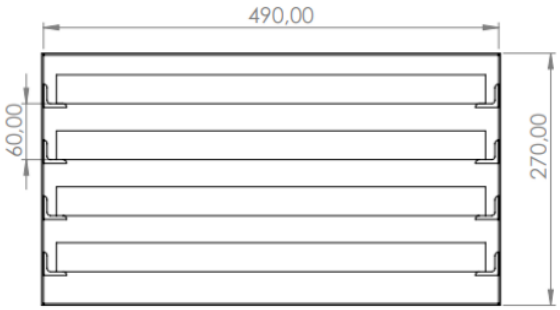

Figure 3. Isometric view tray

Table 1. The process division

Notation	Description
A1	Outlet in the right side
A2	Outlet in the left side
A3	Outlet in the top side
L1	Gap 1
L2	Gap 2
L3	Gap 3

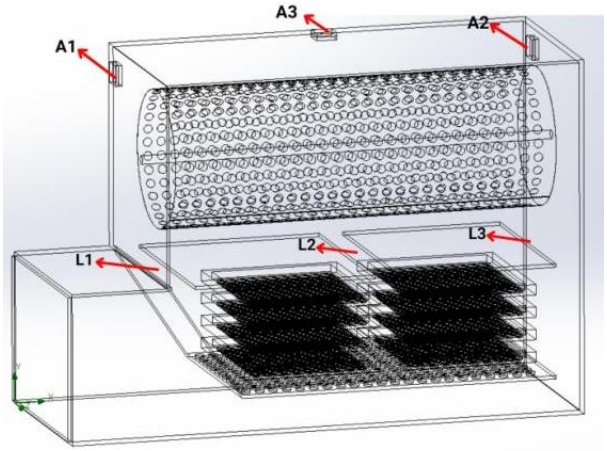

Figure 4. Isometric view machine

The size made with a outlet hole's size 60 mm x 60 mm and with a gap's size 540 mm x 70 mm. The treatment was made as many 21 geometries, according to the treatment made placement outlet is on the side and top of the machine, while the position of the hole is on the side and center of the partition (Fig. 4).

2.2. Mathematical model

Mathematical equation used a navier-stokes equation which consisting of mass, momentum, and energy conservation on fluid flows is [6]:

$$\frac{\partial \rho}{\partial t} + \nabla(\rho \vec{v}) = 0 \quad (1)$$

$$\frac{\partial}{\partial t}(\rho \vec{v}) + \nabla(\rho \vec{v}\vec{v}) = -\nabla\rho + \nabla(\vec{\tau}) + \rho\vec{g} + \vec{F} \quad (2)$$

$$\frac{\partial}{\partial t}(\rho E) + \nabla(\vec{v}(\rho E + \rho)) = \nabla\left(k_{eff}\nabla T\right) + S_h \quad (3)$$

2.3. Boundary condition

The initial temperature input data is 60 ^{o}C with an inlet velocity 1 m/s, and environmental temperature is made with an average temperature of 27 ^{o}C and a pressure of 1,01325 bar. The use of an input temperature of 60 ^{o}C is adjusted to the commodity to be dried simplicia products that contain high volatiles, so that the use of temperatures below 60 ^{o}C is the optimum temperature that can be used [7]. Boundary conditions made consist of 4 parts, namely the inlet velocity on the inlet hot air environmental pressure on the outlet, real wall 1 on the rotary, and real wall 2 on the tray.

2.4. Analysis process

2.4.1. Pre-processing

The first process is the process of making machine geometries, 21 geometries are made according to the geometries made. The next process is to enter data for simulation in the boundary conditions in the form of temperature, pressure, and air velocity. The most important things in the design of the dryer is the initial input conditions in the form of temperature, pressure and fluid velocity which are the keys in a simulation process [8]. The stages after data input are the desired input goals, temperature, velocity, pressure and turbulence. The last stage in preprocessing is meshing and what is used is global mesh.

2.4.2. Solver

The solver or processing stage is the analysis stage of the input data in the process with the equation used until a convergent value or value with the smallest error rate is found, which is called the iteration process. The iteration of the 21 treatments made has an average iteration value of 298 iterations, with the time required for $\pm$ 3 hours with iterations per travel for 36 seconds.

2.4.3. Post-processing

The last stage in the simulation process is to interpret the analysis results into certain images and graphs. The result obtained is in the form of numerical data from variables of fluid properties such as temperature, velocity, and turbulence. The data from the simulation results that have been carried out on the machine produces an image of hot air contours throughout the engine surface, velocity, air contours on the tray, hot air contours on the rotary, and the level of air turbulence when the airflows.

2.5. Simulation condition

The simulation settings parametric are temperature, air velocity, and air turbulence. The parametric of the study in this research is to design the outlet to maximize the temperature inside the drying chamber. The use of air flow velocity and temperature in research using CFD will show the temperature distribution in the drying chamber and it can be used in design improvements [9].

3. Result and Discussion

3.1. Simulation results on the position of the outlet and the gap

The position outlet and the number of gaps will affect the value of temperature distribution, air velocity, and the level of turbulence that occurs in the drying process. The temperature and speed of the inlet and outlet will affect the material being dried from a physical and chemical properties [10]. The average pressure is same because the geometric shape is almost the same, which is 1.06 bar.

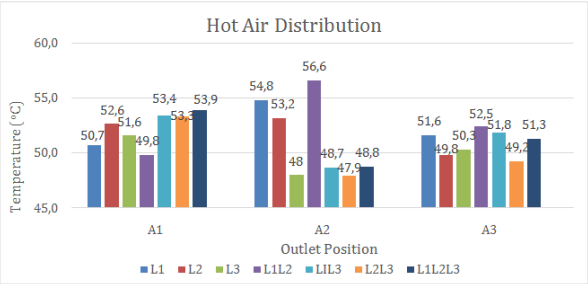

Figure 5. Hot air distribution 21 treatments

3.1.1. Temperature

The results obtained the farther the position of the hole from the outlet, the greater the average value of the temperature distribution in the drying chamber because the hot air will circulate first in the chamber. The distribution of the highest temperature values is in the A2L1L2 sample, namely the disposal of A2 with two gaps opened, namely hole 1 and hole 2 with a value of 56.69 ^{o}C (Fig. 5). Position outlet with the placement of the gap also affects the level of flatness in the drying tray system because the hot air will pass through the tray first and then enter the rotary and then exit at the outlet. The treatment that has the lowest value is the A2L2L3 treatment which produces an average temperature of 47.92 ^{o}C, there is a much different decrease in temperature due to the cold temperature trapped in the dryer (Fig. 5).

The results of the temperature distribution are the key to having the best design for the machine, the distribution of the hot air temperature contour from the simulation results can interpret the plan to have the design (Fig. 6). Based on research [11] in simulations on the design of the dryer, the best result is a design that produces a low-pressure drop, high drying rate, and uniformity of hot air in the dryer.

3.1.2. Velocity

The results show fewer the number of gaps given, the faster the air velocity. This is because the air is not divided and passes through many gaps. The highest air velocity will affect the drying process because hot air will quickly exit the outlet. Increasing the speed of the drying process will cause a decrease in temperature that occurs faster towards the outlet because it is caused by an increase in the rate of evaporation of water [10]. The highest velocity value is shown by the A3L1 treatment with a speed of 2.15 m/s and the treatment with the lowest value is A2L2L3 with a speed of 1.18 m/s. The position of the open hole and its distance from the outlet are factors that influence because it causes the speed value to decrease rapidly.

3.1.3. Turbulence

The results obtained the level of turbulence is directly proportional to the air velocity. The higher air velocity value, the faster the turbulence that occurs. This turbulence occurs because the velocity of the air experiences friction with the inside of the dryer quickly and then goes to the outlet. The highest velocity value was shown by the A3L1 treatment with the turbulence of 0.024 m/s and the treatment with the lowest value was A2L2L3 with the turbulence of 0.014 m/s. The stability of the

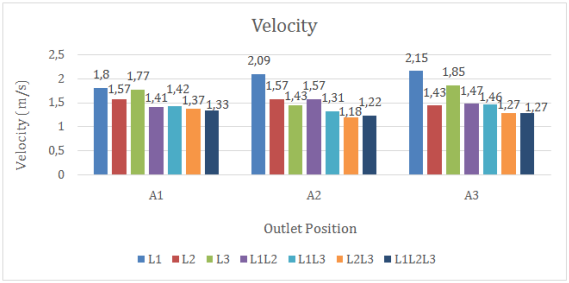

Figure 6. Velocity 21 treatments

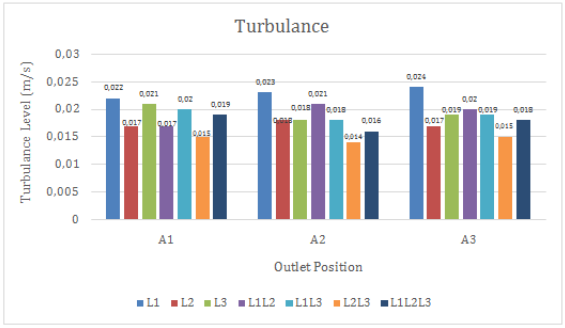

Figure 7. Air turbulance 21 treatments

turbulence level will affect the mass transfer and heat transfer in the dried material [12].

3.2. Hot air distribution process

Airflow scheme blown as shown in Fig. 8 by a fan throughout the drying chamber passes through the bottom of the machine, continues to the drying tray through the gaps and gap of the perforated plate, followed by a distribution to the top of the machine where there is a rotating drying. The rotating rotary is made so that the hot air evenly touches the dried product and the cold air will come out through the air funnel on the right side of the machine.

3.2.1. All Parts

All parts of the machine in 21 treatments, which was taken the treatment that had the highest temperature distribution value, namely the A2L1L2 treatment (Fig. 9). The most uniformity of the red color is the best result because the red color represents the maximum temperature obtained in the design. The average velocity produced in the A2L1L2 treatment was 1.57 m/s, the resulting average was smaller than the one-hole treatment and larger than the three-gaps treatment.

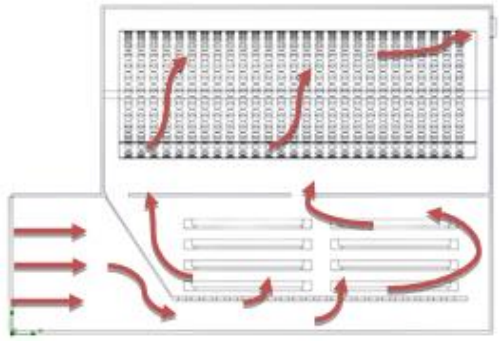

Figure 8. Distribution flow

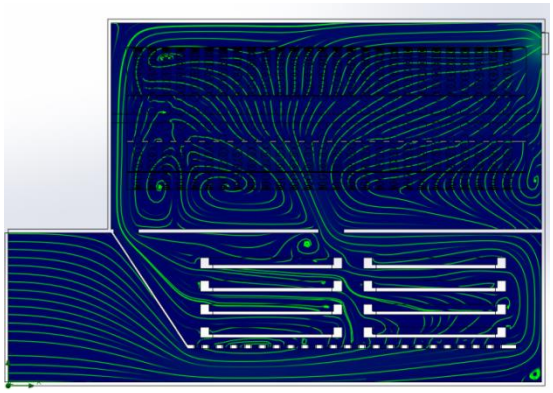

Figure 9. Velocity A2L1L2

These results are because the fewer the number of gaps made the faster the airflow rate and the more gaps the lower the airflow rate. Study in [13] simulated the drying chamber and produced an average speed of 1.51 m/s this was due to a large amount of space so there was not much turbulence. The level of turbulence that occurs is 0.021 m/s, the more gap made the more turbulence that occurs because hot air will touch the end of the hole (Fig. 7). The occurrence of differences in the decrease in water content in different samples is due to differences in turbulence which directly affect the moisture of the dried material [13].

3.2.2. Tray

The simulation results of the A2L1L2 treatment on the tray produce uniform results where the average temperature of the shelf section is 57.52 ^{o}C. This is because the tray is the section that is first fed by hot air (Fig. 10).

The tray dryer that is running usually only the part that is close to the hot air and the hot air is not evenly distributed throughout the shelf [14]. The simulation results show that the average temperature value is not much different from the input temperature and the temperature of each shelf (Fig. 11). The temperature distribution of the dryer in the tray has a standard deviation of 2 ^{o}C, with a maximum and minimum air difference of 5.12 ^{o}C.

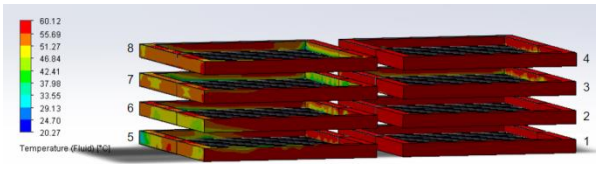

Figure 10. Tray contour A2L1L2

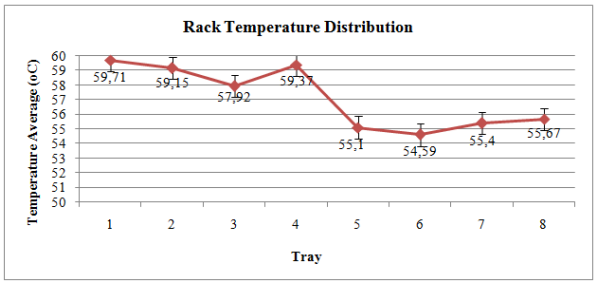

Figure 11. Tray temperature distribution A2L1L2

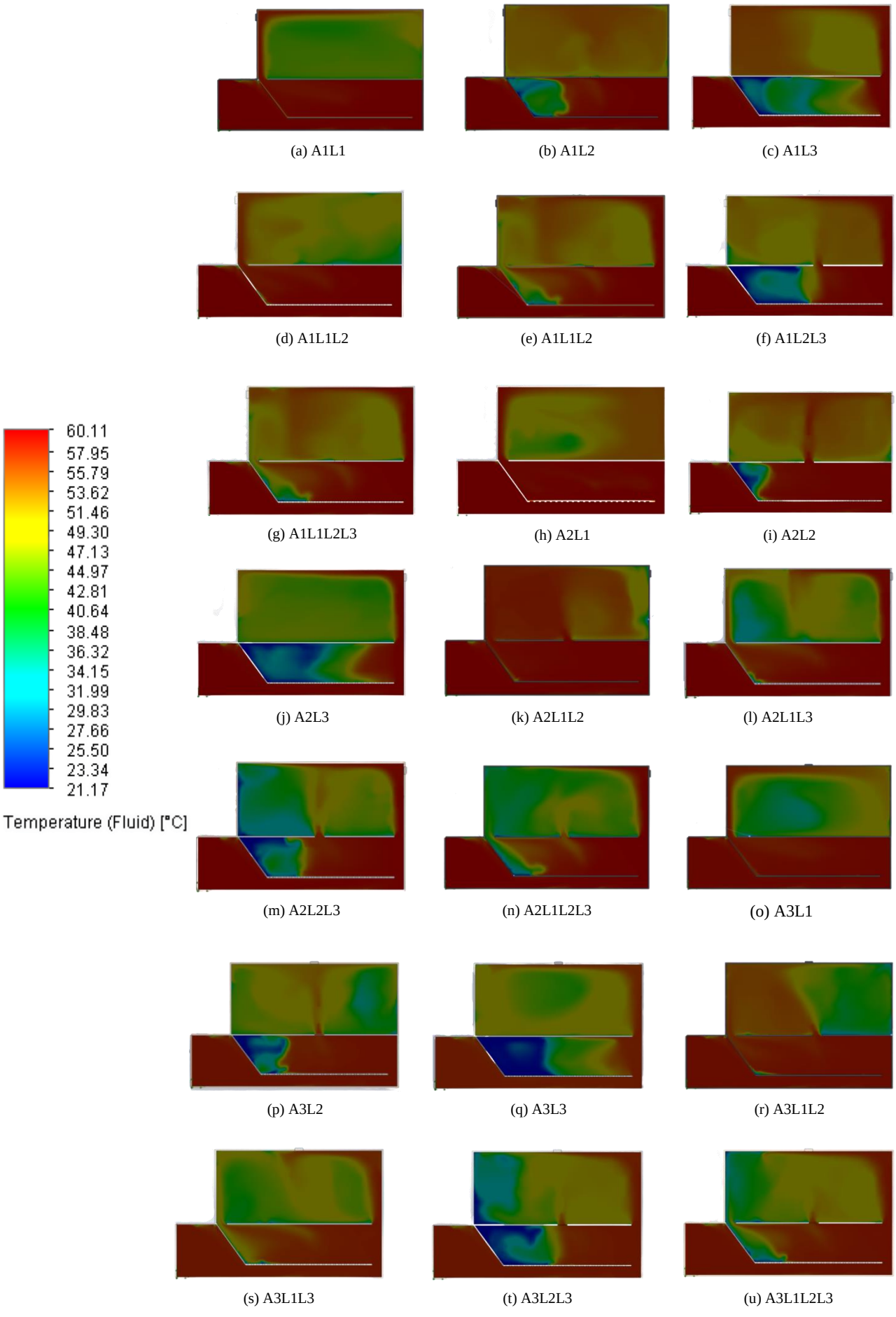

(a) A1L1 (b) A1L2 (c) A1L3

(d) A1L1L2 (e) A1L1L2 (f) A1L2L3

(g) A1L1L2L3 (h) A2L1 (i) A2L2

(j) A2L3 (k) A2L1L2 (l) A2L1L3

(m) A2L2L3 (n) A2L1L2L3 (o) A3L1

(p) A3L2 (q) A3L3 (r) A3L1L2

(s) A3L1L3 (t) A3L2L3 (u) A3L1L2L3

Figure 12. Simulation results

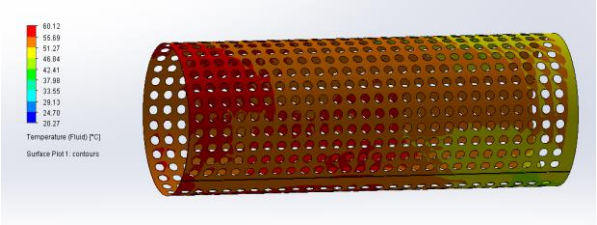

Figure 13. Hot air contours A2L1L2

The highest temperature is still owned by the first tray exposed to airflow, but there is a difference in the 3rd tray. This can be seen in Fig. 13 that the temperature distribution based on color shows more yellow color than tray 1,2, and 4, and tray 3 is in the temperature range 46-51 ^{o}C.

3.2.3. Rotary section

The simulation results of A2L1L2 treatment on the rotary section produce fewer uniform results (Fig. 10) where the average temperature of the rotating part is 53.52 ^{o}C. This is because the rotating part is the part that is flowed with hot air after the tray, the air drops due to convection and conduction heat transfer in the tray. The air temperature in the left rotary is lower than the left, based on the temperature distribution on the left side of 46-51 ^{o}C and on the right a range of 51-60 ^{o}C.

4. Conclusion

The distribution of hot air in the design of this double-type dryer have an average temperature 56.59 ^{o}C, standard deviation 3.55 ^{o}C, velocity 1.57 m/s, pressure 1.06 bar, and turbulence of 0.021 m/s. The average temperature on the tray is 57.52 ^{o}C which is higher than the average rotary temperature of 53.52 ^{o}C. The treatment that gives the most optimal hot air distribution value is the A2L1L2 treatment with the outlet on the right and with 2 gaps opened, gap 1 and gap 2.

References

[1] M. V. Zambrano, B. Dutta, D. G. Mercer, H. L. MacLean, and M. F. Touchie, “Assessment of Moisture Content Measurement Methods of Dried Food Products in Small-Scale Operations in Developing Countries: A Review,” *Trends Food Sci. Technol.*, vol. 88, pp. 484–496, 2019.

[2] C. A. Nababan, A. H. Nasution, and H. Ambarita, “Analisis Computational Fluid Dynamics (CFD) pada Mesin Pengering Pakaian yang Memanfaatkan Energi Panas Buangan Kondensor AC (Air Conditioner) Split 1 PK dengan Menggunakan Software Solidworks 2015,” Universitas Sumatera Utara, 2018.

[3] N. Malekjani and S. M. Jafari, “Simulation of Food Drying Processes by Computational Fluid Dynamics (CFD); Recent Advances and Approaches,” *Trends Food Sci. Technol.*, vol. 78, pp. 206–223, 2018.

[4] J. Castaño-Rodríguez, D. Amaya, and O. Ramos, “Food Dryer Design and Analysis of Velocity and Temperature Profiles,” *Int. J. Appl. Eng. Res.*, vol. 13, pp. 13578–13583, 2018.

[5] S. Misha, S. Mat, M. A. M. Rosli, M. Hafidz Ruflan, K. Sopian, and E. Salleh, “Simulation of Air Flow Distribution in a Tray Dryer by CFD,” *Recent Adv. Renew. Energy Sources*, pp. 126–135, 2015.

[6] P. Demissie, M. Hayelom, A. Kassaye, A. Hailesilassie, M. Gebrehiwot, and M. Vanierschot, “Design, Development and CFD Modeling of Indirect Solar Food Dryer,” *Energy Procedia*, vol. 158, pp. 1128–1134, 2019.

[7] J. Ettannil, V. Rangaraju, and T. J. Zachariah, “Quality of Dry Ginger (Zingiber Officinale) by Different Drying Methods,” *J. Food Sci. Technol.*, vol. 51, 2012.

[8] P. Kaushal and H. K. Sharma, “Convective Dehydration Kinetics of Noodles Prepared from Taro (Colocasia Esculenta), Rice (Oryza Sativa) and Pigeonpea (Cajanus Cajan) Flours,” *Agric. Eng. J. CIGR J.*, vol. 15, no. 4, pp. 202–212, 2013.

[9] A. Rindang, S. Panggabean, and F. Wulandari, “CFD Analysis of Temperature Drying Chamber at Rotary Dryer With Combined Energy,” in *IOP Conference Proceedings Series: Journal of Physics: Conference Series*, 2019.

[10] K. Samborska, D. Witrowa-Rajchert, and A. Gonçalves, “Spray-Drying of α-Amylase-The Effect of Process Variables on the Enzyme Inactivation,” *Dry. Technol.*, vol. 23, no. 4, pp. 941–953, 2005.

[11] A. K. Babu, K. Govindaraj, V. A. A. Raj, and R. Velraj, “CFD Studies on Different Configurations of Drying Chamber for Thin-Layer Drying of Leaves,” *Energy Sources, Part A Recover. Util. Environ. Eff.*, vol. 42, no. 3, pp. 1–13, 2019.

[12] H. Jubaer, S. Afshar, J. Xiao, X. D. Chen, C. Selomulya, and M. W. Woo, “On the Effect of Turbulence Models on CFD Simulations of a Counter-Current Spray Drying Process,” *Chem. Eng. Res. Des.*, vol. 141, pp. 592–607, 2019.

[13] J. Pimsamarn, P. Kitsubun, and R. Tongruk, “Numerical Simulation of Air Flow and Temperature Distribution in Yarn Drying Room,” *ASEAN J. Chem. Eng.*, vol. 11, no. 2, pp. 8–21, 2011.

[14] S. Misha, S. Mat, M. H. Ruslan, K. Sopian, and E. Salleh, “The Prediction of Drying Uniformity in Tray Dryer System using CFD Simulation,” *Int. J. Mach. Learn.*, vol. 3, no. 5, pp. 419–423, 2013.

EPI International Journal of Engineering
Volume 8, Number 1, February 2025, pp. 15-25
DOI: 10.25042/epi-ije.022025.03

*p*ISSN 2615-5109
*e*ISSN 2621-0541

Evaluation of Articulated CAT 745 Fuel Ratio Based on Haul Road Geometry at PT Hillconjaya Sakti Site PT Adhi Kartiko Pratama Tbk

Wahyuni S[a], Rini Novrianti Sutardjo Tui[b], Aryanti Virtanti Anas[c,*], Rizki Amalia[d]

[a]Mining Engineering Undergraduate Study Program, Faculty of Engineering, Hasanuddin University. Email: sw20d@student.unhas.ac.id
[b]Department of Mining Engineering, Faculty of Engineering, Hasanuddin University. Email: rini@unhas.ac.id
[c]Department of Mining Engineering, Engineering Faculty, Hasanuddin University. Email: aryantiv@unhas.ac.id
[d]Department of Mining Engineering, Engineering Faculty, Hasanuddin University. Email: rizkiamalia@unhas.ac.id

Abstract

The distance for transporting overburden at PT Hillconjaya Sakti reaches hundreds of meters. Based on actual conditions, Articulated CAT 745 queues often occur on specific haul road segments due to unsuitable haul road conditions. Hence, the fuel ratio value is in the low-performance category. This study aims to evaluate the fuel ratio value and provide recommendations for improving the geometry of haul roads to meet the established fuel ratio value standards. Multiple linear regression analysis using Eviews 12 VS software was used to determine the variables that significantly affect the fuel consumption of haulers based on haul road geometry. Road grade, total resistance, travel time, and speed of the hauler are independent variables, while fuel consumption is the dependent variable. Based on the data processing results, a fuel ratio value of 1.85 was obtained, and the parameters that significantly affected fuel consumption were total resistance and travel time. Improve haul road conditions based on ESDM Decree No. 1827 K/30/MEM/2018 and AASHTO Manual Rural High Way Design. The fuel ratio value after repairs decreased to 0.60 and was in the best performance category based on PT Hillconjaya Sakti's standard fuel ratio value.

Keywords: Fuel ratio; haul road geometry; load factor; multiple regression

1. Introduction

PT Hillconjaya Sakti uses an open mining system (surface mining) with a backfilling method, where the mine-out area will be used as a disposal area and will move in line with the direction of mining so that the distance to transport layers of soil reaches hundreds of meters. The geometry of the haul road is the main factor related to the activity of the haulage [1]. Road geometry that does not comply with standards and poor road surface conditions can increase the cycle time of the hauler, thereby reducing productivity and increasing fuel consumption. A good haul road design will significantly reduce equipment delivery time, use of fuel, tire costs, and freight costs per ton and establish a safe transportation system [2].

Based on actual conditions in the field, during the process of transporting overburden, there are often queues of Articulated CAT 745 on certain haul road segments, which cause delays and impact work efficiency. Delays that occur result in low productivity and increased fuel usage because the engine continues to work during delays, causing the fuel ratio value to exceed the standards set by the company. The optimal fuel ratio can be achieved if the Articulated CAT 745 is capable of maximum production with efficient fuel consumption. Several factors influence fuel consumption, namely road grade, total resistance, travel time, distance and speed. Road geometry that does not meet established standards, such as road slope and road width, will result in the transport equipment not being able to work optimally and will affect the cycle time of the hauler. The longer the cycle time of the hauler, the higher the fuel consumption rate. Similarly, a high total resistance coefficient will produce a high rolling resistance value so that the engine releases more energy and more force is required to pull the hauler. Therefore, a high rolling resistance value impacts excessive fuel use in the transport equipment. Multiple linear regression analysis is one way to predict factors that significantly influence Articulated CAT 745 fuel consumption. Evaluation of haul road geometry is carried out to determine the suitability of good haul road rules based on road standards and to become a benchmark in road improvements to reduce fuel consumption and meet the standard Articulated CAT 745 fuel ratio value at PT Hillconjaya Sakti as a contractor of PT Adhi Kartiko Pratama Tbk.

2. Methodology

The research was at the Makale Pit PT Hilconjaya Sakti project site PT Adhi Kartiko Pratama Tbk Lameruru

*Corresponding author. Tel.: +62-813-5487-2847
Jalan Perintis Kemerdekaan km. 10 Tamalanrea
Makassar, Indonesia, 90245

Village, Lamanggiri District, North Konawe Regency, Southeast Sulawesi Province, Indonesia. The research stage begins by conducting a literature review from various references. The next stage is conducting field orientation and data collection. The data collected in this research are the topography of the mining area, nickel haul road coordinate data, haul road width, road subsidence depth, haul road conditions, haul cycle time, working hour data, and Articulated CAT 745 hauler specifications. The data that has been obtained is then processed through mathematical equations based on literature. Multiple linear regression analysis is carried out using the E-Views 12 VS software to analyze the influencing factors of CAT 745 fuel consumption, such as road grade, travel time, and total resistance, through multiple linear regression tests and carry out a comparative analysis between actual road geometry and theoretical road geometry standards.

Evaluation is carried out on the width and grade of the road by comparing the actual measurement data with the standard AASHTO road geometry measurements based on the Articulated CAT 745 specifications used by PT Hillconjaya Sakti so that it can be identified which haul road segments do not meet the standards. The evaluation and regression analysis results are used as a reference when making plans to improve road geometry. Road geometry improvements are based on parameters that have a significant effect on fuel consumption and productivity in an effort to achieve standard fuel ratio values.

3. Results and Discussion

3.1. Geometry of mine haul road

The mine haul road should be considered an important asset to a mining operation [2]. Haul road geometry is a calculation of the haulage road space used in transport activities. The road's geometry must match the hauler's dimensions so that the hauler can move freely at normal and safe speeds [3]. Haul roads are an important component of open-pit mining infrastructure because road performance directly impacts operational efficiency and work safety. Haul road geometry consists of many elements, including road width, maximum grade, road cross-grade, etc. The road's geometry must match the equipment's dimensions so that the transportation equipment can move freely at normal and safe speeds [4].

Overburden transportation activities are carried out via two routes. The first route is a hauler route for transporting overburden to disposal with a distance of 976.05 meters. The second route is the route for the hauler back to the mining front with a distance of 982.03 meters. The haul road on each route is divided into 11 segments to make it easier to interpret the condition and geometry of the haul road.

1. Width of haul road

   Determining the minimum haul road width for straight roads (Fig. 1) is based on the rule of thumb according to AASTHO (American Association of State Transportation Highway Officials) AND Minister of Energy and Mineral Resources Decree No 1827 K/30/MEM/2018 with Equation 1 [5].

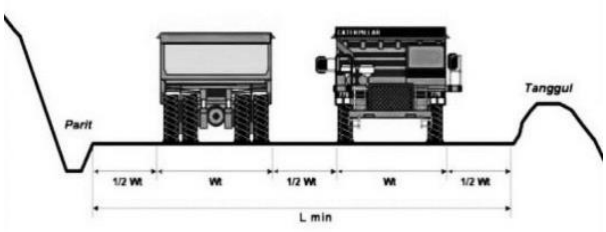

Figure 1. Straight haul road width

$$L = (n \times Wt) + (n + 1)(0.5 \times Wt) \quad (1)$$

where:

L = minimum width of straight haul roads (m)
n = number of lanes
Wt = total hauler width (m)

Calculation of the width of the haul road at curves or bends (Fig. 2) can be done using Equations 2 and 3 [5].

$$W = 2\,(U + Fa + Fb + Z) + C \quad (2)$$

$$C = Z = \frac{1}{2}\,(U + Fa + Fb) \quad (3)$$

where:

W = minimum haul road width at curves (m)
U = distance of vehicle wheel tracks (m)
Fa = front hanging width (m)
Fb = back drop width (m)
C = distance between two trucks that will intersect (m)
Z = distance from the outside of the truck to the edge of the road (m)

Articulated CAT 745 hauler equipment specification data required to determine the minimum carriageway width is presented in Table 1.

Based on Articulated CAT 745 specification data, the straight road width and minimum corner width are as follows.

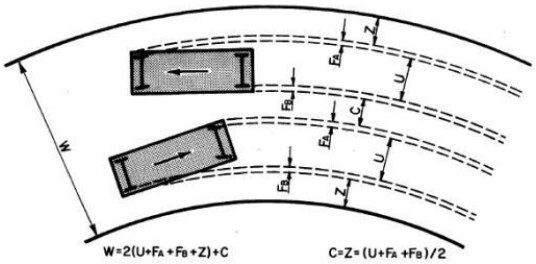

Figure 2. Width of haul road at bends

Table 1. Articulated CAT 745 specification data

Specification	Size
Width of hauler	3.801 m
Length of hauler	11.55 m
Distance between wheels	2.687 m
Front dangle	3.418 m
Back dangle	1.448 m
Wheel storage corner	45°
Fuel tank	550 L

a. Straight road width

$$L_{min}\ (1\ lane) = (1\times3.801) + (1+1) \times (\tfrac{1}{2}\times3.801) \quad (4)$$
$$= 7.60\ m$$
$$L_{min}\ (2\ lane) = (2\times3.801) + (2+1) \times (\tfrac{1}{2}\times3.801) \quad (5)$$
$$= 13.30\ m$$

b. Width of bend road

$$C = Z = 0.5(2{,}687+(3.418\times\sin 45) + (1.448\times \sin 45) \quad (6)$$
$$= 3.06\ m$$
$$L_{min}\ (1\ lane) = 1(2.687 + (3.48 \times \sin 45) + \big((1.448 \times \sin 45)\big) + 3.06 \quad (7)$$
$$= 12.26\ m$$
$$L_{min}\ (2\ lane) = 2(2.687 + (3.48 \times \sin 45) + \big((1.448 \times \sin 45)\big) + 3.06 \quad (8)$$
$$= 21.45\ m$$

The activity of transporting overburden is carried out via two routes, namely the route for transporting overburden to disposal and the route for hauler back to the front of the mine. The actual condition of the haul road route is 1 and 2 lanes, this is because the road construction is adjusted to the topography and geology. The actual road width measurement results for each segment of the loaded and unloaded routes can be seen in Table 2 and Table 3.

Based on Tables 2 and 3, road segments that meet the standards of Ministerial Decree No. 1827/K/30/MEN/2018 only segments E-F and J-K on loaded routes and segments K-J, G-F' and F'-E on unloaded routes

Table 2. Actual width of haul roads on loaded routes

Road Segment	Distance (m)	Number of Lanes	The width of the road (m)		Information
			Straight	Bend	
A-B	61.58	2	10.04	14.18	Not ideal
B-C	73.38	2	10.42	14.18	Not ideal
C-D	56.87	2	10.71	9.38	Not ideal
D-E	51.36	2	12.07	10.19	Not ideal
E-F	199.87	1	12.54	15.22	Ideal
F-G	78.08	1	6.62	11.84	Not ideal
G-H	99.24	2	9.40	16.13	Not ideal
H-I	174.89	2	7.87	-	Not ideal
I-J	97.06	2	11.01	15.50	Not ideal
J-K	68.75	2	16.92	-	Ideal
K-L	14.97	2	8.90	-	Not ideal
Amount	976.05				

Table 2. Width of haul roads unloaded routes

Road Segment	Distance (m)	Number of Lanes	The width of the road (m)		Information
			Straight	Bend	
L-K	14.97	2	8.90	-	Not ideal
K-J	68.75	2	16.92	-	Ideal
J-I	97.06	2	11.01	15.50	Not ideal
I-H	174.89	2	7,87	-	Not ideal
H-G	99.24	2	9.40	16.13	Not ideal
G-F'	139.88	1	9.80	12.50	Ideal
F'-E	144.06	1	6.95	12.87	Ideal
E-D	51.36	2	12.07	10.19	Not ideal
D-C	56.87	2	10.71	9.38	Not ideal
C-B	73.38	2	10.42	14.18	Not ideal
B-A	61.58	2	10.04	14.18	Not ideal
Amount	982.03				

2. Grade of haul road

The grade of the haul road is an important factor that must be observed in detail regarding the condition of the mine road. This is because the grade of the haul road is directly related to the ability of the haulage equipment (grade), both in braking and in overcoming hills. The grade of the haul road can be calculated using Equation 9 [6].

$$i = \frac{\Delta H}{\Delta x}\ x\ 100\% \quad (9)$$

where:

i = grade
ΔH = height difference between 2 measured points (m)
Δx = flat distance between two measured points (m)

Evaluation of the road grade based on the standards of Ministerial Decree No. 1827/K/30/MEN/2018 with a maximum value of mine road grade of 12%. The higher the grade of the road, the greater the fuel consumption [6]. A positive grade indicates the direction of movement of the hauler is upward (uphill), while a negative grade indicates the direction of movement of the hauler is downward (downhill). The road grade on each segment for the load route and the unloaded route is presented in Table 4 and Table 5, respectively.

Based on the data in Table 4 and Table 5, there is a road grade that exceeds the standards of Ministerial Decree No. 1827/K/30/MEN/2018. Road grades exceeding 12% are found on road segments during load and unloaded routes. On the loaded route,

Table 3. Road grade on loaded routes

Road Segment	Distance (m)	Height Difference (m)	Grade (%)
A-B	61.58	-0.21	-0.37
B-C	73.38	1.68	2.93
C-D	56.87	7.62	13.38
D-E	51.36	3.74	6.54
E-F	199.87	4.23	7.39
F-G	78.08	2.93	5.12
G-H	99.24	5.26	9.20
H-I	174.89	3.84	6.71
I-J	97.06	8.29	14.57
J-K	68.75	5.70	9.98
K-L	14.97	5.81	10.17
Amount	976.05		

Table 4. Road grade on the unloaded routes

Road Segment	Distance (m)	Height Difference (m)	Grade (%)
L-K	14.97	-5.81	-10.17
K-J	68.75	-5.70	-9.98
J-I	97.06	-8.29	-14.57
I-H	174.89	-3.84	-6.71
H-G	99.24	-5.26	-9.20
G-F'	139.88	-5.79	-10.144
F'-E	144.06	-1.99	-3.48
E-D	51.36	-3.74	-6.54
D-C	56.87	-7.62	-13.38
C-B	73.38	-1.68	-2.93
B-A	61.58	0.21	0.37
Amount	982.03		

segments C-D and I-J for uphill conditions have grades of 13.38% and 14.57%, and on unloaded routes, segments, J-I and D-C for downhill conditions have grades of -14.57% and -13.38%.

3. Rolling resistance

The surface conditions of the haul roads at PT Hillconjaya Sakti have two soil characteristics, namely smooth, hard, dry dirt, gravel, and well-maintained and soft unplowed dirt, poorly maintained so that tire subsidence easily forms in large sizes. The characteristics of smooth, hard, dry dirt, gravel, and well-maintained have a rolling resistance coefficient of 2%, and the characteristics of soft, unblown dirt, poorly maintained, have a rolling resistance coefficient of 4%.

Rolling resistance is obtained based on subsidence data on each road segment through direct measurements in the field and the load of the Articulated CAT 745 hauler. Based on Table 6 and Table 7, the results of the rolling resistance calculation on the overburden load route obtained the largest resistance value on the D-E segment of 19,546.89 lbs, and on the unloaded route, the largest rolling resistance value was obtained on the same road segment, namely the E-D segment, of 10,155.16 lbs.

4. Grade resistance

Road grade s that do not meet standards result in large grade resistance values. This causes the engine to work harder to withstand the grade resistance so that greater engine power is required at the rim at lower speeds, which results in longer cycle times and increased fuel usage. The results of grade resistance calculations are presented in Table 8.

Table 6. Rolling resistance on the loaded route

Road Segment	Vehicle Weight (Tons)	Rolling Resistance Coefficient (%)	Subsidence Data (Inches)	Rolling Resistance (lbs)
A-B		4	5.05	16,745.53
B-C		4	3.42	13,201.13
C-D		4	3.00	12,291.54
D-E		2	7.68	19,546.89
E-F		2	2.52	8,358.53
F-G	65.6	4	1.25	8,489.49
G-H		2	1.44	6,024.06
H-I		2	1.25	5,597.03
I-J		2	1.97	7,162.83
J-K		2	1.02	5,113.05
K-L		4	0.79	7,493.07

Table 7. Rolling resistance on unloaded routes

Road Segment	Vehicle Weight (Tons)	Rolling Resistance Coefficient (%)	Subsidence Data (Inches)	Rolling Resistance (lbs)
L-K		4	0.79	1,041.59
K-J		2	1.02	1,354.04
J-I		2	2.00	2,645.56
I-H		2	1.44	1,909.53
H-G		2	1.44	1,909.53
G-F	40	2	1.00	1,319.32
F-E		2	1.00	1,328.00
E-D		2	7.68	10,155.16
D-C		4	3.00	3,967.49
C-B		4	3.42	4,522.11
B-A		4	5.05	6,683.34

Table 5. Results of grade resistance calculations

Load Route			Unloaded Route		
Road Segment	*Grade* (%)	Grade Resistance (lbs)	Road Segment	*Grade* (%)	Grade Resistance (lbs)
A-B	-0.37	-489.38	L-K	-10.17	-8,137.60
B-C	2.93	3,837.60	K-J	-9.98	-7,982.40
C-D	13.38	17,557.18	J-I	-14.57	-11,658.40
D-E	6.54	8,576.54	I-H	-6.71	-5,366.40
E-F	7.39	9,700.93	H-G	-9.20	-7,363.20
F-G	5.12	6,712.19	G-F	-10.14	-8,115.20
G-H	9.20	12,075.65	F-E	-3.48	-2,783.20
H-I	6.71	8,800.90	E-D	-6.54	-5,229.60
I-J	14.57	19,119.78	D-C	-13.38	-10,705.60
J-K	9.98	13,091.14	C-B	-2.93	-2,340.00
K-L	10.17	13,345.66	B-A	0.37	298.40

The results of calculating grade resistance on the loaded route obtained the largest resistance value on the I-J segment of 19,199.78 lbs, while on the unloaded route, the largest grade resistance value was obtained on the same road segment, namely the J-I segment, of -11,658.40 lbs.

5. Total resistance

Total resistance is the drag force between the wheels and the haul road conditions. The total resistance is obtained based on the rolling and tilt resistance values. Different road surface characteristics and road grades will influence the equipment's productivity level and fuel consumption of transportation equipment [7]. The results of calculating the total resistance value on the load and unloaded routes can be seen in Table 9 and Table 10, respectively.

The total resistance on the unloaded route shows that the largest resistance value on the C-D road segment is 29,848.72 lbs. Based on Table 10, the largest total resistance value on the B-A road segment is 6,981.74 lbs.

Table 6. Total resistance on the loaded route

Road Segment	Rolling Resistance (lbs)	Grade Resistance (lbs)	Total Resistance (lbs)
A-B	16.745,53	-489,38	16.256,15
B-C	12.204,71	3.837,60	16.042,31
C-D	12.291,54	17.557,18	29.848,72
D-E	9.582,70	8.576,54	18.159,25
E-F	8.358,53	9.700,93	18.059,46
F-G	8.489,49	6.712,19	15.201,68
G-H	6.024,06	12.075,65	18.099,71
H-I	5.597,03	8.800,90	14.397,92
I-J	7.162,83	19.119,78	26.282,60
J-K	5.113,05	13.091,14	18.204,19
K-L	7.493,07	13.345,66	20.838,73

Table 7. Total resistance on unloaded routes

Road Segment	Rolling Resistance (lbs)	Grade Resistance (lbs)	Total Resistance (lbs)
L-K	1.041,59	-8.137,60	-7.096,01
K-J	1.354,04	-7.982,40	-6.628,36
J-I	2.645,56	-11.658,40	-9.012,84
I-H	1.909,53	-5.366,40	-3.456,87
H-G	1.909,53	-7.363,20	-5.453,67
G-F'	1.319,32	-8.115,20	-6.795,88
F'-E	1.328,00	-2.783,20	-1.455,20
E-D	4.079,43	-5.229,60	-1.150,17
D-C	3.967,49	-10.705,60	-6.738,11
C-B	3.914,54	-2.340,00	1.574,54
B-A	6.683,34	298,40	6.981,74

Table 8. Rimpull of the Articulated CAT 745

Gear	*Horse Power* (HP)	Speed (mph)	*Rimpull* (lbs)
1st	504	3.8	42,276.32
2nd		5.0	32,130.00
3rd		7.0	22,950.00
4th		8.8	18,255.68
5th		11.6	13,849.14
6th		14.2	11,313.38

3.2. Rimpull

Rimpull is the amount of pulling force a machine tool can exert on the surface of a roadway [8]. House power and speed of each gear are obtained based on Articulated CAT 745 hauler specification data, while mechanical efficiency is assumed to be 85% (1-year unit). Rimpull is expressed in pounds (lbs) and is usually listed in the engine specifications. Rimpull for acceleration is the increase in speed of a moving hauler obtained from the acceleration force taken from the excess rimpull. The results of the rimpull calculation for each gear based on house power and hauler speed based on the Articulated CAT 745 specifications are presented in Table 11.

The maximum speed obtained in gear 1 is 42,276.32 lbs at a speed of 3.8 mph. The rimpull produced by the engine must be greater than the total resistance so that the hauler can accelerate. If the total resistance can be reduced, the operator can increase the speed to a higher gear by company operational standards at a safe speed. Optimal speed can speed up the cycle time so that there is a change from the actual cycle time condition to the cycle time based on rimpull.

3.3. Load factor

The load factor is a multiplying factor to obtain actual horsepower. Maximum power is not used continuously during the working period, so the load factor depends on the working conditions. The load factor can be calculated based on rimpull usage. Load factor can use Equation 10:

$$Load\ Factor = \frac{Rimpull\ used}{Maximum\ rimpull} \quad (10)$$

3.4. Productivity of Hauler

Productivity is calculated based on cycle time data, work efficiency, swell factor, and fill factor calculated using Equation 12.

$$C = KB \times FF \times n \quad (11)$$

$$Q = \frac{C \times 60 \times Ek \times SF}{Cta} \quad (12)$$

where:

Q = production per hour hauler (m^3/hour)
n = number of excavator buckets to fill the hauler
KB = bucket capacity (m^3)
FF = *fill factor* (%)
SF = *swell factor*
Ek = hauler working time (%)
Cta = hauler cycle time (minutes)

The productivity of one Articulated CAT 745 unit is as follows:

$$Q = \frac{16\ LCM \times 45\% \times 60\ minute/hour}{18.60\ minute} \quad (13)$$
$$= 23.22\ LCM/hour$$

So the productivity of Articulated CAT 745 obtained is 23.22 LCM/hour.

3.5. Fuel consumption

Fuel consumption is the main parameter that is always considered when selecting a tool because it is the most significant contributor to operational costs [9]. The power required by a vehicle to drive the engine affects fuel consumption. Calculating the fuel requirements for a tool is very important to evaluate it in terms of fuel usage because fuel contributors have a significant influence on a company's finances. The size of a hauler's fuel consumption depends not only on the engine characteristics but is also influenced by the hauler's driving force, transport road conditions, speed, and power. The main variables in the vehicle's driving force are rolling resistance and grade resistance. The conditions of the haul road are the condition of the road surface and the grade of the road [10].

1. Fuel consumption (liters/hour)
   PT Hillconjaya Sakti uses 70% palm biodiesel (B30) fuel from PT Sinar Alam Duta Perdana II. Energy sources for haulers are transitioning to reduce emissions from fossil fuels and the resulting climate change [11]. Biodiesel is a form of new, renewable energy that reduces the use of fossil fuels. Palm biodiesel has a specific fuel consumption of 0.48 kg/kWh and a density of 7.06 lb/gallon [12]. Fuel consumption is the specific ratio of fuel entering the engine for one hour multiplied by the load factor and divided by the fuel density per liter. It is calculated using Equation 14 [10].

   $$FC = \frac{SFC \times P \times LF}{FD} \quad (14)$$

   where:
   FC = fuel consumption (liters/hour)
   SFC = specific fuel consumption (kg/kwH)
   LF = load factor
   FD = fuel density (kg/m^3)

   The results of calculating fuel consumption per hour have been summarized in Table 12. Based on the results of fuel consumption calculations in Table 12, the theoretically estimated fuel consumption of the Articulated CAT 745 on the loaded route is 62.98 liters/hour, while on the unloaded route, it is 41.66 liters/hour. The results of this calculation are then used to estimate actual fuel consumption based on the travel time of the hauler.

2. Fuel Consumption (liters/rit)
   Articulated CAT 745 fuel consumption calculations are carried out to estimate the amount of fuel used per drive for each segment. The results of actual fuel consumption calculations can be seen in Table 13.

Table 9. Results of theoretical fuel consumption calculations

Loaded Route		Unloaded Route	
Road Segment	Fuel Consumption (liters/hour)	Road Segment	Fuel Consumption (liters/hour)
A-B	56.37	L-K	42.77
B-C	57.73	K-J	43.94
C-D	75.10	J-I	46.99
D-E	87.18	I-H	42.83
E-F	52.86	H-G	41.36
F-G	56.57	G-F'	42.85
G-H	56.09	F'-E	41.36
H-I	55.16	E-D	28.78
I-J	78.08	D-C	44.19
J-K	56.32	C-B	40.69
K-L	61.28	B-A	42.52
Average	62.98		41.66

Table 11. Results of actual fuel consumption calculations

Loaded Route			Unloaded Route		
Road Segment	Average Cycle Time (Seconds)	Fuel Consumption (Liters/Rit)	Road Segment	Average Cycle Time (Seconds)	Fuel Consumption (Liters/Rit)
A-B	35.59	0.62	L-K	28.04	0.32
B-C	30.48	0.53	K-J	36.80	0.43
C-D	93.93	1.64	J-I	75.32	0.87
D-E	22.54	0.39	I-H	27.36	0.32
E-F	25.18	0.44	H-G	17.30	0.20
F-G	16.51	0.29	G-F'	14.44	0.17
G-H	25.85	0.45	F'-E	18.49	0.21
H-I	19.99	0.35	E-D	32.79	0.38
I-J	75.54	1.32	D-C	93.15	1.08
J-K	47.03	0.82	C-B	32.25	0.37
K-L	21.82	0.38	B-A	43.24	0.50
Amount		7.25			4.85
		12.10			

The total fuel consumption of the Articulated CAT 745 on all haulage road segments during the load route and unloaded route for one hour is as follows.

$$\text{Fuel consumption} = 12.10 \text{ (liters/rit)} \times 3.23 \text{ (rit/hour)} = 39.03 \text{ liters/hour} \quad (15)$$

The condition of the hauler at idle time is around 10% of the total demand when the hauler is running [13], so the total fuel consumption of the Articulated CAT 745 is as follows.

$$\text{Total fuel consumption} = 39.03 \text{ liters/hour} + 39.03 \times 10\% = 42.93 \text{ liters/hour} \quad (16)$$

So, the total fuel consumption of the Articulated CAT 745 on the load route and unloaded route is 42.93 liters/hour.

3.6. Actual fuel ratio

Fuel ratio is the amount of fuel (liters) released to obtain 1 BCM of overburden [14]. Factors that influence the fuel ratio value are fuel consumption (liters/hour) and equipment productivity (bcm/hour). The total productivity for one unit of Articulated CAT 745 is 23.22 LCM/hour, and the total fuel consumption used is 42.93 liters/hour, so the fuel ratio of the Articulated CAT 745 hauler is as follows.

Table 10. PT Hillconjaya Sakti standard fuel ratio

Performance Level	RF value
Low Performance	> 1.19
Average	1.00 – 1.19
Best Performance	< 1.00

$$\text{Fuel ratio} = \frac{42.93 \text{ liters/hour}}{23.22 \text{ LCM/hour}} = 1.85 \text{ liters/LCM} \quad (17)$$

The fuel ratio obtained is 1.85 liters/LCM, which is included in the low-performance category based on the standard fuel ratio value set by PT Hillconjaya Sakti in Table 14.

PT Hillconjaya Sakti can meet the standard fuel ratio values set by reducing fuel consumption and increasing the productivity of transportation equipment. The solution to reduce fuel consumption and increase productivity is to evaluate the condition of the haul roads used in overburden hauling activities at the Makale Pit.

3.7. Multiple linear regression analysis

Multiple linear regression analysis is a linear relationship between two or more independent variables and the dependent variable. This analysis is to measure the intensity of the relationship between two or more and make an approximate prediction of the value of Y over predict two or more predictor variables against the criterion variable. Equation 18 is a multiple linear regression equation [7].

$$Y = a + b_1X_1 + b_2X_2 + \cdots b_nX_n \quad (18)$$

where,

Y = dependent variable
X = independent variable
a = constant
b = independent variable regression coefficient

Prediction of fuel consumption on mining transportation equipment using the multiple regression method [15]. Classical assumptions are important for applying multiple regression, such as the assumptions of linearity, normality, non-multicollinearity, and homoscedasticity; if none of the assumptions are met, then the resulting output will be bad from the multiple regression variables [16].

Multiple regression variables I and multiple regression II are presented in Table 15, Table 16, Table 17, and Table 18.

The independent variables in multiple linear regression I are road grade (X1) and total resistance (X2) and the independent variables in multiple linear regression II are travel time (X1) and speed (X2). The dependent variable in this analysis is the fuel ratio (Y). Multiple regression analysis I and multiple regression II are differentiated based on the value of the independent variable which is fixed and can change under the same conditions. Road grade and total resistance are variables with fixed values under the same conditions used as independent variables in multiple regression I. Travel time and speed are variables with values that can change under the same conditions used as independent variables in multiple linear regression II.

Table 12. Multiple linear regression variable I on loaded routes

Theoretical Fuel (Y)	Grade (X_1)	Total Resistance (X_2)
56.37	0.37	16256.15
57.73	2.93	17038.73
75.10	13.38	29848.72
87.18	6.54	28123.43
52.86	7.39	18059.46
56.57	5.12	15201.68
56.09	9.20	18099.71
55.16	6.71	14397.92
78.08	14.57	26282.60
56.32	9.98	18204.19
61.28	10.17	20838.73

Table 13. Multiple linear regression variable I on unloaded routes

Theoretical Fuel (Y)	Grade (X_1)	Total Resistance (X_2)
42.77	10.17	7096.01
43.94	9.98	6628.36
46.99	14.57	9012.84
42.83	6.71	3456.87
41.36	9.20	5453.67
42.85	10.14	6795.88
41.36	3.48	1455.20
28.78	6.54	4925.56
44.19	13.38	6738.11
40.69	2.93	2182.11
42.52	0.37	6981.74

Table 14. Multiple linear regression variable II on loaded routes

Actual Fuel (Y)	Traveling time (X_1)	Speed (X_2)
0.62	35.59	1.73
0.53	30.48	2.41
1.64	93.93	0.61
0.39	22.54	2.28
0.44	25.18	7.94
0.29	16.51	4.73
0.45	25.85	3.84
0.35	19.99	8.75
1.32	75.54	1.28
0.82	47.03	1.46
0.38	21.82	0.69

Table 15. Multiple linear regression variable II on unloaded routes

Actual Fuel (Y)	Traveling time (X_1)	Speed (X_2)
0.32	28.04	0.53
0.43	36.80	1.87
0.87	75.32	1.29
0.32	27.36	6.39
0.20	17.30	5.74
0.17	14.44	9.69
0.21	18.49	7.79
0.38	32.79	1.57
1.08	93.15	0.61
0.37	32.25	2.28
0.50	43.24	1.42

1. Classic assumption test
   The classical assumption test must be fulfilled as a condition for multiple linear regression, namely that there is no heteroscedasticity and no multicollinearity, and it is normally distributed [17].
   a. Normality test
      The normality test aims to determine whether or not there is a normal distribution of residual values for the dependent variable and independent variables. Normality test results above α (0.05) support H0, which means the residuals are distributed normally and the assumptions are met.
      1) Multiple linear regression I
         a) Loaded route
            The test result has a sig value of 0.712646, which means the value is greater than 0.05, so it is concluded that the residual is normally distributed or passes the normality test.
         b) Unloaded route
            The test result has a sig value of 0.000009, which means the value is smaller than 0.05, so it can be concluded that the residuals are not normally distributed or do not pass the normality test. Data that is not normally distributed can be overcome using detection and eliminating outliers [16]. The test results have a sig value of 0.954511, which means the value is greater than 0.05, so it is concluded that the residuals are normally distributed or pass the normality test.
      2) Multiple linear regression II
         a) Loaded route
            The sig value test result is 0.796351, which means the value is greater than 0.05, so it is concluded that the residual is normally distributed or passes the normality test.
         b) Unloaded route
            The sig value test result is 0.882869, which means the value is greater than 0.05, so it is concluded that the residual is normally distributed or passes the normality test.
   b. Heteroscedasticity test
      The heteroscedasticity test was carried out to determine any deviations from the classical assumption requirements in the regression model. The regression model must meet the requirements, namely the absence of heteroscedasticity in the data used. One way to detect heteroscedasticity is if the independent variable significantly influences the dependent variable with a significance level below 5%.
      1) Multiple linear regression I
         a) Loaded route
            The sig value test result (Prob. Chi-Square on Obs*R-squared) is 0.0908, which means the value is greater than 0.05 so it is concluded that heteroscedasticity does not occur.
         b) Unloaded route
            The sig value test result (Prob. Chi-Square on Obs*R-squared) is 0.3741, which means the value is greater than 0.05 so it is concluded that heteroscedasticity does not occur.
      2) Multiple linear regression II
         a) Loaded route
            The test results show that the sig value (Prob. Chi-Square on Obs*R-squared) is 0.3773, which means the value is greater than 0.05 so it can be concluded that heteroscedasticity does not occur.
         b) Unloaded route

The test results show that the sig value (Prob. Chi-Square on Obs*R-squared) is 0.7418, which means the value is greater than 0.05 so it can be concluded that heteroscedasticity does not occur.

c. Multicollinearity test
The multicollinearity test occurs if the independent variables are strongly correlated with other independent variables.
1) Multiple linear regression I
a) Loaded route
The test results show that the variance inflation factor (VIF) value of the grade and total resistance is 1.676174, respectively, which means the value is less than 10, so it can be concluded that there is no multicollinearity.
b) Unloaded route
The test results show that the variance inflation factor (VIF) value of the road grade and total resistance is 1.706051 and 1.699240, respectively, which means the value is less than 10, so it is concluded that there is no multicollinearity.
2) Multiple linear regression II
a) Loaded route
The test results show that the variance inflation factor (VIF) value of the travel time and speed is 1.377563, respectively, which means the value is less than 10, so it can be concluded that there is no multicollinearity.
b) Unloaded route
The test results show that the variance inflation factor (VIF) value of the travel time and speed is 1.695555, respectively, which means the value is less than 10, so it is concluded that there is no multicollinearity.

2. Multiple linear regression model
The multiple linear regression equation model was obtained based on the coefficient values resulting from the analysis. The equation model consists of equations on the load and unloaded routes from each multiple regression I and multiple regression II.
a. Multiple linear regression I
1) Loaded route
Based on the results of multiple linear regression the model Equation 20 for the load route is obtained as follows:

$$Y = 21.98070 - 0.633917\ X_1 + 0.002274\ X_2$$

2) Unloaded route
The regression equation model for the unloaded route can be shown as follows:

$$Y = 39.58199 + 0.159428\ X_1 + 0.000372\ X_2$$

b. Multiple linear regression II
1) Loaded route
The results of multiple linear regression obtained the equation as follows.

$$Y = -0.003220 + 0.017495\ X_1 + 0.000400\ X_2$$

2) Unloaded route
Based on the results of multiple linear regression, the equation model for the unloaded route is:

$$Y = -0.003355 + 0.011620\ X_1 + 0.000409\ X_2$$

3. Significance test
The significance test in multiple linear regression consists of a simultaneous test, partial test, and coefficient of determination.
a. Simultaneous test (f-test)
The simultaneous test (F-test) aims to find out whether the independent variables (X_1 and X_2) together (simultaneously) significantly influence the dependent variable (Y).
1) Multiple linear regression I
a) Loaded route
The results of multiple linear regression estimation on loaded routes have test results that show a prob value (F-statistic) of 0.000291, which is smaller than 0.05 so that the independent variables simultaneously have a significant effect on the dependent variable.
b) Unloaded route
The results of multiple linear regression estimation on the unload route have test results that show a prob value (F-statistic) of 0.000041, which is smaller than 0.05 so that the independent variables simultaneously have a significant effect on the dependent variable.
2) Multiple linear regression II
a) Loaded route
The results of the multiple linear regression estimation on the loaded route have test results that show a prob value (F-statistic) value of 0.000000 is smaller than 0.05 so that the independent variable simultaneously has a significant effect on the dependent variable.

b) Unloaded route
The results of multiple linear regression estimates on unloaded routes have test results that show a prob value (F-statistic) value of 0.000000 is smaller than 0.05 so that the independent variables simultaneously have a significant effect on the dependent variable.

b. Partial test (t-test)
The partial test (t-test) aims to determine the effect of each independent variable individually on the dependent variable.
1) Multiple linear regression I
a) Loaded route
Based on the results of multiple linear regression estimates on loaded routes, the following results are obtained.
- Prob value. on the road grade variable (X_1) of 0.1984 is greater than the

significance level of 0.05. This indicates that the road grade variable (X_1) has no significant effect on fuel consumption (Y).

- Prob value. the total resistance variable (X_2) of 0.0002, it is smaller than the significance level of 0.05; this shows that the total resistance variable (X_2) has a significant effect on fuel consumption (Y).

b) Unloaded Route

The results of multiple linear regression estimates on the unloaded route are:

- Prob value. on the road grade variable (X_1) of 0.1835, which is greater than the significance level of 0.05; this shows that the road grade variable (X_1) has no significant effect on fuel consumption (Y).
- Prob value. on the total resistance variable (X_2) of 0.1135, which is greater than the significance level of 0.05; this shows that the total resistance variable (X_2) has no significant effect on fuel consumption (Y).

2) Multiple linear regression II

a) Loaded route

Estimation results of multiple linear regression on loaded routes obtain:

- Prob value. in the travel time variable (X_1) of 0.0000 is smaller than the significance level of 0.05, this indicates that the travel time variable (X_1) has a significant effect on fuel consumption (Y).
- Prob value. on the speed variable (X_2) of 0.0554, which is greater than the significance level of 0.05; this indicates that the speed variable (X_2) has no significant effect on fuel consumption (Y).

b) Unloaded route

The results based on multiple linear regression estimates on the unloaded route are:

- Prob value. in the travel time variable (X_1) of 0.0000 is smaller than the significance level of 0.05, this indicates that the travel time variable (X_1) has a significant effect on fuel consumption (Y).
- Prob value. on the speed variable (X_2) of 0.3377, which is greater than the significance level of 0.05; this shows that the speed variable (X_2) has no significant effect on fuel consumption (Y).

c. Coefficient of determination

The coefficient of determination explains the variation in the influence of the independent variables on the dependent variable or can also be said to be the proportion of the influence of all independent variables on the dependent variable. The value of the coefficient of determination of multiple linear regression can be measured by the Adjusted R-Square value, namely when the number of independent variables is more than one [18].

1) Multiple linear regression I

a) Loaded route

It is found from the loaded route equation that the correlation coefficient (Adjusted R-Square) was 0.836677 or had a contribution effect of 83.6677% on fuel consumption and the other 16.3323% was influenced by other factors but not included in the calculation. So, the grade of the road (X_1) and total resistance (X_2) strongly influence the increase in fuel consumption.

b) Unloaded route

Based on the estimation results in the multiple linear regression model on the unloaded route, the correlation coefficient (Adjusted R-Square) value is 0.937048 or has a contribution effect of 93.7048% on fuel consumption, and other factors influence the other 6.2952% but not included in the calculation. The grade of the road (X_1) and total resistance (X_2) have a very high influence on the increase in fuel consumption.

2) Multiple linear regression II

a) Loaded route

Based on the estimation results in the multiple linear regression model on the loaded route, it is known that the correlation coefficient (Adjusted R-Square) was 0.999990 or had a contribution effect of 99.9990% on fuel consumption, and other factors influenced the other 0.001% but not included in the calculation. Thus, travel time (X_1) and speed (X_2) have a very high influence on the increase in fuel consumption.

b) Unloaded route

The estimation results in the multiple linear regression model on unloaded routes show that the correlation coefficient (Adjusted R-Square) was 0.999879 or had a contribution effect of 99.9904% on fuel consumption and other factors influenced the other 0.0096% but not included in the calculation. Thus, travel time (X_1) and speed (X_2) have a very high influence on the increase in fuel consumption.

The variables that significantly affect fuel consumption are total resistance (on the loaded route) and travel time (on the unloaded route). The effect of total resistance and travel time on fuel consumption has a positive relationship where the lower the value of these parameters, the lower the fuel consumption.

3.8. Road geometry improvement plan

The parameters that have a significant effect on fuel consumption are total resistance and speed. The plan to improve the haul road's geometry regarding the haul road's width and the road's grade, respectively, can be shown in Table 19 and Table 20.

Evaluation of the haul road geometry is carried out on the width of the haul road following the minimum road width based on the Articulated CAT 745 specifications. The width of the road must match the dimensions of the equipment used by PT Hillconjaya Sakti so that the hauler can move freely and safely, increasing the speed of transportation equipment and avoiding delays. In this way, the cycle time of the hauler will decrease, thereby reducing fuel consumption and increasing the productivity of the Articulated CAT 745.

Table 17. Results of the plan to improve the width of the haul road

Freight Road Segment	Width (m)		Freight Road Segment	Width (m)	
	Straight ahead	Bend		Straight ahead	Bend
A-B	13.30	21.45	L-K	13.30	-
B-C	13.30	21.45	K-J	16.92	-
C-D	13.30	21.45	J-I	13.30	21.45
D-E	13.30	21.45	I-H	13.30	-
E-F	7.60	12.26	H-G	13.30	21.45
F-G	7.60	12.26	G-F'	9.80	12.26
G-H	13.30	21.45	F'-E	7.60	21.45
H-I	13.30	-	E-D	13.30	21.45
I-J	13.30	21.45	D-C	13.30	21.45
J-K	16.92	-	C-B	13.30	21.45
K-L	13.30	-	B-A	13.30	21.45

Table 18. Results of the plan to improve the grade of the haul road

Freight Road Segment	Grade (%)	Unloaded Road Segment	Grade (%)
A-B	-0.37	L-K	-10.00
B-C	2.93	K-J	-9.00
C-D	12.00	J-I	-12.00
D-E	6.54	I-H	-6.71
E-F	7.39	H-G	-8.00
F-G	5.12	G-F'	-10.00
G-H	8.00	F'-E	-3.48
H-I	6.71	E-D	-6.54
I-J	1.00	D-C	-12.00
J-K	9.00	C-B	-2.93
K-L	10.00	B-A	0.37

The haul road geometry evaluation plan carried out is that the haul road grade that exceeds the standard is evaluated based on Ministerial Decree No. 1827/K/30/MEN/2018 standards to reduce the grade resistance value. Maintaining the condition of haul road materials, such as adding soil hardening material to prevent tire subsidence, thereby reducing the rolling resistance value. Reducing the rolling resistance and tilt resistance values will directly reduce the total resistance as a parameter, significantly affecting fuel consumption.

3.5 Fuel ratio results recommendations for improvement

The fuel consumption calculation (liters/hour) is based on the load factor obtained from the haul road geometry improvement plan results. The results of the calculation of liter/hour fuel consumption are shown in Table 21.

Calculation of fuel consumption as an example of the A-B segment is:

Table 16. Results of fuel consumption calculations (liters/hour) based on the haul road geometry improvement plan

Loaded Route		Unloaded Route	
Road Segment	Fuel Consumption (liters/hour)	Road Segment	Fuel Consumption (liters/hour)
A-B	57.81	L-K	43.06
B-C	58.81	K-J	42.22
C-D	72.55	J-I	43.05
D-E	72.74	I-H	42.83
E-F	56.35	H-G	45.11
F-G	56.21	G-F'	44.06
G-H	58.03	F'-E	41.36
H-I	55.16	E-D	41.99
I-J	64.87	D-C	41.75
J-K	58.55	C-B	42.16
K-L	61.26	B-A	43.11
Average	61.12		42.79

$$\text{Fuel consumption} = \frac{33.82 \text{ sec/rit}}{3.600 \text{ sec/h}} \text{ x } 61.12 \text{ liters/hour} = 0.57 \text{ liters/rit} \quad (19)$$

The fuel consumption (liters/rit) of each segment can be seen in Table 22.

The total fuel consumption of the Articulated CAT 745 on all haulage road segments during the load route and unloaded route for one hour is as follows:

$$\text{Fuel consumption (liters/hour)} = 10.86 \text{ (liters/rit)} \times 3.48 \text{ (rit/hour)} = 37.76 \text{ liters/hour} \quad (20)$$

The condition of the hauler at the idle time is around 10% of the total demand when the hauler is running [12], so the total fuel consumption of the Articulated CAT 745 is:

$$\text{Total fuel consumption (liters/hour)} = 37.76 + (37.76 \times 10\%) = 41.54 \text{ liters/hour} \quad (21)$$

So, the total fuel consumption of the Articulated CAT 745 on the loaded and unloaded routes is 41.54 liters/hour. The total fuel consumption of the Articulated CAT 745 on the loaded and unloaded routes is 40.28 liters/hour, so the fuel ratio value resulting from recommendations for improving the haul road geometry is as follows.

$$\text{Fuel ratio} = \frac{41.54 \text{ liters/hour}}{25.03 \text{ LCM/hour}} = 0.60 \text{ liters/LCM} \quad (22)$$

Table 19. Results of actual fuel consumption calculations

Loaded Route			Unloaded Route		
Road Segment	Average Cycle Time (Seconds)	Fuel Consumption (Liters/Rit)	Road Segment	Average Cycle Time (Seconds)	Fuel Consumption (Liters/Rit)
A-B	33.82	0.57	L-K	27.74	0.33
B-C	30.06	0.51	K-J	36.80	0.44
C-D	93.93	1.59	J-I	73.61	0.87
D-E	22.54	0.38	I-H	18.40	0.22
E-F	15.03	0.26	H-G	16.56	0.20
F-G	13.15	0.22	G-F'	12.88	0.15
G-H	16.91	0.29	F'-E	14.72	0.17
H-I	18.79	0.32	E-D	22.08	0.26
I-J	75.14	1.28	D-C	92.01	1.09
J-K	37.57	0.64	C-B	29.44	0.35
K-L	18.79	0.32	B-A	33.12	0.39
Amount		6.38			4.49
			10.86		

The fuel ratio is influenced by two factors, namely, the amount of fuel consumed and the productivity of the tool. The lower the fuel consumption and the greater the productivity of the tool achieved, the lower the fuel ratio value will be. The optimum fuel ratio value is the target to achieve large profits. The optimum fuel ratio obtained based on road repair recommendations is 0.60 liters/LCM. These results have met the standard fuel ratio value expected by PT Hillconjaya Sakti (<1.00 liters/LCM) because it is in the best performance category. The decrease from the actual fuel ratio value was 1.25 liters/LCM.

4. Conclusions

The parameters that significantly affect the fuel consumption of Articulated CAT 745 are total resistance and travel time. Total resistance affects fuel consumption with a probability value (p-value) of 0.0002, and travel time affects fuel consumption at a p-value of 0.0000. Both total resistance and travel time significantly affect fuel consumption because their p-values are much smaller than 0.05. Travel time has the strongest effect, as indicated by the small p-value (close to 0). These results suggest that optimizing travel time and managing total resistance can effectively reduce fuel consumption in the Articulated CAT 745. The estimated optimum of fuel ratio obtained based on the haul road geometry improvement plan is 0.60 liters/LCM.

Acknowledgments

The authors would like to thank profusely PT Adhi Kartiko Pratama Tbk. especially Mr. Maridup P. Sirait as Project Manager of PT Hillconjaya Sakti Project Site PT Adhi Kartiko Pratama Tbk., Mr. Agung Raharjo, as the Engineering Section Head and supervisor, Mrs. Ir. Sufiana, S.T as Head of Mining Engineering, Mr. Naldo Kristian Taula'bi', S.T for the help and data provided during the research.

References

[1] A. Kurniawan, M. Amin, and Bochori, "Pengaruh Geometri Jalan Sebelum dan Setelah Perbaikan Jalan terhadap Produktivitas dan Konsumsi Bahan Bakar serta Rasio Bahan Bakar," *J. Pertamb.*, vol. 3, no. 1, pp. 26–35, 2019.

[2] A. V. Anas, A. Ilyas, R. Amalia, A. Ifthihar, and N. D. Pune, "Mine Haul Road Planning in South West Mahalona Area PT Vale Indonesia Tbk," in *The 4th EPI International Conference on Science and Engineering (EICSE) 2020*, Gowa: AIP Publishing, 2022, pp. 050004–1–050004–9. doi: 10.1063/5.0094757.

[3] F. Tania, M. K. Syafrianto, and S. Setiawati, "Evaluasi Geometri Jalan Angkut Tambang dari Front Penambangan Menuju Lokasi Washing Plant PT Cita Mineral Investindo Tbk (CITA) Kecamatan Sandai Kabupaten Ketapang," *JeLAST J. Tek. Kelautan, PWK, Sipil, dan Tambang*, vol. 8, no. 2, pp. 1–8, 2021, doi: 10.26418/jelast.v8i2.48670.

[4] B. G. Adiwiyuga, D. N. Usman, and Zaenal, "Pengaruh Geometri Jalan terhadap Konsumsi Bahan Bakar pada Penambangan Batubara PT Bima Nusa Internasional Site PT Kideco Jaya Agung di Kecamatan Muara Komam, Kabupaten Paser, Provinsi Kalimantan Timur," in *Bandung Conference Series: Mining Engineering*, 2023, pp. 225–231. doi: 10.29313/bcsme.v3i1.6773 .

[5] A. Saputra, Sumarya, and B. Heriyadi, "Evaluasi dan Perbaikan Jalan Tambang Menggunakan Software Garmin Virb Xe di PT Riung Mitra Lestari Job Site Embalut Kalimantan Timur," *J. Bina Tambang*, vol. 4, no. 3, pp. 22–31, 2019.

[6] R. R. Wincono and J. R. Horman, "Analisis Pengaruh Kemiringan Jalan Angkut terhadap Konsumsi Bahan Bakar Dump Truck Hino 500 FG 235 JJ," *INTAN J. Penelit. Tambang*, vol. 2, no. 2, pp. 155–160, 2019, doi: 10.56139/intan.v2i2.38.

[7] A. W. Pratama and Y. M. Anaperta, "Analisis Hubungan Total Resistance dan Kemiringan Jalan terhadap Konsumsi Bahan Bakar Dump Truck Hino 500 FM 260 JD pada Kegiatan Penambangan Bauksit di PT. Bhakti Karya Mandiri Site Teraju, Kabupaten Sanggau, Provinsi Kalimantan Barat," *J. Bina Tambang*, vol. 5, no. 5, pp. 89–100, 2023.

[8] A. Nelvi, "Analisis Konsumsi Bahan Bakar Truck Mitsubishi Fuso 220 pada Pengangkutan Batubara Berdasarkan Rimpull (Studi Kasus: PT. Haswi Kencana Indah)," *J. Tek. dan Teknol. Tepat Guna*, vol. 2, no. 1, pp. 1–9, 2023, doi: 10.62357/j-t3g.v2i1.141.

[9] M. Su, Z. Su, S. Cao, K.-S. Park, and S.-H. Bae, "Fuel Consumption Prediction and Optimization Model for Pure Car/Truck Transport Ships," *J. Mar. Sci. Eng.*, vol. 11, no. 6, p. 1231, 2023, doi: 10.3390/jmse11061231.

[10] A. Vera-Burau, D. Álvarez-Ramírez, L. Sanmiquel, and M. Bascompta, "A Comparison of the Fuel Consumption and Truck Models in Different Production Scenarios," *Appl. Sci.*, vol. 13, no. 9, p. 5769, 2023, doi: 10.3390/app13095769.

[11] J. J. Posada-Henao, I. Sarmiento-Ordosgoitia, and A. A. Correa-Espinal, "Effects of Road Slope and Vehicle Weight on Truck Fuel Consumption," *Sustainability*, vol. 15, no. 1, p. 724, 2023, doi: 10.3390/su15010724.

[12] Direktorat Jenderal Minyak dan Gas Bumi, "Keputusan Direktur Jenderal Minyak dan Gas Bumi Nomor 146.K/10/DJM/2020 tentang Standar dan Mutu (Spesifikasi) Bahan Bakar Minyak Jenis Solar yang Dipasarkan di Dalam Negeri," Jakarta, 2020.

[13] M. R. Hays, "Trucks," in *Surface Mining*, B. A. Kennedy, Ed., Littleton, CO: Society for Mining, Metallurgy, and Exploration, 1990, pp. 672–691.

[14] Yunita and E. Harsiga, "Analisis Fuel Ratio pada Project Penambangan di Pit 1 PT Cahaya Riau Mandiri Jobsite PT Duta Alam Sumatera," *MINERAL*, vol. 8, no. 1, pp. 39–46, 2023, doi: 10.33019/mineral.v8i1.4097.

[15] K. Awuah-Offei, B. Osei, and H. Askari-Nasab, "Modeling Truck/Shovel Energy Efficiency under Uncertainty," *Trans. Soc. Mining, Metall. Explor.*, vol. 330, pp. 573–584, 2011.

[16] S. R. Dindarloo and E. Siami-Irdemoosa, "Determinants of Fuel Consumption in Mining Trucks," *Energy*, vol. 112, pp. 232–240, 2016, doi: 10.1016/j.energy.2016.06.085.

[17] R. Mubarak, *Pengantar Ekonometrika*, I. Pamekasan: Duta Media Publishing, 2021.

[18] Purnomo *et al.*, *Analisis Data Multivariat*, I. Banyumas: Omera Pustaka, 2022.

EPI International Journal of Engineering
Volume 8, Number 1, February 2025, pp. 26-33
DOI: 10.25042/epi-ije.022025.04

*p*ISSN 2615-5109
*e*ISSN 2621-0541

Preliminary Design and Energy Production of a Mobile Floating Structure (MFS) for Offshore Wind Turbines in Indonesian Waters

Muhammad Uswah Pawara[a,*], Chris Jeremy Verian Sitorus[b], Hariyono[c], Andi Mursid Nugraha Arifuddin[d], Alamsyah[e], Taufik Hidayat[f], Suardi[g], Abdul Mujib Syadzali[h], Faisal Mahmuddin[i]

[a]Naval Architecture Program, Kalimantan Institute of Technology. Email: uswah.pawara@lecturer.itk.ac.id
[b]Naval Architecture Program, Kalimantan Institute of Technology. Email: chris.sitorus@lecturer.itk.ac.id
[c]Naval Architecture Program, Kalimantan Institute of Technology. Email: hariyono@lecturer.itk.ac.id
[d]Naval Architecture Program, Kalimantan Institute of Technology. Email: andi.mursid@lecturer.itk.ac.id
[e]Naval Architecture Program, Kalimantan Institute of Technology. Email: alamsyah@lecturer.itk.ac.id
[f]Naval Architecture Program, Kalimantan Institute of Technology. Email: taufik.hidayat@lecturer.itk.ac.id
[g]Naval Architecture Program, Kalimantan Institute of Technology. Email: suardi@lecturer.itk.ac.id
[h]Civil Engineering Program, Kalimantan Institute of Technology. Email: abdul.mujib@lecturer.itk.ac.id
[i]Marine Engineering Department, Hasanuddin University. Email: fmahmuddin@gmail.com

Abstract

The Mobile Floating Structure (MFS) is an innovative floating wind turbine concept that utilizes a catamaran hull design to enhance mobility and operational efficiency. Unlike stationary platforms, the MFS can relocate to areas with higher wind energy density, making it a promising solution for optimizing wind energy harvesting in offshore environments. This study focuses on the preliminary design and energy production of the MFS. Maxsurf is used to analyze hydrostatics and assess the hydrodynamic performance of the MFS hull after the dimension of the MFS is determine with key considerations including rotor diameter and the weight of the wind turbine. Furthermore, four wind turbines are installed in the MFS. Those aspect were integrated into the design process to ensure realistic operational adaptability. As result. the resulting dimensions of the MFS were determined utilizing Maxsurf. Moreover, different with the previous study that use satellite data, the present study employs reanalysis data to estimate the energy density and power production of MFS. the energy density map is also produced in the present study to determine the monthly location of the MFS. The energy production of the MFS with four turbines has been calculated, and the energy production map is also drawn. Finally, the energy production of the MFS in the chosen location has also been estimated. The energy production map can be utilized to develop MFS in other location.

Keywords: Floating wind turbine; MFS; platform design; energy production

1. Introduction

The global demand for sustainable energy solutions has driven significant advancements in renewable energy technologies, with wind energy emerging as a key contributor. Floating wind turbine platforms, particularly in offshore locations, offer a promising solution to harness wind energy more effectively [1]. Mobile Floating Structure (MFS) stands out as an innovative approach, leveraging the twin-hull or catamaran design for enhanced mobility and operational efficiency [2]. Unlike fixed or location-specific platforms, the MFS can relocate to areas with higher wind energy density, making it a versatile and effective option for energy harvesting [3].

*Corresponding author. Tel.: +62-821-9555-0414
Institut Teknologi Kalimantan, Jl. Soekarno Hatta No.KM 15, Balikpapan, Indonesia, 76127

Mobile Floating Structure (MFS) is a concept for a floating wind turbine that adopts the catamaran hull design. Its primary advantage lies in its ability to relocate to areas with higher wind energy density, thereby enhancing the effectiveness and optimization of wind energy harvesting. Previous studies have analyzed the potential for wind energy in several Indonesian waters, identifying ideal locations for MFS installations, such as the Java Sea near Sulawesi Island, where optimal wind conditions are observed during January and February [4], [5].

While wind energy conversion systems have been extensively explored in prior research—including land-based systems [6], and sea-based systems [7], [8], many existing prototypes remain confined to specific locations. This limitation can lead to efficiency losses due to seasonal variations in wind speed and distribution. The MFS addresses this issue through its mobility, which

allows it to access areas with consistently higher wind energy density. A similar approach has been implemented in Japan with the concept of a Very Large Mobile Offshore Structure (VLMOS) [9]. The initial concept and primary design of the MFS have been developed [2]. However, further refinements are required to adapt the design to the dynamic and diverse conditions of Indonesian waters. Additional considerations, such as the weight of the turbine on the MFS deck, must be integrated into the design process. As part of ongoing development, the MFS concept has been redesigned and submitted as a simple patent [10].

This study aims to advance the MFS design into a more efficient, sustainable model tailored to the unique conditions of Indonesian waters. Using advanced tools like Maxsurf for hydrostatic performance, this research seeks to optimize the MFS's operational efficiency and hull design accounting for the turbine's weight and dimension. Furthermore. Energi production that can be harnessed by MFS is estimated. After producing the MFS model and determining the main dimension, the energy production is calculated using reanalysis data. The result of the study would be beneficial to choose suitable location of MFS and to develop the MFS further.

2. MFS Design

The design and analysis of the Mobile Floating Structure (MFS) for wind turbines in Indonesian waters based on turbine dimension and characteristic. This procedure ensures that the platform can accommodate the turbines, key stages of the design are as follows:

2.1. MFS platform design

This step begins with defining the MFS's main dimensions, including length (L), breadth (B), height (H), and draft (T). These dimensions are calculated based on the weight of the wind turbine, the span of its blades, and other technical considerations.

2.2. Body plan design

After the main dimensions established, the next step involves designing the lines plan, which provides a blueprint for the hull's geometry. This design serves as the foundation for creating the body plan, detailing the precise shape of the MFS hull. The process leverages Maxsurf software to optimize both the lines plan and the body plan for hydrodynamic efficiency. At the end of this stage, an initial model of the MFS is completed, ready for further analysis.

2.3. Hydrostatic analysis

The initial MFS design undergoes detailed hydrostatic analysis to assess its performance in operational conditions. Hydrostatic analysis is conducted using Maxsurf producing hydrostatic performance and parameters. These analyses ensure that the MFS design is optimized for the marine environment, providing insights into its operational efficiency and feasibility.

3. MFS Power Production

3.1. Research location and data

The research location is the same as the previous study [3], which is in the waters around the islands of Sulawesi and Maluku, within the range of 116°E – 132°E and 8°N – 10°S . To determine the amount of wind energy generated by the MFS, this study uses 11 years of ERA-Interim Reanalysis data from 1999 to 2009, whereas the previous study utilized satellite data [3]. Era Interim reanalysis data is reanalysis product provided by ECMWF (European Centre for Medium-Range Weather Forecasts) [11]. The ERA-Interim has been intensively used to assess offshore wind energy in various location in the world [12-16]. The data with a temporal resolution of 6 h, and a spatial resolution of 0.25° × 0.25° were employed. Figure 1 displays the time series of 10m u-component wind at latitude: -5, and longitude: 120 in January 2009.

3.2. Wind energy density

The magnitude of wind speed on each pixel was obtained using the following equation [17].

$$V = \sqrt{u^2 + v^2} \quad (1)$$

where, V is the magnitude of wind speed at a height of 10 m (m/s); u is the is the East-West wind component and v is the wind component u (North-South). This was done over the entire time series and all pixels of the study area.

Wind energy density is defined as the power on the unit section perpendicular to the flow. It was obtained using the following equation.

$$W = 1/2\rho V^3 \quad (2)$$

In Eq. (3), W is wind power density (W/m2), V is the magnitude of wind speed at a height of 10 m (m/s), and ρ is air density (kg/m3), taken here as 1.225 kg/m3 as the sea surface air density.

3.3. Wind power production estimation

To determine the total energy production of the platform the turbine that used in previous study is selected which is NM72/2000 manufactured by NEG Micon, the specification of the turbine is given in Table 1.

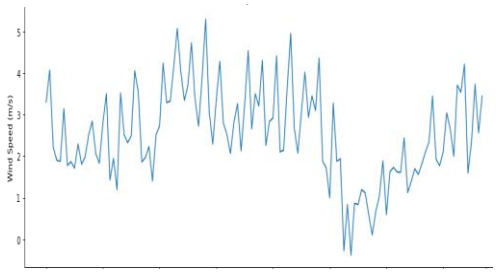

Figure 1. Time series data

Table 1. NM72/2000 turbine data [18]

Parameter	Unit
Hub height	64 m
Rated power	2 MW
Cut in speed	2 m/s
Rated speed	14 m/s
Cut out speed	25 m/s
Rotor diameter:	72.0 m
Rotor swept area:	4,072.0 m²

This study determines power generation based on the wind speed data and a selected wind turbine's characteristic. The power curve of the selected turbine is described by:

$$\begin{cases} 0, & 0 \le v \le v_{ci} \\ P_R(A + B_v + Cv^2), & v_{ci} \le v \le v_r \\ P_R\,, & v_r \le v \le v_{co} \\ 0\,, & v > v_{co} \end{cases} \quad (3)$$

where,
v_{ci}, v_r v_{co} Cut-in, rated, and cut-out speeds
A, *B*, *C*: Coefficients fitted to the turbine's power curve.

The coefficients *A*, *B*, *C* are calculated using the following equations:

$$A = \frac{1}{(v_r - v_{ci})^2}\left[v_{ci}\,(v_{ci} + v_r) - 4v_{ci}v_r\left(\frac{v_{ci} + v_r}{2v_r}\right)^3\right]$$

$$B = \frac{1}{(v_r - v_{ci})^2}\left[4\,(v_{ci} + v_r)\left(\frac{v_{ci}+v_r}{2v_r}\right)^3 - (3v_{ci} + v_r)\right] \quad (4)$$

$$C = \frac{1}{(v_r - v_{ci})^2}\left[2 - 4\left(\frac{v_{ci} + v_r}{2v_r}\right)^3\right]$$

4. Results and Discussion

4.1. MFS platform model

MFS platform is designed based on the concept in the previous study [2], the concept of catamaran with dual hull is still adopted in the present study. Furthermore, four wind turbines is installed on the platform, and two barges are used to accommodate four wind turbines. Based on the consideration, the preliminary design of MFS has been performed. The model of the platform is given in Fig. 2.

4.2. MFS Main Dimension and Body Plan

The dimension of hull is determined based on turbine dimension specifically blade expansion or rotor diameter. By referring the turbine general data that is given in Tabel 1, the main dimension of the MFS is estimated and modeled in Maxsurf. After modifying the model, the final dimensions of the MFS can be determined. The main dimension of the MFS is given in Tabel 2, and the result of body plan design of the MFS using Maxsurf is shown in Fig. 3.

.

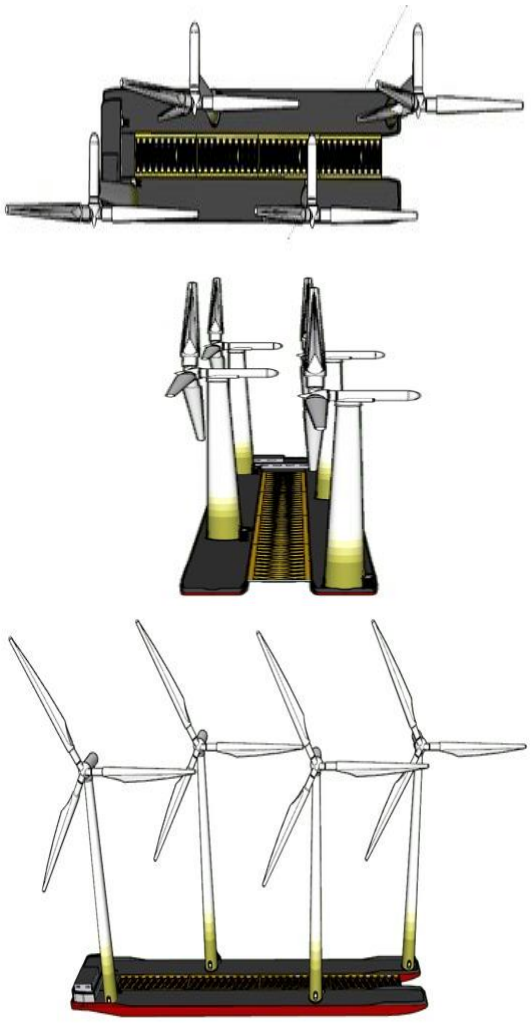

Figure 2. MFS platform

Table 2. MFS main dimension

Parameter	Unit
Lwl	128 m
H	4 m
B	8 m
T	3.2 m

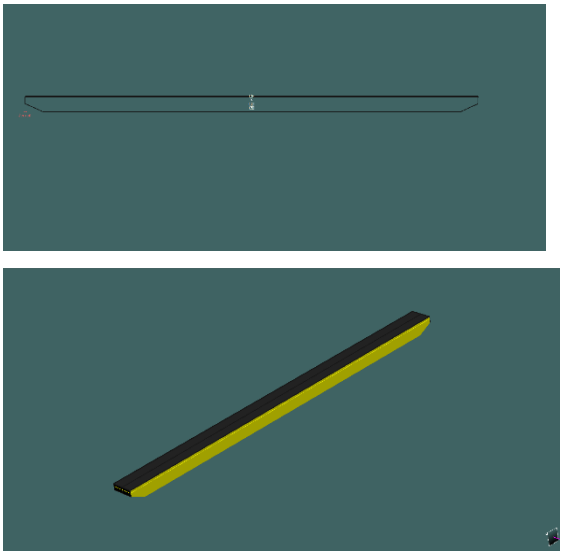

Figure 3. MFS body plan

4.3. Lines plan and hydrostatic performance

The body plan that has been produced is used to draw the lines plan of MFS hull. The lines is important because it used to analyze the hydrostatic characteristic of a floating platform. The resulted lines plane is given in Figure 4. The initial analysis of hydrostatic performance is also has been performed and the result is given in Fig. 4.

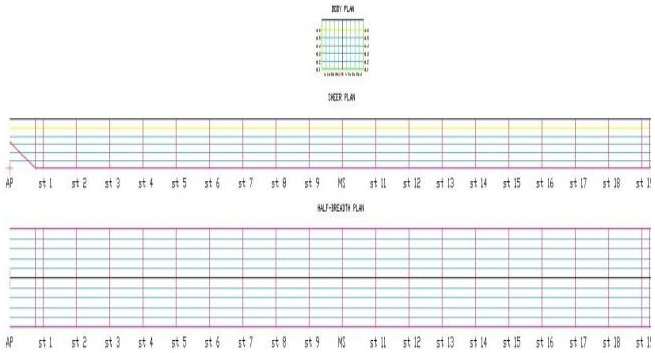

(a) lines plan;

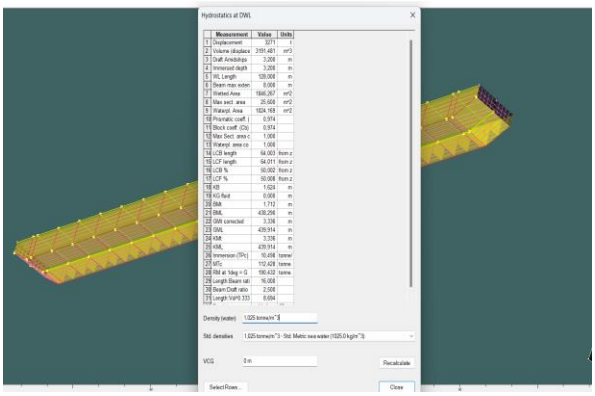

(b) hydrostatic characteristic.

Figure 4. (a) lines plan; (b) hydrostatic characteristic

4.4. Wind energy density map

Previous study used Weibull Distribution to determine energy density. In the present study, Eq. 2 is used to estimate the energy density. After the energy density each location is calculated, the wind energy density maps are produced.

The monthly wind energy maps are shown in Fig. 5.

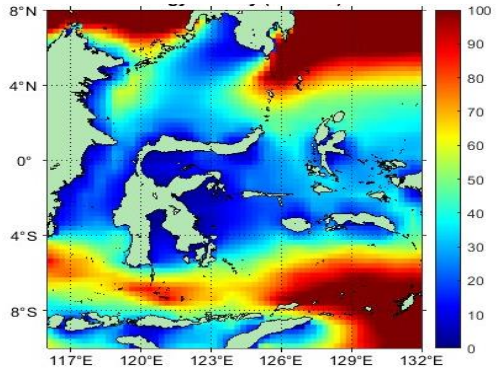

(a) January

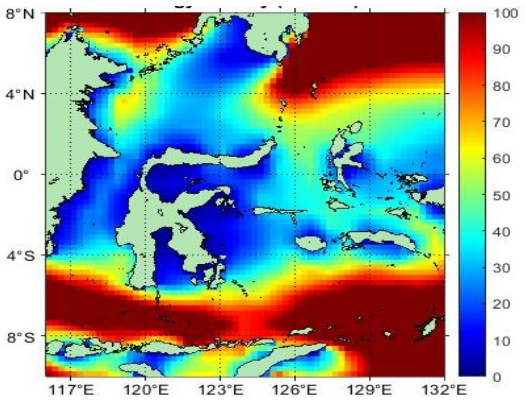

b. February

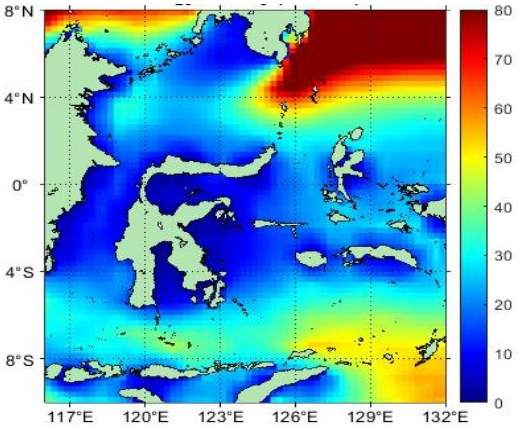

(c) March

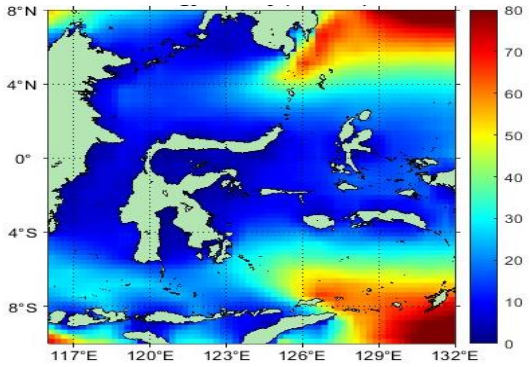

(d) Apr

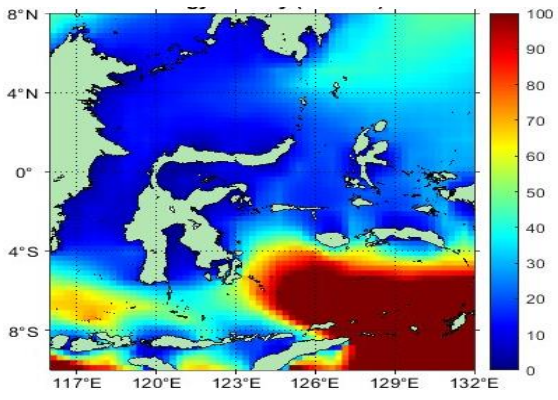

(e) May

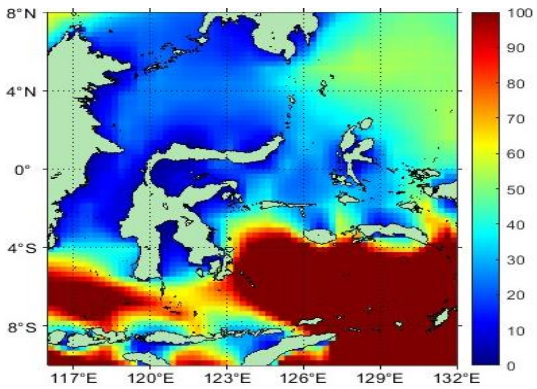

(f) June

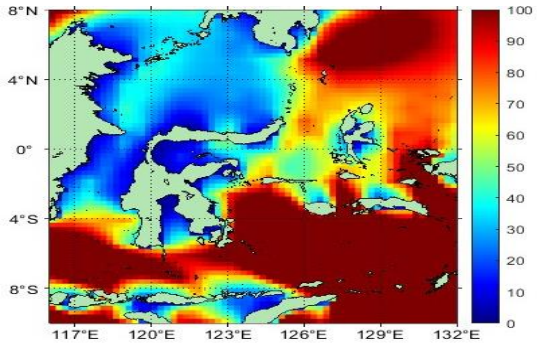

(g) July

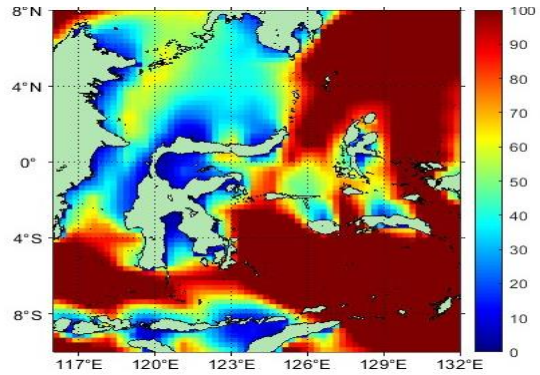

(h) August

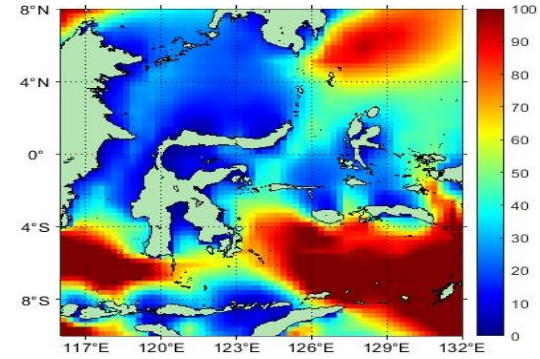

(i) September

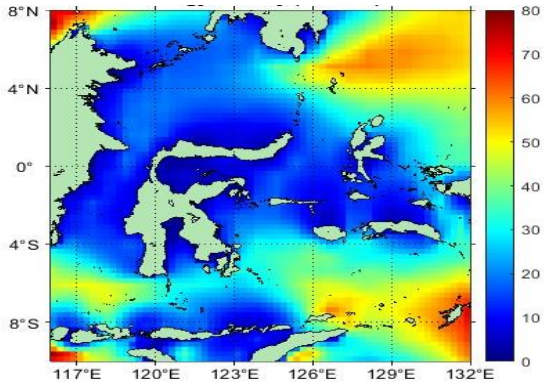

(j) October

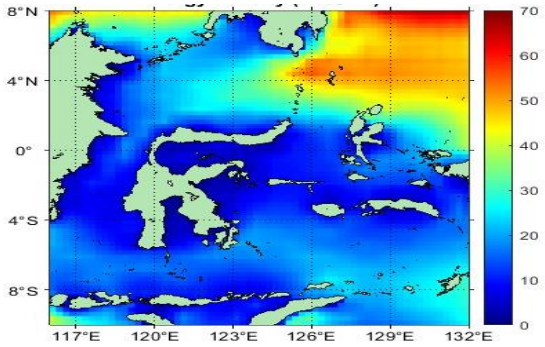

(k) November

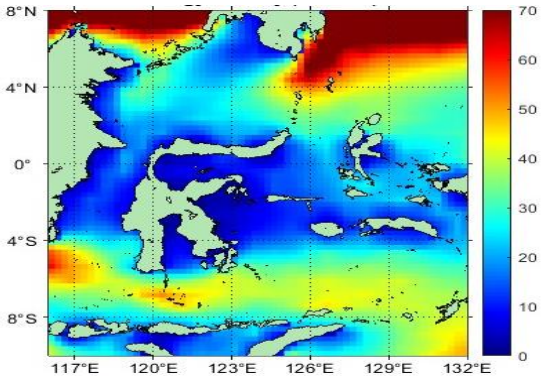

(l) Dec

Figure 5. Monthly power density map

Figure 5 shows that the energy density of the research location which is in the Sulawesi and Maluku Island is around 40-100 watt/m^2. Moreover, it can be seen that Jan – Feb and Jun – August are suitable time to harness the energy.

From the figures, it is important to note that the result of energy density in the present study seems lower than in the previous study. It could be caused that the adopted method to determine energy density and the used data are difference. It also can be concluded that the reanalysis data underestimate the wind speed in Indonesia if it is compared to the previous study using satellite data.

Furthermore, the density map is used to determine monthly MFS location. Tabel 3 is information on monthly MFS location.

Table 3. Monthly MFS location

Month	Longitude	Latitude	Energy Density (Watt/m^2)
January	121.00°	-7.25°	88.81
February	118.00°	-7.25°	137.94
March	126.00°	5.00°	97.45
April	126.50°	-7.25°	65.23
May	125.00°	-6.50°	123.05
June	125.00°	-6.00°	188.22
July	126.00°	-6.00°	261.19
August	125.75°	-4.00°	186.91
September	117.25°	-6.00°	134.48
October	117.50°	-6.00°	49.22
November	126.00°	4.50°	54.85
December	126.00°	5.25°	77.56

4.5. MFS energy production

The energy production of the MFS with four turbine is estimated using wind speed data and power curve in Eqs. 3 and 4. The energy production of the MFS in the research location in the Sulawesi and Maluku Island has been determined, the monthly map is also has been drawn, the map can be used as reference to develop MFS in other location. The map of MFS energy production with four turbine is shown in Fig. 6.

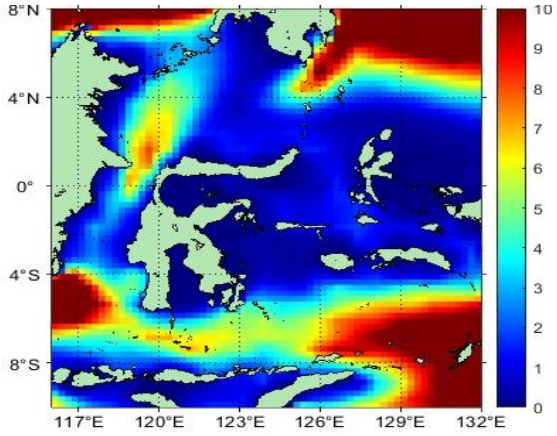

(a) January

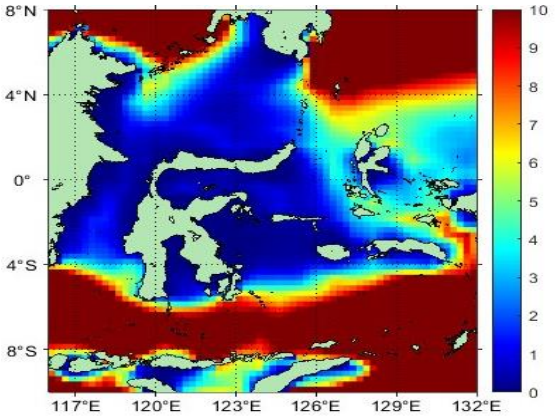

(b) February

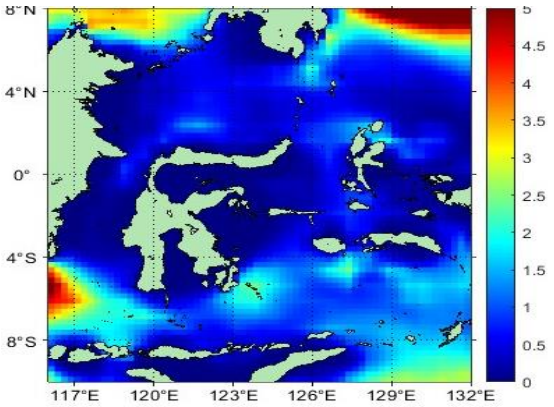

(c) March

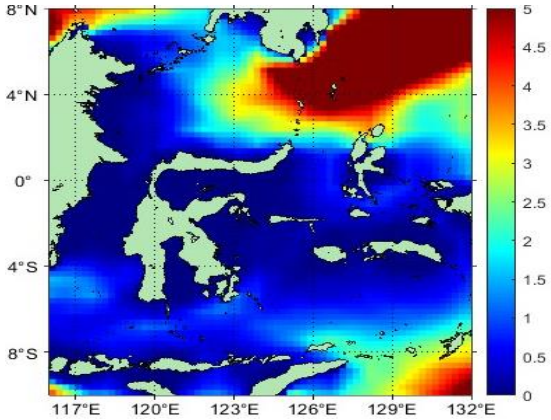

(d) April

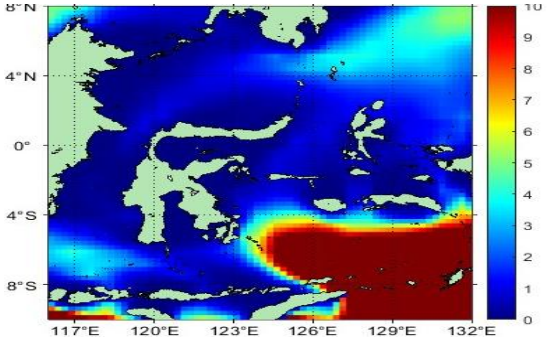

(e) May

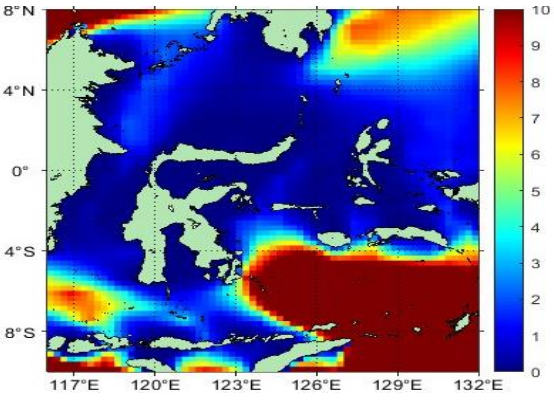

(f) June

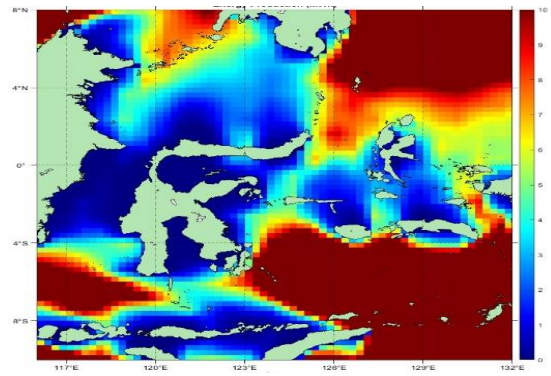

(g) July

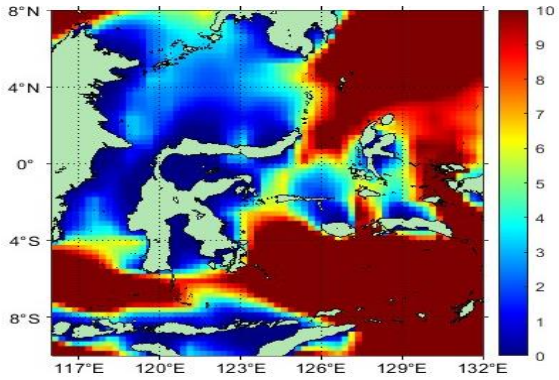

(h) August

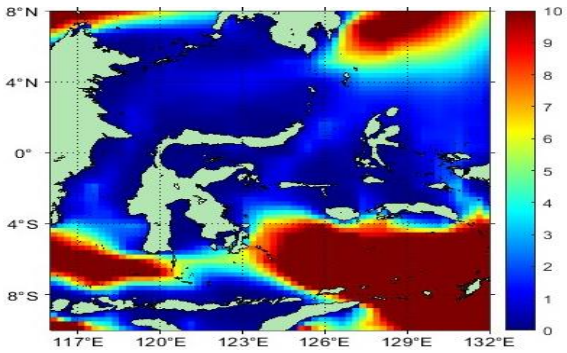

(i) September

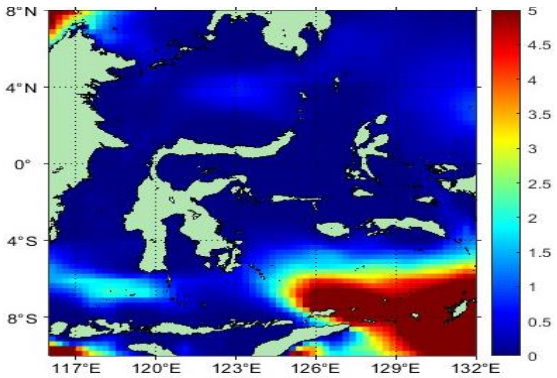

(j) October

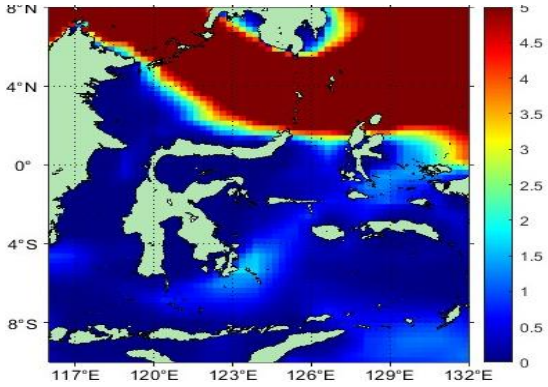

(k) November

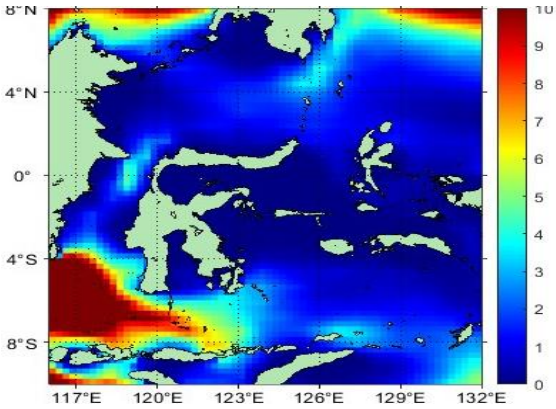

(l) December

Figure 6. Energy production map

Form Fig. 6, the energy production from the monthly location of MFS is also can be calculated. The monthly energy production of MFS in the chosen location has been estimated and it is given in Table 5. Based on Table 5, the maximum energy production is in July.

Table 5. The expected power production.

Month	Total power production KWh	Expected Power (KW)	Power Percentage (%)
January	9260.94	385.87	19.29
February	10768.50	448.69	22.43
March	10245.65	426.90	21.35
April	6187.34	257.81	12.89
May	13571.74	565.49	28.27
June	20495.91	854.00	42.70
July	29808.80	1242.03	62.10
August	21127.29	880.30	44.02
September	14142.05	589.25	29.46
October	4211.88	175.50	8.77
November	4649.01	193.71	9.69
December	7705.81	321.08	16.05

5. Conclusion

This study presents the preliminary design and energy production analysis of a Mobile Floating Structure (MFS) tailored for offshore wind energy harvesting in Indonesian waters. By employing a catamaran-based platform equipped with four NM72/2000 wind turbines, and utilizing Maxsurf software for hydrostatic and hydrodynamic analysis, the design ensures both structural efficiency and operational feasibility. The innovative mobility feature of the MFS allows it to be relocated seasonally to optimize energy capture, with energy density and power production assessed using 11 years of ERA-Interim reanalysis data. The results demonstrate significant variation in monthly energy potential, with peak production occurring in July. Although the reanalysis data slightly underestimates wind energy compared to satellite-based methods, the findings validate the MFS as a promising solution for dynamic and sustainable offshore wind energy exploitation. The energy production and location maps produced in this study can serve as strategic tools for future deployment planning and further development of mobile offshore renewable energy systems in Indonesia.

Acknowledgements

This research was funded by Institute for Research and Community Service (LPPM) ITK through Internal Grant 2024 with contract number 4340/IT10.II/PPM.04/2024.

References

[1] E. C. Edwards, A. Holcombe, S. Brown, E. Ransley, M. Hann, and D. Greaves, "Evolution of floating offshore wind platforms: A review of at-sea devices," *Renew. Sustain. Energy Rev.*, vol. 183, no. May, p. 113416, 2023, doi: 10.1016/j.rser.2023.113416.

[2] M. U. Pawara and F. Mahmuddin, "Developing a Mobile Floating Structure as an Offshore Wind Energy Harvesting System in Indonesia Sea Areas," *Proc. 3rd Int. Conf. Adv. Mech. Eng.*, no. December, pp. 835–841, 2017.

[3] F. Mahmuddin, "Analysis of wind energy potential with a mobile floating structure around Sulawesi and Maluku Islands of Indonesia," *Proc. Int. Conf. Offshore Mech. Arct. Eng. - OMAE*, vol. 9, no. April, 2015, doi: 10.1115/OMAE2015-41588.

[4] F. Mahmuddin, "Mapping ocean wind energy potential around Sulawesi and Maluku islands," *RINA, R. Inst. Nav. Archit. - Int. Conf. Sh. Offshore Technol. ICSOT 2014 Dev. Sh. Des. Constr.*, no. November 2014, pp. 81–86, 2014.

[5] F. Mahmuddin, M. Idrus, and Hamzah, "Analysis of Ocean Wind Energy Density around Sulawesi and Maluku Islands with Scatterometer Data," *Energy Procedia*, vol. 65, pp. 107–115, 2015, doi: 10.1016/j.egypro.2015.01.041.

[6] R. Huva, R. Dargaville, and S. Caine, "Prototype large-scale renewable energy system optimisation for Victoria, Australia," *Energy*, vol. 41, no. 1, pp. 326–334, 2012, doi: https://doi.org/10.1016/j.energy.2012.03.009.

[7] S. Lefebvre and M. Collu, "Preliminary design of a floating support structure for a 5MW offshore wind turbine," *Ocean Eng.*, vol. 40, pp. 15–26, 2012, doi: https://doi.org/10.1016/j.oceaneng.2011.12.009.

[8] J. Park, J. Kim, Y. Shin, J. Lee, and J. Park, "3MW class offshore wind turbine development," *Curr. Appl. Phys.*, vol. 10, no. 2, Supplement, pp. S307–S310, 2010, doi: https://doi.org/10.1016/j.cap.2009.11.032.

[9] K. Takagi, "Hydroelastic Behavior of VLMOS In Beam Seas," May 23, 2004.

[10] M. U. Pawara and F. Mahmuddin, "Turbin angin terapung berbasis kapal lambung ganda," 2023

[11] D. P. Dee *et al.*, "The ERA-Interim reanalysis: Configuration and performance of the data assimilation system," *Q. J. R. Meteorol. Soc.*, vol. 137, no. 656, pp. 553–597, 2011, doi: 10.1002/qj.828.

[12] G. Nagababu, S. S. Kachhwaha, N. K. Naidu, and V. Savsani, "Application of reanalysis data to estimate offshore wind potential in EEZ of India based on marine ecosystem considerations," *Energy*, vol. 118, pp. 622–631, 2017, doi: https://doi.org/10.1016/j.energy.2016.10.097.

[13] M. M. Nezhad *et al.*, "A primary offshore wind farm site assessment using reanalysis data: a case study for Samothraki island," *Renew. Energy*, vol. 172, no. x, pp. 667–679, 2021, doi: 10.1016/j.renene.2021.03.045.

[14] H. G. Kim, J. Y. Kim, and Y. H. Kang, "Comparative evaluation of the third-generation reanalysis data for wind resource assessment of the Southwestern offshore in South Korea," *Atmosphere (Basel).*, vol. 9, no. 2, 2018, doi: 10.3390/atmos9020073.

[15] M. M. Nezhad, M. Neshat, A. Heydari, A. Razmjoo, G. Piras, and G. D. Astiaso, "A new methodology for offshore wind speed assessment integrating Sentinel-1, ERA-Interim and in-situ measurement," *Renew. Energy*, 2021, doi: 10.1016/j.renene.2021.03.026.

[16] A. Raileanu, F. Onea, and E. Rusu, "Assessment of the wind energy potential in the coastal environment of two enclosed seas," in *OCEANS 2015 - Genova*, 2015, pp. 1–8. doi: 10.1109/OCEANS-Genova.2015.7271248.

[17] C. Mattar and M. C. Guzmán-Ibarra, "A techno-economic assessment of offshore wind energy in Chile," *Energy*, vol. 133, pp. 191–205, 2017, doi: https://doi.org/10.1016/j.energy.2017.05.099.

[18] "NEG Micon NM 72/2000 - 2,00 MW - Wind turbine." Accessed: Apr. 22, 2025. [Online]. Available: https://en.wind-turbine-models.com/turbines/62-neg-micon-nm-72-2000.

EPI International Journal of Engineering
Volume 8, Number 1, February 2025, pp. 34-44
DOI: 10.25042/epi-ije.022025.06

*p*ISSN 2615-5109
*e*ISSN 2621-0541

Design of Quasi-isotropic Rectangular Plates for Optimizing the Fundamental Mode of Bending Vibration

Yoshihiro Narita[a,*]

[a]Hokkaido University (Professor Emeritus), Sapporo, Japan. Email: ynarita1951@gmail.com

Abstract

This study is the first work to demonstrate that quasi-isotropic laminated composite plates can be optimized for bending vibration through appropriate stacking sequence design. A quasi-isotropic plate is defined as a laminated composite plate exhibiting isotropic in-plane stiffness. Owing to this constraint, such plates have traditionally been excluded from stacking sequence optimization. The present work clarifies why optimization remains feasible despite the in-plane isotropy requirement and outlines a systematic procedure for maximizing or minimizing the fundamental natural frequency with respect to ply orientation angles while preserving isotropic in-plane behavior. Numerical results are provided for square and rectangular plates under various classical boundary conditions, and the corresponding maximum and minimum fundamental frequencies are identified. In particular, the ratio of maximum to minimum fundamental frequency is evaluated; for example, it reaches 2.17 for a cantilevered quasi-isotropic square plate.

Keywords: Free vibration; rectangular plate; quasi-isotropy; stacking sequence optimization; fundamental frequency

1. Introduction

Laminated composite plates are widely used as structural components in aeronautical and other advanced engineering applications [1–3]. Their high specific strength and stiffness allow significant weight reduction, and they provide considerable potential for structural optimization through stacking-sequence tailoring [4–6]. In vibration design, the stacking sequence can be adjusted to control dynamic behavior; for example, the fundamental natural frequency may be maximized to prevent resonance [7–12].

In contrast, a certain type of laminated plates is designed to suppress anisotropy by adopting specific stacking sequences, since structural plate elements may be subjected to in-plane loads acting in uncertain directions. Such laminates are referred to quasi-isotropic plates, and they have been investigated from various perspectives. Fukunaga [13] studied a class of laminated composites that present isotropic stiffness with respect to both in-plane and out-of-plane stiffnesses. Paradies [14] proposed a method for laminated composites with quasi-isotropic stiffness, and derived the diagram of quasi-isotropic laminates. Akkerman [15] derived the three-dimensional thermoelastic properties of quasi-isotropic laminates in closed form equations. Douglas et al. [16] studied the experimental determination of the elastic modulus of a quasi-isotropic laminate by tensile mechanical testing. Vannucci and Verchery [17] proposed new kinds of isotropic laminates composed of identical anisotropic layers to obtain fully isotropy. Altunsaray and Bayer [18] studies the maximum deflection and free vibration of quasi-isotropic clamped or supported rectangular plates.

By the present definition, a quasi-isotropic laminate is designed to exhibit identical in-plane stiffness in all directions; that is, its in-plane stiffness remains the same regardless of the loading direction within the laminate plane. This character is achieved by orienting individual layers at different angles—for example, 0°, 45°, 90°, and −45° relative to a reference direction, as illustrated in Fig. 1. Nevertheless, the out-of-plane (bending) stiffness of the laminate remains anisotropic. In other words, although the laminate behaves isotropically under in-plane loading, it still exhibits directional dependence in bending vibration.

The present study considers quasi-isotropic plates as candidates for stacking-sequence optimization for the first time. Numerical investigations demonstrate that the fundamental bending frequency can be designed through appropriate stacking sequence under quasi-isotropic constraints. These results confirm that layer-sequence optimization is both effective and feasible for quasi-isotropic rectangular plates.

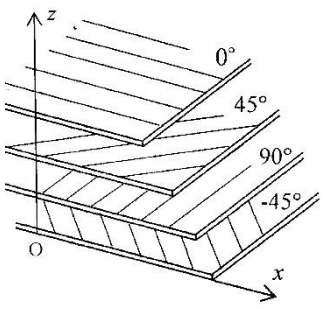

Figure 1. Example of upper half stacking design in a quasi-isotropic symmetric 8-layer laminated plate [0°/45°/90°/-45°]s

*Corresponding author.
Hokkaido University, N-13, W-8, Sapporo
Japan

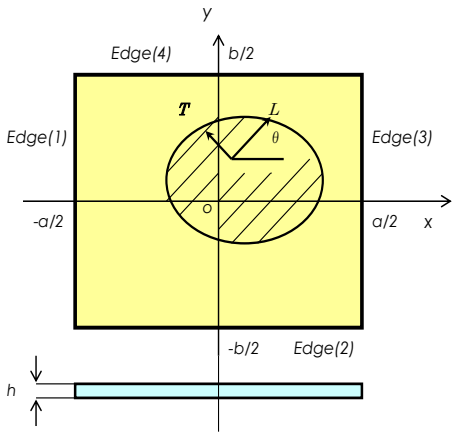

Figure 2. Rectangular plate in the coordinate system

2. Theory

2.1 Quasi-isotropic plate

The present paper deals with quasi-isotropic plates that fall into a class of symmetrically laminated plates with specific stiffness property. In each layer, the stress-strain relation is given in the *k*-th layer [1,2] by

$$\begin{Bmatrix}\sigma_x\\ \sigma_y\\ \tau_{xy}\end{Bmatrix}^{(k)} = \begin{bmatrix}\bar{Q}_{11} & \bar{Q}_{12} & \bar{Q}_{16}\\ \bar{Q}_{12} & \bar{Q}_{22} & \bar{Q}_{26}\\ \bar{Q}_{16} & \bar{Q}_{26} & \bar{Q}_{66}\end{bmatrix}^{(k)} \begin{Bmatrix}\varepsilon_x\\ \varepsilon_y\\ \gamma_{xy}\end{Bmatrix} \tag{1}$$

where σ_x, σ_y and τ_{xy} are normal and shear stresses, and $\varepsilon_x, \varepsilon_y$ and γ_{xy} are normal and shear strains, respectively. $\bar{Q}_{ij}^{(k)}$ (i, j=1,2,6) are the material constants obtained by

$$\begin{aligned}
Q_{11}^{(k)} &= Q_{11}l^4 + 2\left(Q_{12}+2Q_{66}\right)l^2m^2 + Q_{22}m^4\\
\bar{Q}_{12}^{(k)} &= Q_{12}\left(l^4+m^4\right) + \left(Q_{11}+Q_{22}-4Q_{66}\right)l^2m^2\\
\bar{Q}_{22}^{(k)} &= Q_{11}m^4 + 2\left(Q_{12}+2Q_{66}\right)l^2m^2 + Q_{22}l^4\\
\bar{Q}_{16}^{(k)} &= \left(Q_{11}-Q_{12}-2Q_{66}\right)l^3m - \left(Q_{22}-Q_{12}-2Q_{66}\right)lm^3\\
\bar{Q}_{26}^{(k)} &= \left(Q_{11}-Q_{12}-2Q_{66}\right)lm^3 - \left(Q_{22}-Q_{12}-2Q_{66}\right)l^3m\\
\bar{Q}_{66}^{(k)} &= \left(Q_{11}+Q_{22}-2Q_{12}-2Q_{66}\right)l^2m^2 + Q_{66}\left(l^4+m^4\right)
\end{aligned} \tag{2}$$

with $l=\cos\theta_k$ and $m=\sin\theta_k$, and are expressed in the x and y directions by considering a fiber orientation angle θ_k (with respect to the x axis) from the constants

$$Q_{11} = \frac{E_L}{1-\nu_{LT}\nu_{TL}}, Q_{22} = \frac{E_T}{1-\nu_{LT}\nu_{TL}},$$
$$Q_{12} = Q_{11}\nu_{TL} = Q_{22}\nu_{LT}, Q_{66} = G_{LT} \tag{3}$$

Here, the subscript L indicates the direction along straight fiber and T does the direction perpendicular to the L axis in the plane. E_L and E_T are young's modulus in the L and T directions, respectively. ν_{LT}, ν_{TL} are the major and minor Poisson's ratios, and G_{LT} is a shear moduli.

In the following numerical examples, a set of constants

$$E_L = 150 \text{ GPa}, E_T = 10 \text{ GPa},$$
$$G_{LT} = 5 \text{ GPa}, \nu_{LT} = 0.3 \tag{4}$$

are used that are the averaged values from a few modern typical CFRP sheets [19].

In the classical lamination theory [1], the in-plane stiffness and bending stiffness are defined by

$$A_{ij} = \sum_{k=1}^{K} \bar{Q}_{ij}^{(k)}\left(z_k - z_{k-1}\right),$$
$$D_{ij} = \frac{1}{3}\sum_{k=1}^{K} \bar{Q}_{ij}^{(k)}\left({z_k}^3 - {z_{k-1}}^3\right) \tag{5}$$

where K indicates the total number of layers. It is seen that the A_{ij} (i,j=1,2,6) is proportional to z and the D_{ij} (i,j=1,2,6) is to z powered by three.

There is a certain class of laminates that result in $A_{11}=A_{22}$ and $A_{16}=A_{26}=0$, for example in Fig.1, [0/45°/90°/-45°]$_S$ (s denotes symmetric laminate about the mid-plane) with each layer having the same thickness. This specially laminated plate is called "a quasi-isotropic plate", since the plate is uniformly isotropic in the plane (tension). It is noted, however, that the bending stiffness D_{ij} in this case cannot be identical due to "cubic power" of z in Eq.(5) and outer layers contribute more to the bending stiffness of the whole plate.

By generalizing this idea, the following laminated plates are also regarded as quasi-isotropic plates.

Six-layer plate:

$$\left[\theta_1/\theta_2/\theta_3\right]_S, \quad \theta_i \in \left\{\theta_1-60^\circ, \theta_1+60^\circ\right\} \quad (i=2,3) \tag{6}$$

Eight-layer plate:

$$\left[\theta_1/\theta_2/\theta_3/\theta_4\right]_S$$
$$\theta_i \in \left\{\theta_1-45^\circ, \theta_1+45^\circ, \theta_1+90^\circ\right\} \quad (i=2,3,4) \tag{7}$$

Ten-layer plate:

$$\left[\theta_1/\theta_2/\theta_3/\theta_4/\theta_5\right]_S$$
$$\theta_i \in \left\{\theta_1-72^\circ, \theta_1-36^\circ, \theta_1+36^\circ, \theta_1+72^\circ\right\} \quad (i=2,3,4,5) \tag{8}$$

Twelve-layer plate:

$$\left[\theta_1/\theta_2/\theta_3/\theta_4/\theta_5/\theta_6\right]_S$$
$$\theta_i \in \left\{\theta_1-60^\circ, \theta_1-30^\circ, \theta_1+30^\circ, \theta_1+60^\circ, \theta_1+90^\circ\right\}$$
$$\left(i=2,3,4,5,6\right) \tag{9}$$

where θ_1 is any angle (real number) on $-90^\circ < \theta_1 \le 90^\circ$ but for clarity, it is here assumed to be with an increment of $\Delta\theta_1$=5° (i.e., $\theta_1 = -85^\circ,..,0^\circ,5^\circ,10^\circ,..,90^\circ$) or $\Delta\theta_1$=15°.

For example in Eq.(9), θ_1 is a fiber orientation angle of the outer-most layer, θ_2 is an fiber angle of the second outer layer, and θ_6 is an fiber angle of the inner-most layer. So the sequence in bracket [ ] is technically important. In contrast, $\theta_i \in \{\ \}$ simply means that θ_i 's (i=2,3,..) is chosen once among elements in parenthesis { }.

In computation, the fiber angle θ_1 of outer most layer takes discrete values with $\Delta\theta_1$=5° or 15°, and layers in the second and inner layers are taken to satisfy the assumption of in-plane isotropic. For example, when θ_1 of the

outermost layer is taken as θ_1=10°, a six-layer plate chooses θ_2 and θ_3 from {-50°,70°}, and an eight-layer plate does θ_2, θ_3 and θ_4 from {-35°,55°,-80°}. Similarly, a ten-layer plate takes on among {-62°,-26°,46°,82°}, and a twelve-layer plate does among {-50°,-20°,40°,70°,-80°}. All the fiber angles are adjusted to stay within $-90° < \theta \le 90°$, for example, 105° is replaced by -75° (so, the fiber orientation angle is physically identical).

All the fiber angles written in Eqs.(6)-(9) satisfy the stiffness condition (A_{11}=A_{22} and A_{16}=A_{26}=0) as a quasi-isotropic plate, namely, the in-plane stiffnesses in x and y directions are identical, but the bending (out-of-plane) stiffnesses are anisotropic. This is the reason why the laminated quasi-isotropic plates can be a target for stacking sequence optimization in bending frequencies, although "isotropy" may sound far from the stacking sequence optimization.

2.2 Optimization

The frequency parameter for the bending fundamental (lowest) mode is used as an objective function and is maximized or minimized in the present design problem. The design variables are taken to be a set of fiber orientation angles in the K/2 layers of the upper (lower) half of the cross-section. The design problem is stated as

Maximize the frequency parameter Ω_1
subject to the constraints
that A_{11}=A_{22} and A_{16}=A_{26}=0. (10)

or

Minimize the frequency parameter Ω_1
subject to the constraints
that A_{11}=A_{22} and A_{16}=A_{26}=0. (11)

This approach of using each fiber orientation angle directly as a design variable is straightforward, and the number of design variables stays within the applicable range of permutation, namely, all the combinations can be calculated so that direct comparison is possible without using some approximate optimum design methods, such as mathematical programming or heuristic methods, e.g. genetic algorithm (GA) or particle swarm optimization (PSO).

2.3 Outline of vibration analysis

A previous solution is used here as in [20,21] based on the method of Ritz within the classical thin plate theory. This analysis-based solution has a low computational cost and easiness in varying combination in boundary conditions, in contrast to numerical methods such as the finite element method. Figure 2 shows geometry of rectangular plate and the coordinate system, and the dimension of the plate is given by a×b×h (thickness).

The relation between stress and strain is given in Eq.(1). When this equation is integrated over the thickness after multiplying a thickness coordinate z, one gets moment resultant

$$\begin{Bmatrix} M_x \\ M_y \\ M_{xy} \end{Bmatrix} = \begin{bmatrix} D_{11} & D_{12} & D_{16} \\ D_{12} & D_{22} & D_{26} \\ D_{16} & D_{26} & D_{66} \end{bmatrix} \{\kappa\} \tag{12}$$

where the D_{ij} are the bending stiffnesses (5) and $\{\kappa\}$ is a curvature vector given in (15).

When one considers the small amplitude (linear) free vibration of a plate, the deflection w may be written by

$$w(x,y,t) = W(x,y)\sin\omega t \tag{13}$$

where W is the amplitude and ω is a radian frequency of the plate. Then, the maximum strain energy due to the bending is expressed by

$$U_{\max} = \frac{1}{2}\iint_A \{\kappa\}^T \begin{bmatrix} D_{11} & D_{12} & D_{16} \\ D_{12} & D_{22} & D_{26} \\ D_{16} & D_{26} & D_{66} \end{bmatrix} \{\kappa\}\, dA \tag{14}$$

where $\{\kappa\}$ is a curvature vector

$$\{\kappa\} = \left\{ -\frac{\partial^2 W}{\partial x^2} \quad -\frac{\partial^2 W}{\partial y^2} \quad -2\frac{\partial^2 W}{\partial x \partial y} \right\}^T \tag{15}$$

The maximum kinetic energy is given by

$$T_{\max} = \frac{1}{2}\rho h \omega^2 \iint_A W^2 dA \tag{16}$$

where ρ [kg/m^3] is the mass per unit volume.

For the sake of simplicity, non-dimensional quantities are introduced as

$$\xi = \frac{2x}{a}, \eta = \frac{2y}{b} \text{ (non-dimensional coordinates)},$$

$$\alpha = \frac{a}{b} \text{ (aspect ratio)},$$

$$D_0 = \frac{E_T h^3}{12(1-\nu_{LT}\nu_{TL})} \text{ (reference stiffness)} \tag{17}$$

$$\Omega = \omega a^2 \sqrt{\frac{\rho h}{D_0}} \text{ (frequency parameter)}$$

It should be remembered here that regardless of the number of layers, the frequency parameter is normalized with respect to the total thickness h. Namely, a twelve-layer plate has the same total thickness as a six-layer plate in this parameter Ω.

The next step in the Ritz method is to assume that the amplitude as

$$W(\xi,\eta) = \sum_{m=0}^{M-1}\sum_{n=0}^{N-1} A_{mn} X_m(\xi) Y_n(\eta) \tag{18}$$

where A_{mn} are unknown coefficients, and $X_m(\xi)$, $Y_n(\eta)$ are the functions modified later so that any kinematical boundary conditions are satisfied at the edges.

After substituting Eq.(18) into the energies (14) and (16), the stationary value is obtained by

$$\frac{\partial}{\partial A_{\bar{m}\bar{n}}}(T_{\max} - U_{\max}) = 0 \quad (\bar{m} = 0,1,2,..;\bar{n} = 0,1,2,...) \tag{19}$$

Then the eigenvalue equation that contains the frequency parameter Ω is derived as

$$\sum_{m=0}^{M-1}\sum_{n=0}^{N-1}\left[\left(\frac{D_{11}}{D_0}\right)I^{(2200)}+\alpha^2\left(\frac{D_{12}}{D_0}\right)(I^{(2002)}+I^{(0220)})+\alpha^4\left(\frac{D_{22}}{D_0}\right)I^{(0022)}+4\alpha^2\left(\frac{D_{66}}{D_0}\right)I^{(1111)}-\Omega^2 I^{(0000)}\right]_{\bar{m}\bar{m}\bar{n}\bar{n}}\cdot A_{mn}=0$$

$$(\bar{m}=0,1,2,..;\bar{n}=0,1,2,...) \tag{20}$$

where an integral I is the products

$$I^{(\bar{p}\bar{q}\bar{r}\bar{s})}_{mmnn}=\phi^{(\bar{p}\bar{q})}_{mm}\cdot\phi^{(\bar{r}\bar{s})}_{nn} \tag{21}$$

of the two integrals defined by

$$\phi^{(\bar{p}\bar{q})}_{mm}=\int_{-1}^{1}\frac{\partial^{(p)}X_m}{\partial\xi^{(p)}}\frac{\partial^{(q)}X_{\bar{m}}}{\partial\xi^{(q)}}d\xi \tag{22}$$

Equation (20) is a set of linear simultaneous equations in terms of the coefficients A_{mn}, and the eigenvalues Ω may be extracted by using existing eigenvalue subroutines.

The analytical procedure developed this far is a standard routine of the Ritz method, and modification is explained next so as to incorporate arbitrary edge conditions into the amplitude $W(\xi,\eta)$. In the traditional approach, for example, using the beam functions for $X_m(\xi)$ and $Y_n(\eta)$, many different products of regular and hyper trigonometric functions exist for arbitrary conditions and it is difficult to make a unified subroutine to calculate all of the various kinds of integrals.

The present approach introduces a kind of polynomial

$$X_m(\xi)=\xi^m(\xi+1)^{B1}(\xi-1)^{B3}$$
$$Y_n(\eta)=\eta^n(\eta+1)^{B2}(\eta-1)^{B4} \tag{23}$$

where B_1, B_2, B_3 and B_4 are "boundary indices" [20,21] which are added to satisfy the kinematical boundary conditions and are used in such a way as B_i=0 for F (free edge), 1 for S (simply supported edge) and 2 for C (clamped edge). To the C-S-F-F plate, for instance, B_1=2, B_2=1 and B_3=B_4=0 are applied. With the boundary indices B_i's and Eqs.(23), the method of Ritz can accommodate arbitrary sets of the edge conditions, and the integrals (22) can be exactly evaluated.

Table 1. Convergence and comparison of frequency parameters $\Omega=\omega a^2(\rho h/D)^{1/2}$ for quasi-isotropic square plates with eight symmetric layers [0°/45°/90°/-45°]s

	Ω_1	Ω_2	Ω_3	Ω_4	Ω_5
CFFF plate					
6×6	11.091	19.229	51.920	69.812	83.420
8×8	11.088	19.225	51.435	69.784	83.321
10×10	11.087	19.223	51.432	69.780	83.314
FEM [11]	11.095	19.217	51.419	69.803	83.321
dif.(%)	0.07	-0.03	-0.03	0.03	0.01
CSFF plate					
6×6	13.929	39.070	75.022	91.093	114.46
8×8	13.928	39.064	75.008	90.686	113.67
10×10	13.928	39.063	75.006	90.681	113.66
FEM [11]	13.928	39.050	74.990	90.573	113.53
dif.(%)	0	-0.03	-0.02	-0.12	-0.11
SSSS plate					
6×6	46.075	97.548	139.96	175.06	201.26
8×8	46.070	97.537	139.94	174.32	199.04
10×10	46.068	97.533	139.94	174.31	198.99
FEM [11]	46.005	97.292	139.66	173.42	198.28
dif.(%)	-0.14	-0.25	-0.20	-0.51	-0.36
CCCC plate					
6×6	90.050	151.32	212.95	245.80	274.60
8×8	90.050	151.32	212.95	245.62	274.36
10×10	90.050	151.32	212.95	245.61	274.35
FEM [11]	89.817	150.65	212.34	244.00	272.61
dif.(%)	-0.26	-0.44	-0.29	-0.66	-0.63

3. Numerical examples and accuracy of the solution

3.1 Numerical examples

Symmetrically laminated plates with six, eight, ten and twelve layers are given for numerical examples. A six-layer plate has three design variables $\theta_1,\theta_2,\theta_3$, but due to the restriction of quasi-isotropy in Eq.(6), a number of combination of layers is given by 36×2×1=72 for $\Delta\theta_1=5°$ of six-layer plates. So, seventy-two times of frequency calculation are repeated to find the maximum and minimum ones. Similarly, the numbers of combination of layers are 36×3×2×1=216, 36×4×3×2×1=864 and 36×5×4×3×2×1=4320 for eight-layer, ten-layer and twelve-layer plates, respectively, with $\Delta\theta_1=5°$. In other words, a twelve-layer plate needs computation of sixty (=4320/72) times more than a six-layer plate. A short effective computation time of the present Ritz method is fully made use particularly for 12-layer plate. For $\Delta\theta_1=15°$, the number of combinations reduces to 24, 72, 288 and 1440 for six-layer, eight-layer, ten-layer and twelve-layer plates, respectively.

The material constants in Eq.(4) are used in the examples. It should be noted again that the frequency parameter Ω is normalized by the total thickness h (i.e. the total thickness of the plates with different number of layers is regarded as the same) in the definition, when one compares effects of fiber orientation angles among plates with different number of layers.

3.2 Convergence and comparison of the solution

Table 1 presents convergence study of the lowest five frequency parameters $\Omega_1 \sim \Omega_5$ with increase of series terms in Eq.(18). Since the amplitude function satisfies kinematical boundary conditions exactly, this Ritz method yields upper-bound solutions, and tends to converge from above. Four sets of boundary conditions are assumed as CFFF (cantilever), CSFF, SSSS and CCCC plates. Each of these four letters correspond in this order to Edge(1), Edge(2), Edge(3) and Edge(4), respectively, in Fig.2. In the table, the lower frequency parameters are converged in values rounded to four significant figures, and even higher frequencies converge well. Based on this test, following results will be obtained by using 10×10 terms.

Table 2. Frequency parameters Ω_1 and lay-up designs of quasi-isotropic square plates (CFFF)($\Delta\theta_1$= 5°).

6-layer plate			8-layer plate		
Order	Ω_1	$[\theta_1/\theta_2/\theta_3]$s	Order	Ω_1	$[\theta_1/\theta_2/\theta_3/\theta_4]$s
1	11.689	[0/ 60/ −60]	1	11.390	[5/ −40/ 50/ −85]
2	(ditto)	[0/ −60/ 60]	2	(ditto)	[−5/ 40/ −50/ 85]
3	11.649	[5/ −55/ 65]	3	11.366	[−10/ 35/ −55/ 80]
4	(ditto)	[−5/ 55/ −65]	4	(ditto)	[10/ −35/ 55/ −80]
5	11.432	[5/ 65/ −55]	5	11.332	[−10/ 35/ 80/ −55]
6	(ditto)	[−5/ −65/ 55]	6	(ditto)	[10/ −35/ −80/ 55]
⋮			⋮		
69	5.098	[70/ −50/ 10]	213	5.335	[−80/ 55/ −35/ 10]
70	(ditto)	[−70/ 50/ −10]	214	(ditto)	[80/ −55/ 35/ −10]
71	5.070	[−65/ 55/ −5]	215	5.326	[−75/ 60/ −30/ 15]
72	(ditto)	[65/ −55/ 5]	216	(ditto)	[75/ −60/ 30/ −15]

10-layer plate			12-layer plate		
Order	Ω_1	$[\theta_1/\theta_2/\theta_3/\theta_4/\theta_5]$s	Order	Ω_1	$[\theta_1/\theta_2/\theta_3/\theta_4/\theta_5/\theta_6]$s
1	11.390	[5/ −31/ 41/ 77/ −67]	1	11.407	[5/−25/ 35/−55/−85/ 65]
2	(ditto)	[−5/ 31/ −41/ −77/ 67]	2	(ditto)	[−5/ 25/−35/ 55/ 85/−65]
3	11.388	[−5/ 31/ −41/ 67/ −77]	3	11.402	[5/−25/ 35/−55/ 65/−85]
4	(ditto)	[5/ −31/ 41/ −67/ 77]	4	(ditto)	[−5/ 25/−35/ 55/−65/ 85]
5	11.375	[−10/ 26/ −46/ 62/ −82]	5	11.389	[−5/ 25/−35/ 85/ 55/−65]
6	(ditto)	[10/ −26/ 46/ −62/ 82]	6	(ditto)	[5/−25/ 35/−85/−55/ 65]
⋮			⋮		
861	5.326	[85/ −59/ 49/ −23/ 13]	4317	5.288	[−80/ 70/−50/ 40/−20/ 10]
862	(ditto)	[−85/ 59/ −49/ 23/ −13]	4318	(ditto)	[80/−70/ 50/−40/ 20/−10]
863	5.297	[80/ −64/ 44/ −28/ 8]	4319	5.288	[85/−65/ 55/−35/ 25/ −5]
864	(ditto)	[−80/ 64/ −44/ 28/ −8]	4320	(ditto)	[−85/ 65/−55/ 35/−25/ 5]

Table 3. Frequency parameters Ω_1 and lay-up designs of quasi-isotropic square plates (CSFF)($\Delta\theta_1$= 5°).

6-layer plate			8-layer plate		
Order	Ω_1	$[\theta_1/\theta_2/\theta_3]$s	Order	Ω_1	$[\theta_1/\theta_2/\theta_3/\theta_4]$s
1	15.769	[20/ −40/ 80]	1	15.420	[25/ −20/ −65/ 70]
2	15.650	[15/ −45/ 75]	2	15.369	[20/ −25/ −70/ 65]
3	15.642	[25/ −35/ 85]	3	15.355	[30/ −60/ −15/ 75]
4	15.279	[30/ −30/ 90]	4	15.280	[30/ −15/ −60/ 75]
5	15.275	[10/ −50/ 70]	5	15.268	[35/ −55/ −10/ 80]
6	14.695	[35/ −25/ −85]	6	15.241	[25/ −65/ −20/ 70]
⋮			⋮		
69	9.155	[85/ −35/ 25]	213	10.121	[80/ −55/ −10/ 35]
70	9.061	[−80/ −20/ 40]	214	9.947	[−85/ −40/ 5/ 50]
71	8.939	[90/ −30/ 30]	215	9.946	[85/ −50/ −5/ 40]
72	8.902	[−85/ −25/ 35]	216	9.881	[90/ −45/ 0/ 45]

10-layer plate			12-layer plate		
Order	Ω_1	$[\theta_1/\theta_2/\theta_3/\theta_4/\theta_5]$s	Order	Ω_1	$[\theta_1/\theta_2/\theta_3/\theta_4/\theta_5/\theta_6]$s
1	15.467	[25/ −47/ −11/ 61/ −83]	1	15.300	[25/−35/ −5/−65/ 55/ 85]
2	15.431	[30/ −42/ −6/ −78/ 66]	2	15.296	[30/ 0/−60/−30/ 60/ 90]
3	15.397	[25/ −47/ −11/ −83/ 61]	3	15.294	[15/−45/ 45/−15/−75/ 75]
4	15.362	[20/ −52/ −16/ 56/ −88]	4	15.279	[20/−40/−10/ 50/−70/ 80]
5	15.361	[30/ −42/ −6/ 66/ −78]	5	15.279	[25/ −5/−35/−65/ 55/ 85]
6	15.296	[25/ −11/ −47/ −83/ 61]	6	15.276	[30/−30/ 0/−60/ 60/ 90]
⋮			⋮		
861	10.176	[85/ −59/ −23/ 13/ 49]	4317	10.246	[−80/−50/−20/ 70/ 10/ 40]
862	10.147	[90/ −18/ −54/ 54/ 18]	4318	10.203	[−85/−55/−25/ 65/ 5/ 35]
863	10.085	[90/ −54/ −18/ 54/ 18]	4319	10.170	[85/−65/−35/ −5/ 55/ 25]
864	10.078	[−85/ −49/ −13/ 59/ 23]	4320	10.168	[90/−60/−30/ 0/ 60/ 30]

Table 4. Frequency parameters Ω_1 and lay-up designs of simply supported quasi-isotropic square plates (SSSS) ($\Delta\theta_1$= 5°).

6-layer plate			8-layer plate		
Order	Ω_1	$[\theta_1/\theta_2/\theta_3]$s	Order	Ω_1	$[\theta_1/\theta_2/\theta_3/\theta_4]$s
1	51.041	[35/ -25/ -85]	1	53.629	[-45/ 45/ 0/ 90]
2	(ditto)	[-35/ 25/ 85]	2	(ditto)	[-45/ 45/ 90/ 0]
3	(ditto)	[-55/ 65/ 5]	3	(ditto)	[45/ -45/ 90/ 0]
4	(ditto)	[55/ -65/ -5]	4	(ditto)	[45/ -45/ 0/ 90]
5	51.006	[-30/ 30/ 90]	5	53.441	[50/ -40/ -85/ 5]
6	(ditto)	[30/ -30/ 90]	6	(ditto)	[-40/ 50/ 5/ -85]
・			・		
69	43.961	[-75/ -15/ 45]	213	44.307	[0/ 90/ -45/ 45]
70	(ditto)	[15/ 75/ -45]	214	(ditto)	[0/ 90/ 45/ -45]
71	(ditto)	[75/ 15/ -45]	215	(ditto)	[90/ 0/ 45/ -45]
72	(ditto)	[-15/ -75/ 45]	216	(ditto)	[90/ 0/ -45/ 45]
10-layer plate			**12-layer plate**		
Order	Ω_1	$[\theta_1/\theta_2/\theta_3/\theta_4/\theta_5]$s	Order	Ω_1	$[\theta_1/\theta_2/\theta_3/\theta_4/\theta_5/\theta_6]$s
1	53.247	[-50/ 58/ 22/ -14/ -86]	1	53.316	[40/-50/-20/ 70/-80/ 10]
2	(ditto)	[40/ -32/ -68/ 76/ 4]	2	(ditto)	[-50/ 40/ 70/-20/ 10/-80]
3	(ditto)	[-40/ 32/ 68/ -76/ -4]	3	(ditto)	[50/-40/-70/ 20/-10/ 80]
4	(ditto)	[50/ -58/ -22/ 14/ 86]	4	(ditto)	[-40/ 50/ 20/-70/ 80/-10]
5	53.165	[-50/ 58/ 22/ -86/ -14]	5	53.286	[-40/ 50/ 20/-70/-10/ 80]
6	(ditto)	[50/ -58/ -22/ 86/ 14]	6	(ditto)	[-50/ 40/ 70/-20/-80/ 10]
・			・		
861	44.947	[10/ 82/ 46/ -26/ -62]	4317	45.274	[85/ -5/ 25/ 55/-65/-35]
862	(ditto)	[-10/ -82/ -46/ 26/ 62]	4318	(ditto)	[-85/ 5/-25/-55/ 65/ 35]
863	(ditto)	[80/ 8/ 44/ -64/ -28]	4319	(ditto)	[5/-85/ 65/ 35/-25 -55]
864	(ditto)	[-80/ -8/ -44/ 64/ 28]	4320	(ditto)	[-5/ 85/-65/-35/ 25/ 55]

Table 5. Frequency parameters Ω_1 and lay-up design of clamped quasi-isotropic square plates (CCCC)($\Delta\theta_1$= 5°).

6-layer plate			8-layer plate		
Order	Ω1	$[\theta_1/\theta_2/\theta_3]$s	Order	Ω1	$[\theta_1/\theta_2/\theta_3/\theta_4]$s
1	90.923	[85/ -35/ 25]	1	91.320	[-85/ 5/ 50/ -40]
2	(ditto)	[-85/ 35/ -25]	2	(ditto)	[5/ -85/ -40/ 50]
3	(ditto)	[-5/ 55/ -65]	3	(ditto)	[85/ -5/ -50/ 40]
4	(ditto)	[5/ -55/ 65]	4	(ditto)	[-5/ 85/ 40/ -50]
5	90.806	[10/ -50/ 70]	5	91.287	[90/ 0/ -45/ 45]
6	(ditto)	[-10/ 50/ -70]	6	(ditto)	[90/ 0/ 45/ -45]
・			・		
69	86.247	[-40/ 80/ 20]	213	86.3075	[55/ 10/ -80/ -35]
70	(ditto)	[40/ -80/ -20]	214	(ditto)	[-55/ -10/ 80/ 35]
71	(ditto)	[-50/ 10/ 70]	215	(ditto)	[35/ 80/ -10/ -55]
72	(ditto)	[50/ -10/ -70]	216	(ditto)	[-35/ -80/ 10/ 55]
10-layer plate			**12-layer plate**		
Order	Ω1	$[\theta_1/\theta_2/\theta_3/\theta_4/\theta_5]$s	Order	Ω1	$[\theta_1/\theta_2/\theta_3/\theta_4/\theta_5/\theta_6]$s
1	91.186	[0/ 72/ -72/ -36/ 36]	1	91.216	[85/ -5/-65/ 25/ 55/-35]
2	(ditto)	[90/ -18/ 18/ 54/ -54]	2	(ditto)	[5/-85/-25/ 65/ 35/-55]
3	(ditto)	[0/ -72/ 72/ 36/ -36]	3	(ditto)	[-85/ 5/ 65/-25/-55/ 35]
4	(ditto)	[90/ 18/ -18/ -54/ 54]	4	(ditto)	[-5/ 85/ 25/-65/-35/ 55]
5	91.182	[-85/ -13/ 23/ 59/ -49]	5	91.178	[-85/ 5/ 65/-55/-25/ 35]
6	(ditto)	[5/ 77/ -67/ -31/ 41]	6	(ditto)	[5/-85/-25/ 35/ 65/-55]
・			・		
861	86.252	[55/ 19/ -89/ -17/ -53]	4317	86.198	[50/ 20/ 80/-10/-70/-40]
862	(ditto)	[-55/ -19/ 89/ 17/ 53]	4318	(ditto)	[-50/-20/-80/ 10/ 70/ 40]
863	(ditto)	[35/ 71/ -1/ -73/ -37]	4319	(ditto)	[40/ 70/ 10/-80/-20/-50]
864	(ditto)	[-35/ -71/ 1/ 73/ 37]	4320	(ditto)	[-40/-70/-10/ 80/ 20/ 50]

Accuracy of this method is verified also by comparison with the frequency parameters of quasi-isotropic square plates obtained by the finite element program used in ref.[11]. The square plate is divided by 20×20=400 elements, and good agreement is found with the Ritz method. Differences caused by the FEM (20×20 elements) and present Ritz (10×10 terms) methods are evaluated by

$$\text{Difference}(\%) = (\text{FEM} - \text{Ritz}) / (\text{Ritz}) \times 100 \qquad (24)$$

and included in the table. As seen, the differences are very small and accuracy of the methods is well established.

3.3 Numerical results

Tables 2,3,4 and 5 present top six frequency parameters Ω_1 of the highest (maximum) values and four of the lowest (minimum) values for CFFF (cantilever), CSFF, SSSS and CCCC plates, respectively. Aspect ratio is taken a/b=1 (square plate). In each table, results are summarized for symmetrically laminated six-layer, eight-layer, ten-layer and twelve-layer plates. In these tables and hereafter, a symbol of angle '°' is omitted in the tables. Stacking sequence in all these examples is examined to satisfy the quasi-isotropic condition.

In Table 2, a six-layer plate (with minimum number of design variables) gives the highest frequency Ω_1=11.689 among four those of different layer numbers, and a twelve-layer plate has the second highest frequency of Ω_1=11.407. It is interesting to see that eight-layer and ten-layer plates share the identical highest frequency Ω_1=11.390. In other words, restriction of the quasi-isotropic condition imposes laminated plates to have complicated optimizing effect, regardless of general tendency that larger number of design variables generally gives more optimized (higher in this case) values. Similarly, for the minimum frequencies, the lowest frequencies are found in the order of plates with six, twelve, ten and eight layers, not simply following the order of the number of layers.

A CFFF (cantilever) square plate in Table 2 has one symmetry axis (about the boundary conditions) that is perpendicular to the clamped edge (Edge(1) in Fig.2), and frequencies are always obtained as pairs of identical frequency values. However, for a CSFF plate with no symmetry with respect to the boundary condition in Table 3, all the frequencies appear as each being independent value. The maximum values are in the decreasing order of Ω_1=15.769, 15.467, 15.420 and 15.300 of plates with six, ten, eight and twelve layers, respectively.

Next, SSSS plate in Table 4 and CCCC plate in Table 5 are uniformly constrained along the edges, and there are two symmetry axes with respect to boundary condition. So, frequencies are given with a set of four identical values due to the two symmetrical axes. Among the maximum frequencies with different number of layers for SSSS plates in Table 4, the maximum values are in the order of Ω_1=53.629, 53.316, 53.247 and 51.041 of plates with eight, twelve, ten and six layers. Unlike plates with free edges in Tables 2 and 3, a six-layer plate does not give the highest value among the four different layer plates. For a CCCC

Table 6. Frequency parameters Ω1 and lay-up designs of quasi-isotropic 8-layer square plates by using $\Delta\theta_1$= 15°

CFFF plate			CSFF plate		
Order	Ω_1	[θ_1/θ_2/θ_3/θ_4]s	Order	Ω_1	[θ_1/θ_2/θ_3/θ_4]s
1	11.291	[0/ 45/ −45/ 90]	1	15.355	[30/ −60/ −15/ 75]
2	(ditto)	[0/ −45/ 45/ 90]	2	15.280	[30/ −15/ −60/ 75]
3	11.229	[15/ −30/ 60/ −75]	3	15.123	[15/ −30/ −75/ 60]
4	(ditto)	[−15/ 30/ −60/ 75]	4	15.099	[15/ −30/ 60/ −75]
5	11.212	[15/ −30/ −75/ 60]	5	14.755	[30/ −60/ 75/ −15]
6	(ditto)	[−15/ 30/ 75/ −60]	6	14.546	[0/ 45/ −45/ 90]
▪			▪		
69	5.512	[60/ −75/ −30/ 15]	69	10.385	[75/ −60/ −15/ 30]
70	(ditto)	[−60/ 75/ 30/ −15]	70	10.324	[−75/ −30/ 60/ 15]
71	5.326	[75/ −60/ 30/ −15]	71	10.287	[75/ −15/ −60/ 30]
72	(ditto)	[−75/ 60/ −30/ 15]	72	9.881	[90/ −45/ 0/ 45]
SSSS plate			**CCCC plate**		
Order	Ω_1	[θ_1/θ_2/θ_3/θ_4]s	Order	Ω_1	[θ_1/θ_2/θ_3/θ_4]s
1	53.629	[45/ −45/ 90/ 0]	1	91.287	[0/ 90/ −45/ 45]
2	(ditto)	[45/ −45/ 0/ 90]	2	(ditto)	[0/ 90/ 45/ −45]
3	(ditto)	[−45/ 45/ 0/ 90]	3	(ditto)	[90/ 0/ −45/ 45]
4	(ditto)	[−45/ 45/ 90/ 0]	4	(ditto)	[90/ 0/ 45/ −45]
5	51.508	[60/ −30/ −75/ 15]	5	90.915	[15/ −75/ −30/ 60]
6	(ditto)	[−30/ 60/ 15/ −75]	6	(ditto)	[−15/ 75/ 30/ −60]
▪			▪		
69	44.307	[0/ 90/ 45/ −45]	69	86.513	[30/ 75/ −15/ −60]
70	(ditto)	[0/ 90/ −45/ 45]	70	(ditto)	[−30/ −75/ 15/ 60]
71	(ditto)	[90/ 0/ 45/ −45]	71	(ditto)	[60/ 15/ −75/ −30]
72	(ditto)	[90/ 0/ −45/ 45]	72	(ditto)	[−60/ −15/ 75/ 30]

Table 7. Maximum and minimum frequency parameters Ω_1 and their ratios of 8-layered square plates ($\Delta\theta_1$=5°)

Class	BC	$\Omega_{1,max}$	$[\theta_1/\theta_2/\theta_3/\theta_4]_S$	$\Omega_{1,min}$	max/min
1	FFFF	32.632	[45/-45/0/90]	21.951	1.49
2	SFFF	19.842	[45/-45/0/90]	10.818	1.83
	FSFF	(ditto)	[-45/45/90/0]	(ditto)	
	FFSF	(ditto)	[45/-45/0/90]	(ditto)	
	FFFS	(ditto)	[-45/45/90/0]	(ditto)	
3	FSSF	10.567	[45/-45/90/0]	5.402	1.96
	FFSS	(ditto)	[-45/45/90/0]	(ditto)	
	SFFS	(ditto)	[45/-45/90/0]	(ditto)	
	SSFF	(ditto)	[-45/45/90/0]	(ditto)	
4	CFFF	11.390	[5/-40/50/-85]	5.326	2.14
	FFCF	(ditto)	[5/-40/50/-85]	(ditto)	
	FCFF	(ditto)	[85/-50/40/-5]	(ditto)	
	FFFC	(ditto)	[85/-50/40/-5]	(ditto)	
5	FFCS	15.420	[25/-20/-65/70]	9.881	1.56
	FSCF	(ditto)	[-25/20/65/-70]	(ditto)	
	CSFF	(ditto)	[25/-20/-65/70]	(ditto)	
	CFFS	(ditto)	[-25/20/65/-70]	(ditto)	
	FFSC	(ditto)	[65/-70/-25/20]	(ditto)	
	FCSF	(ditto)	[-65/70/25/-20]	(ditto)	
	SCFF	(ditto)	[65/-70/-25/20]	(ditto)	
	SFFC	(ditto)	[-65/70/25/-20]	(ditto)	
6	FFCC	18.381	[45/-45/90/0]	13.299	1.38
	FCCF	(ditto)	[-45/45/0/90]	(ditto)	
	CCFF	(ditto)	[45/-45/90/0]	(ditto)	
	CFFC	(ditto)	[-45/45/0/90]	(ditto)	
7	FSFS	31.645	[-85/50/-40/5]	14.669	2.16
	SFSF	(ditto)	[-5/40/-50/85]	(ditto)	
8	SFSS	35.284	[-10/35/-55/80]	21.303	1.66
	SSSF	(ditto)	[-10/35/-55/80]	(ditto)	
	FSSS	(ditto)	[-80/55/-35/10]	(ditto)	
	SSFS	(ditto)	[-80/55/-35/10]	(ditto)	
9	SFSC	36.404	[10/-35/55/-80]	25.620	1.42
	SCSF	(ditto)	[10/-35/55/-80]	(ditto)	
	FSCS	(ditto)	[80/-55/35/-10]	(ditto)	
	CSFS	(ditto)	[80/-55/35/-10]	(ditto)	
10	SFCF	49.854	[5/-40/50/-85]	23.306	2.14
	CFSF	(ditto)	[-5/40/-50/85]	(ditto)	
	FSFC	(ditto)	[-85/50/-40/5]	(ditto)	
	FCFS	(ditto)	[-85/50/-40/5]	(ditto)	
11	FSSC	52.843	[80/-55/35/-10]	28.227	1.87
	SSFC	(ditto)	[-80/55/-35/10]	(ditto)	
	SFCS	(ditto)	[10/-35/55/-80]	(ditto)	
	SSCF	(ditto)	[-10/35/-55/80]	(ditto)	
	SCFS	(ditto)	[80/-55/35/-10]	(ditto)	
	FCSS	(ditto)	[-80/55/-35/10]	(ditto)	
	CSSF	(ditto)	[10/-35/55/-80]	(ditto)	
	CFSS	(ditto)	[-10/35/-55/80]	(ditto)	
12	SSSS	53.629	[-45/45/0/90]	44.307	1.21
13	FSCC	53.669	[75/-60/30/-15]	31.454	1.71
	FCCS	(ditto)	[-75/60/-30/15]	(ditto)	
	SFCC	(ditto)	[15/-30/60/-75]	(ditto)	
	SCCF	(ditto)	[-15/30/-60/75]	(ditto)	
	CCSF	(ditto)	[15/-30/60/-75]	(ditto)	
	CFSC	(ditto)	[-15/30/-60/75]	(ditto)	
	CCFS	(ditto)	[75/-60/30/-15]	(ditto)	
	CSFC	(ditto)	[-75/60/-30/15]	(ditto)	
14	SSSC	63.588	[80/-55/35/-10]	52.398	1.21
	SCSS	(ditto)	[-80/55/-35/10]	(ditto)	
	CSSS	(ditto)	[10/-35/55/-80]	(ditto)	
	SSCS	(ditto)	[-10/35/-55/80]	(ditto)	
15	SSCC	69.660	[45/-45/90/0]	64.000	1.09
	CCSS	(ditto)	[45/-45/0/90]	(ditto)	
	SCCS	(ditto)	[-45/45/0/90]	(ditto)	
	CSSC	(ditto)	[-45/45/90/0]	(ditto)	
16	FCFC	72.699	[-85/50/-40/5]	34.163	2.13
	CFCF	(ditto)	[-5/40/-50/85]	(ditto)	
17	CFCS	74.720	[5/-40/50/-85]	38.348	1.95
	CSCF	(ditto)	[5/-40/50/-85]	(ditto)	
	FCSC	(ditto)	[-85/50/-40/5]	(ditto)	
	SCFC	(ditto)	[-85/50/-40/5]	(ditto)	
18	CFCC	75.290	[5/-40/50/-85]	41.123	1.83
	CCCF	(ditto)	[5/-40/50/-85]	(ditto)	
	FCCC	(ditto)	[85/-50/40/-5]	(ditto)	
	CCFC	(ditto)	[85/-50/40/-5]	(ditto)	
19	SCSC	83.359	[80/-55/35/-10]	59.843	1.39
	CSCS	(ditto)	[10/-35/55/-80]	(ditto)	
20	CSCC	86.374	[10/-35/55/-80]	72.631	1.19
	CCCS	(ditto)	[10/-35/55/-80]	(ditto)	
	CCSC	(ditto)	[80/-55/35/-10]	(ditto)	
	SCCC	(ditto)	[-80/55/-35/10]	(ditto)	
21	CCCC	91.320	[5/-85/-40/50]	86.308	1.06

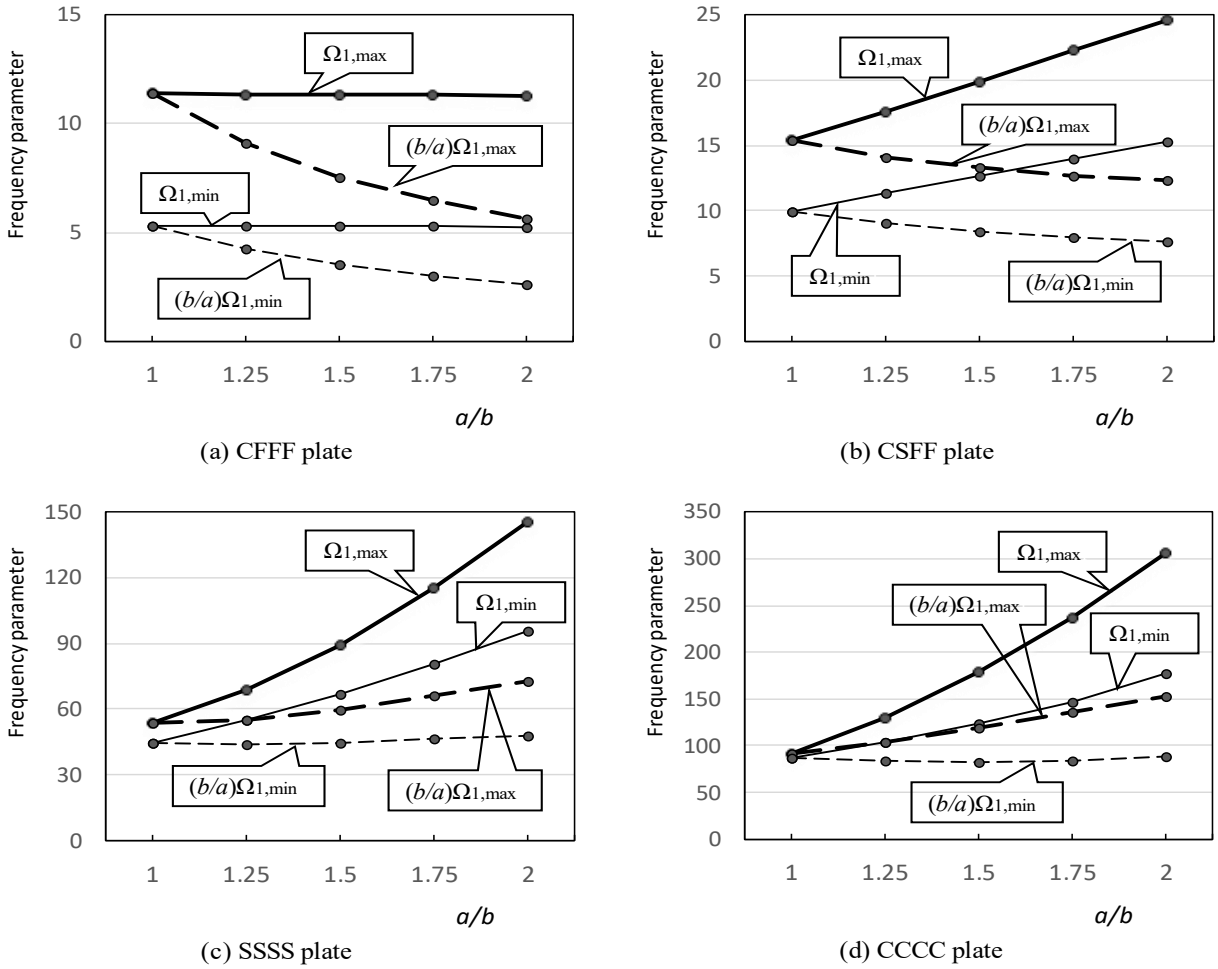

Figure 3. Effect of aspect ratio *a/b* on the maximum and minimum frequencies of quasi-isotropic rectangular plates

plate in Table 5, similarly for a SSSS plate in Table 4, the maximum values are given in the order of eight, twelve, ten and six layers. It is also found that the maximum and minimum frequencies are all close each other due to stronger constraints (i.e., all boundaries clamped) from the edges rather than the constraint from the layer sequence. As mentioned above, the computation time depends on increment $\Delta\theta_1$, and $\Delta\theta_1$=5° was used in Tables 2-5.

Next in Table 6, one sees the effect of using a coarse mesh of $\Delta\theta_1$=15°. This use of the mesh reduces computation time to one third (216 times computation to 72 times) for the eight-layer plate. The table presents top six frequency parameters Ω_1 of the highest values and four of the lowest values for CFFF (cantilever), CSFF, SSSS and CCCC square plates (*a/b*=1). When one compares the maximum frequency $\Omega_{1,max}$, for CFFF plate, it is 11.291/11.390=99.1% of the result with $\Delta\theta_1$=5°. Similarly, reduction of the maximum frequencies is 99.6, 100.0 (same frequency) and 99.5% for CSFF, SSSS and CCCC, respectively. Practically speaking, the results with $\Delta\theta_1$=15° are relatively close to those with $\Delta\theta_1$=5° in these examples.

Table 7 presents $\Omega_{1,max}$, corresponding fiber orientation angles $[\theta_1/\theta_2/\theta_3/\theta_4]_s$ and $\Omega_{1,min}$ with ratios of $\Omega_{1,max}/\Omega_{1,min}$ (ratio of optimization effectiveness) for all possible eighty-one combinations (3^4=81) of *three* classical boundary conditions (F, S, C) along *four* edges of square plates. The eighty-one frequencies are grouped into twenty-one Classes to have identical frequencies. For example, Class 2 (SFFF, FSFF, FFSF, FFFS) holds the same maximum frequency $\Omega_{1,max}$=19.842 and minimum one $\Omega_{1,min}$=10.818.

Class 1 of FFFF plate has three rigid body modes, and Class 2 of SFFF, FSFF, FFSF and SSSF plates has one rigid body mode. These modes in rigid body motion (zero frequency) are not listed here, and the lowest elastic vibration modes are given in the tables. Generally speaking, on the ratio of $\Omega_{1,max}/\Omega_{1,min}$, the ratio decreases from 2.16 of Class 7 (FSFS, SFSF) to 1.06 of Class 21 (CCCC), as the clamped edge (C) is increasing and the free edge (F) is removed along four edges.

For studying effect of aspect ratio *a/b* on the frequencies, Figure 3 presents variations of the maximum frequency $\Omega_{1,max}$ and minimum frequencies $\Omega_{1,min}$ that are shown by *thick* solid line and *thin* solid line, respectively. An aspect ratio *a/b* is covered from *a/b*=1 to 2. Naturally, the thick solid curve in $\Omega_{1,max}$ is always higher than the thin solid curve in $\Omega_{1,min}$, and these curves (thick and thin lines) never cross each other. Since frequency parameter Ω is affected by the change of plate area (i.e., the plate area decreases as *a/b* increases), also shown are broken lines to exclude the effect of plate area. Thick *broken* lines indicate maximum frequency change after excluding the area effect, and the thin *broken* lines do the minimum frequency change by using a modified frequency parameter. This expression can absorb the effect of change in the plate area.

$$\left(\frac{b}{a}\right)\Omega = \omega(ab)\sqrt{\frac{\rho h}{D_0}} \tag{25}$$

In Fig.3 (a) CFFF plate, the maximum $\Omega_{1,max}$ and minimum frequencies $\Omega_{1,min}$ stay almost flat with the aspect ratio change. But after excluding the area effect, both maximum modified parameter $(b/a)\Omega_{1,max}$ and minimum one $(b/a)\Omega_{1,min}$ decrease monotonically. In (b) CSFF plate, $\Omega_{1,max}$ and $\Omega_{1,min}$ linearly increase with a/b. Instead, after removing the area effect, both curves of $(b/a)\Omega_{1,max}$ and $(b/a)\Omega_{1,min}$ become almost linearly go down. As the plate edges are more restrained in (c) SSSS and (d) CCCC plates, $\Omega_{1,max}$ and $\Omega_{1,min}$ increase like a part of quadratic curve. After removal of the area effect, $(b/a)\Omega_{1,max}$ and $(b/a)\Omega_{1,min}$ slightly increase.

4. Conclusions

A quasi-isotropic plate is defined as a laminated composite plate consisting of layers with different fiber orientation angles arranged such that the resulting in-plane stiffness is isotropic. This configuration is achievable because the extensional stiffness matrix is obtained as the linear summation of the stiffness contributions of individual layers. In contrast, the bending stiffness components of a quasi-isotropic laminate are generally not isotropic, since they are proportional to the cubic power of the thickness coordinate, which introduces directional dependence in bending behavior. The present paper noticed this effect and used for optimization.

Quasi-isotropic laminate is widely used in aeronautical structures and related fields. Structural panels in aircraft and spacecraft frequently often employ quasi-isotropic laminates, because they must endure severe multi-directional dynamic conditions during take-off and launch. It is hoped that the idea of present paper will be used in such design situations.

References

[1] Jones RM, Mechanics of Composite Materials, CRC Press, (1998).

[2] Vinson JR, Sierakowski RL, The Behavior of Structures Composed of Composite Materials, Kluwer Academic Pub., (2002).

[3] Phiri R, Rangappa SM, Siengchin S, Oladijo OP, Ozbakkaloglu T, Advances in lightweight composite structures and manufacturing technologies: A comprehensive review, Heliyon, 10 (2024).

[4] Gurdal Z, Haftka RT, Hajela P, 1999, Design and Optimization of Laminated Composite Materials, Wiley-Interscience.

[5] Ghiasi H, Pasini D, Lessard DL, Optimum stacking sequence design of composite materials Part I: Constant stiffness design, Composite Structures 90 (2009), pp.1–11.

[6] Ghiasi H, Fayazbakhsh K, Lessard DL, Optimum stacking sequence design of composite materials Part II: Variable stiffness design, Composite Structures, 93 (2010), pp.1-13.

[7] Bert CW, Optimal design of a composite-material plate to maximize its fundamental frequency, Journal of Sound and Vibration, 50 (1977), pp.229-237.

[8] Fukunaga H, Sekine H, Sato M, Optimal design of symmetrically laminated plates for the fundamental frequency, J. Sound and Vibration, 171, (1994), pp.219-229.

[9] Narita Y, Layerwise optimization for the maximum fundamental frequency of laminated composite plates, Journal of Sound and Vibration, 263, (2003), pp.1005-1016.

[10] Narita Y, Hodgkinson JM, Layerwise optimization for maximising the fundamental frequencies of point-supported rectangular laminated composite plates, Composite Structures, 69 (2005), pp.127-135.

[11] Narita Y, Maximum frequency design of laminated plates with mixed boundary conditions, International Journal of Solids and Structures, 43, (2006), pp.4342-4356.

[12] Honda S, Narita Y, Sasaki K, Discrete optimization for vibration design of composite plates by using lamination parameters, Advanced Composite Materials 18 (2009), pp.297-314.

[13] Fukunaga H, On isotropic laminate configurations, Journal of Composite Materials, 24, (1990), pp.519-535.

[14] Paradies R, Designing quasi-isotropic laminates with respect to bending, Composites Science and Technology, 56, (1996), pp.461-472.

[15] Akkerman R, On the properties of quasi-isotropic laminates, Composites Part B, 33, (2002), pp.133-140.

[16] Douglas L, Otterloo V, Dayal V, How isotropic are quasi-isotropic laminates, Composites Part.A, 34 (2003), pp.93-103.

[17] Vannucci P, Verchery G, A new method for generating fully isotropic laminates, Composite Structures, 58 (2002), pp.75-82.

[18] Altunsaray E, Bayer I, Deflection and free vibration of symmetrically laminated quasi-isotropic thin rectangular plates for different boundary conditions, Ocean Engineering, 57 (2013), pp.197-222.

[19] Narita Y, Innami M, Narita D, The effect of using different elastic moduli on vibration of laminated CFRP rectangular plates, EPI Int. J. Engng, 2 (2019). pp.19-27. DOI: 10.25042/epi-ije.022019.05

[20] Narita Y, Combinations for the free-vibration behaviors of anisotropic rectangular plates under general edge conditions, Trans. ASME, J. Appl. Mech., 67 (2000), pp.568-573.

[21] Narita Y, Natural frequencies of isotropic rectangular plates in improved accuracy, EPI Int. J. Eng, 5 (2022), pp. 26-36. DOI: 10.25042/epi-ije.022022.05.

EPI International Journal of Engineering
Volume 8, Number 1, February 2025, pp. 45-49
DOI: 10.25042/epi-ije.022025.06

*p*ISSN 2615-5109
*e*ISSN 2621-0541

Inventory Model Simulation to Reduce Bullwhip

Mujaddid[a,*], Sapta Asmal[b], Saiful Mangngenre[c]

[a]Department of Industrial Engineering, Faculty of Engineering, Hasanuddin University. Email: adit.mullen@gmail.com
[b]Department of Industrial Engineering, Faculty of Engineering, Hasanuddin University. Email: saptaasmal@unhas.ac.id
[c]Department of Industrial Engineering, Faculty of Engineering, Hasanuddin University. Email: saiful.ti@unhas.ac.id

Abstract

One of the issues that frequently arise in the supply chain is the bullwhip effect. The bullwhip effect is simply the presence of a distant intersection of supply and demand. To address this issue, inventory management must be implemented in order to provide products or services at the appropriate time and location. The goal of this study is to reduce the occurrence of the bullwhip effect, increase service level, and consider total cost and profit. The method used is the RQ policy. RQ policy is a fixed replenishment point inventory policy / fixed replenishment quantity policy referred to as an RQ policy. When the inventory level drops below the fixed replenishment point (R), the product's fixed replenishment quantity (Q) is ordered, which is simulated in anylogistix software to determine the optimal inventory policy and design. The optimal simulation results are R:15,000 and Q: 30,000 with an inventory capacity of 30,000, a bullwhip effect value of 1.62 to 1, indicating no bullwhip effect, and a service level of 0.90 to 1, indicating that all orders can be fulfilled. with the right timing and profits ranging from Rp. 74.400.000 to Rp. 101,450,000.

Keywords: Bullwhip effect; inventory; service level; model simulation; supply chain management

1. Introduction

Inventory control policies have been identified as a factor contributing to the bullwhip effect and inventory insecurity [1]. The bullwhip effect occurs when the variation in demand for suppliers is greater than the variation in sales. P&G was the first to coin the phrase "bullwhip effect" about the demand for baby diapers [2], which results in excess or shortage of stock, loss of income, lower levels of customer satisfaction, ineffective delivery, and production scheduling errors [3], [4]. Several factors that can cause the bullwhip effect include demand force updates, order batching, price fluctuations, and rotation and shortage gaming [5], while solutions to reduce the impact of the bullwhip effect include reducing uncertainty, reducing variability, reducing lead time, and working strategically [6]. The bullwhip effect is calculated using the variance of incoming goods and incoming demand, as shown in the following equation [7]:

$$BWE = \frac{\sigma_{out}^2/\mu_{out}}{\sigma_{in}^2/\mu_{in}} \quad (1)$$

where,
BWE : bullwhip effect
σ^2 : variance in demand
μ : Average value
in : inbound orders,
out : outbound orders

By implementing an optimal inventory control policy, the bullwhip effect phenomenon can be avoided [1], [8]. Inventory is a warehouse item such as finished goods or semi-finished goods that are ready for sale or the production process [7]. Inventory management issues will arise if the quantity and time of ordering are incorrectly determined. The consequence of an error in inventory management, namely, the full storage capacity, results in excessive costs and the occurrence of lost sales. In general, inventory performance is measured by service level, which is to improve service and customer demand or to provide satisfaction to incoming customers. Costs will have an impact on inventory management accuracy. Some inventory management decisions include what items will be stored, where the storage will take place, how much quantity of goods should be stored when an item should be ordered, and what size order should be placed [9].

Controlling inventory and running simulations for comparison and evaluation of inventory control in research related to the bullwhip effect. The study's findings point to optimization in terms of the bullwhip effect, total cost, inventory performance [1], [8], [10], and average service level. As a result, the purpose of this study is to provide insight into solving the bullwhip effect phenomenon using the RQ Policy inventory policy approach available on anylogistix software and building three scenarios to determine the optimal policy for coca id.

*Corresponding author. Tel.: +62-853-9526-6606
Jalan Poros Malino km. 6, Bontomarannu
Gowa, Indonesia

AnyLogistix is a software that combines analytical and dynamic modeling to allow for in-depth analysis and evaluation of supply chain efficiency while taking opportunity into account. AnyLogistix allows you to visually model the logistics process while observing the dynamically analyzed system [11].

2. Research Method

The stages in the research are described as follows:

2.1. Data collections

Product data, demand data, incoming goods data, incoming demand data, warehouse capacity, lead time, and total costs incurred in coca id SMEs engaged in cup screen printing are the data used to solve the bullwhip effect problem with inventory management. Supporting data includes general MSME data and supply chain flow.

Table 1. Data on buying and selling prices of products

Products	Unit	Buying Prices (Rp)	Selling Prices (Rp)
Cup Screen Printing	Pcs	400	800

Table 2. Demand data and supply in 2021

Months	Supply	Demand
January	40.000	46.000
February	41.000	45.000
March	42.000	42.000
April	40.000	43.000
May	38.000	48.000
June	42.000	46.000
July	40.000	42.000
August	40.000	44.000
September	41.000	47.000
October	42.000	46.000
November	40.000	48.000
December	40.000	43.000

Table 3. Average cup demand in 2021

Consumer	Units	Time	Average Demand
Ruma.id	Pcs	Month	2.000
Kopita	Pcs	Month	1.000
Digit Coffe	Pcs	Month	4.000
Kopi Teori	Pcs	Month	5.000
Sekala Cafe	Pcs	Month	2.000
At 10 coffee	Pcs	Month	1.000
Adapada	Pcs	Month	2.000
Evlogi	Pcs	Month	2.000
Goffe	Pcs	Month	1.000
Biltea	Pcs	Month	5.000
Kedai Kopi Oma	Pcs	Month	1.000
Kaganga	Pcs	Month	1.000
Tastea	Pcs	Month	9.000
Delicate	Pcs	Month	3.000
45 Coffe	Pcs	Month	1.000
148 Coffe	Pcs	Month	2.000
Exposed	Pcs	Month	3.000

Table 4. Coca Id inventory

Initial Stocks	Capacity
20.000	20.000

Table 5. Total Cost on coca id

Type	Time	Cost (Rp)
Electricity	Months	Rp 350.000
Water	Months	Rp 150.000
Employee	Months	Rp 7.500.000
Place	Months	Rp 2.000.000
Machine	Months	Rp. 500.000

Figure 1. Coca id supply chain flow

Table 6. Delivery flow and lead time

From	Destination	Lead Time
Supplier Surabaya	Workshop Makassar	7 days
Workshop Coca id Makassar	All Customer	1 day

2.2. Data processing

In existing conditions, data processing is done manually, and proposals or problem solving is done with anylogistix simulation software and optimization tools.

Three scenarios are created in the anylogistix simulation and optimization tools software for data processing to determine the value of the bullwhip effect, total cost, and profit as a proposal for optimal improvements for coca id.

3. Results and Discussion

3.1. Determine of existing condition

The following are the results of the bullwhip effect calculation based on the data in Table 2 and Eq. (1):

Calculation of the average supply cups:

$$\mu = \frac{X_1 + X_2 + X_n}{n}$$

$$\mu_{in} = \frac{486.000}{12}$$

$$\mu_{in} = 40.500$$

Calculation of the average demand cups:

$$= \frac{X_1 + X_2 + X_n}{n}$$

$$\mu_{out} = \frac{540.000}{12}$$

$$\mu_{out} = 45.000$$

Calculation of variance of supply cups:

$$\sigma^2 = \sqrt{\frac{\sum(X_i - \mu)^2}{n}}$$

$$\sigma_{in}^2 = \sqrt{\frac{\begin{array}{c}(40.000-40.500)^2+(41.000-40.500)^2+\\(42.000-40.500)^2+(40.000-40.500)^2+\\(38.000-40.500)^2+(42.000-40.500)^2+\\(40.000-40.500)^2+(40.000-40.500)^2+\\(41.000-40.500)^2+(42.000-40.500)^2+\\(40.000-40.500)^2+(40.000-40.500)^2\end{array}}{12}}$$

$$\sigma_{in}^2 = \sqrt{\frac{\begin{array}{c}250.000+250.000+2.250.000+\\250.000+6.250.000+2.250.000+\\250.000+250.000+250.000+\\2.250.000+250.000+250.000\end{array}}{12}}$$

$$\sigma_{in}^2 = \sqrt{\frac{15.000.000}{12}}$$

$$\sigma_{in}^2 = \sqrt{1.250.000}$$

$$\sigma_{in}^2 = 1.118$$

Calculation of variance on demnand cups:

$$\sigma^2 = \sqrt{\frac{\sum(X_i-\mu)^2}{n}}$$

$$\sigma_{out}^2 = \sqrt{\frac{\begin{array}{c}(46.000-45.000)^2+(45.000-45.000)^2+\\(42.000-45.000)^2+(43.000-45.000)^2+\\(48.000-45.000)^2+(46.000-45.000)^2+\\(42.000-45.000)^2+(44.000-45.000)^2+\\(47.000-45.000)^2+(46.000-45.000)^2+\\(48.000-45.000)^2+(43.000-45.000)^2\end{array}}{12}}$$

$$\sigma_{out}^2 = \sqrt{\frac{\begin{array}{c}1.000.000+0+9.000.000+\\4.000.000+9.000.000+1.000.000+\\9.000.000+1.000.000+4.000.000+\\1.000.000+9.000.000+4.000.000\end{array}}{12}}$$

$$\sigma_{out}^2 = \sqrt{\frac{52.000.000}{12}}$$

$$\sigma_{out}^2 = \sqrt{4.333.333{,}33}$$

$$\sigma_{out}^2 = 2.081$$

The calculation of the bullwhip effect on the existing conditions in 2021 is:

$$BWE: \frac{\sigma 2_{Out}/\mu_{Out}}{\sigma 2_{In}/\mu_{In}}$$

$$\mu_{in} = 40.500$$

$$\mu_{out} = 45.000$$

$$\sigma_{out}^2 = 2.081$$

$$\sigma_{in}^2 = 1.118$$

$$BWE = \frac{2.081./45.000}{1.118/40.500}$$

$$BWE = \frac{0{,}05}{0{,}03} = 1{,}67$$

In the current situation, the bullwhip effect is 1.67, indicating that there is an intersection between supply and demand for 1 year.

3.2. Calculation of the service level of the existing condition

The equation used in anylogistix simulation software to get the service level value is:

$$Service\ Level = \frac{P1}{P2}$$

where,
P1: *Products in the successful orders*
P2: *Sum of all orders placed for facility*

$$Service\ Level = \frac{486.000}{540.000}$$

$$Service\ Level = 0{,}9$$

In the current state, the service level value is 0.9, indicating that there are incoming requests that cannot be fulfilled or that only 90% of requests can be fulfilled for one year.

3.3. Calculation of total cost in an existing condition

Using the data in Tables 1, 2, and 5 and the following equation, calculate the total cost:

Total Cost: Inventory Spend + Other Cost

where,
Inventory Spend : Buying Price x Total of supply cup
Other Cost : Facility Cost x Time

Calculation of inventory spend:

Inventory spend: 400 x 486.000
Inventory spend: Rp. 194.400.000

Calculation of other costs:

Other costs: 10.000.000 x 12
Other costs: Rp. 120.000.000

Calculation of *Total cost* on:

*Total Cost:*194.400.000 + 120.000.000
Total cost: Rp. 314.400.000

The total cost for a year in the current condition is Rp.314.400.000.

3.4. Calculation of the profit condition existing

The RQ Policy method was used to simulate three different inventory scenarios with capacities of 20,000, 25,000, and 30,000. A fixed replenishment point inventory policy / fixed replenishment quantity policy is referred to as an RQ policy. When the inventory level drops below the fixed replenishment point (R), the product's fixed replenishment quantity (Q) is ordered. The results of the inventory scenario simulation using anylogistix software are shown below:

Table 1. Scenario 1 of inventori 20.000 and Q: 20.000

R Value	Bullwhip Effect	Servic Level	Revenue	Total Cost	Profit
r: 3,000	0,35	0,62	Rp269.600.000	Rp254.950.000	Rp14.650.000
r: 4,000	0,71	0,76	Rp331.200.000	Rp290.550.000	Rp40.650.000
r: 5,000	0,71	0,76	Rp331.200.000	Rp290.550.000	Rp40.650.000
r: 6,000	0,71	0,76	Rp331.200.000	Rp290.550.000	Rp40.650.000
r: 7,000	0,71	0,76	Rp331.200.000	Rp290.550.000	Rp40.650.000
r: 8,000	1,05	0,79	Rp345.600.000	Rp292.550.000	Rp53.050.000
r: 9,000	0,35	0,79	Rp344.000.000	Rp292.950.000	Rp51.050.000
r: 10,000	0,50	0,83	Rp363.200.000	Rp303.350.000	Rp59.850.000
r: 11,000	1,27	0,85	Rp369.600.000	Rp305.350.000	Rp64.250.000
r: 12,000	1,11	0,81	Rp353.600.000	Rp299.350.000	Rp54.250.000
r: 13,000	1,11	0,81	Rp353.600.000	Rp296.950.000	Rp56.650.000
r: 14,000	0,53	0,81	Rp353.600.000	Rp299.350.000	Rp54.250.000
r: 15,000	0,83	0,81	Rp353.600.000	Rp297.750.000	Rp55.850.000

According to the simulation results table above, the bullwhip effect value does not reach 1, indicating that there is still a crossroads between incoming goods and incoming requests, as well as the service level, which does not reach 1, indicating that they have not been able to fulfill all incoming requests.

Table 2. Scenario 2 inventori 25.000 and Q: 25.000

R Value	Bullwhip Effect	Service Level	Revenue	Total Cost	Profit
r: 3,000	0,39	0,71	Rp308.800.000	Rp280.150.000	Rp28.650.000
r: 4,000	1,68	0,73	Rp316.800.000	Rp276.150.000	Rp40.650.000
r: 5,000	0,94	0,77	Rp334.400.000	Rp285.350.000	Rp49.050.000
r: 6,000	1,18	0,78	Rp340.800.000	Rp288.550.000	Rp52.250.000
r: 7,000	0,31	0,83	Rp363.200.000	Rp306.550.000	Rp56.650.000
r: 8,000	0,73	0,82	Rp356.000.000	Rp296.950.000	Rp59.050.000
r: 9,000	3,36	0,76	Rp330.400.000	Rp286.550.000	Rp43.850.000
r: 10,000	0,98	0,85	Rp372.800.000	Rp304.150.000	Rp68.650.000
r: 11,000	1,20	0,90	Rp393.600.000	Rp315.750.000	Rp77.850.000
r: 12,000	1,00	1,00	Rp436.800.000	Rp337.750.000	Rp99.050.000
r: 13,000	0,41	0,90	Rp392.800.000	Rp315.350.000	Rp77.450.000
r: 14,000	0,94	0,95	Rp412.800.000	Rp328.950.000	Rp83.850.000
r: 15,000	1,02	0,99	Rp432.800.000	Rp336.550.000	Rp96.250.000

According to the simulation results table above, with a value of R:12,000, the bullwhip effect touches number one, indicating that there is no bullwhip effect, and the service level also touches number one, indicating that all incoming orders can be fulfilled 100% of the time. with an Rp.99,050,000 profit and a total cost of Rp.337,750,000.

Table 3. Scenario 3 inventori 30.000 and Q: 30.000

R Value	Bullwhip Effect	Service Level	Revenue	Total Cost	Profit
r: 3,000	1,30	0,81	Rp352.000.000	Rp291.750.000	Rp60.250.000
r: 4,000	2,66	0,72	Rp313.600.000	Rp275.750.000	Rp37.850.000
r: 5,000	2,66	0,72	Rp313.600.000	Rp275.750.000	Rp37.850.000
r: 6,000	1,55	0,77	Rp336.800.000	Rp284.550.000	Rp52.250.000
r: 7,000	0,82	0,84	Rp368.800.000	Rp309.350.000	Rp59.450.000
r: 8,000	1,78	0,81	Rp354.400.000	Rp298.550.000	Rp55.850.000
r: 9,000	0,74	0,96	Rp419.200.000	Rp325.750.000	Rp93.450.000
r: 10,000	0,72	0,94	Rp410.400.000	Rp328.950.000	Rp81.450.000
r: 11,000	0,70	0,94	Rp410.400.000	Rp328.950.000	Rp81.450.000
r: 12,000	0,70	0,94	Rp410.400.000	Rp328.950.000	Rp81.450.000
r: 13,000	0,53	0,83	Rp360.800.000	Rp299.350.000	Rp61.450.000
r: 14,000	1,00	1,00	Rp436.800.000	Rp340.950.000	Rp95.850.000
r: 15,000	1,00	1,00	Rp436.800.000	Rp335.350.000	Rp101.450.000

According to the simulation results table above, with a value of R: 15,000, the bullwhip effect touches number 1, indicating that there is no bullwhip effect, and the service level also touches number 1, indicating that all incoming orders can be fulfilled 100 percent, the profit is Rp. 101,450,000, and the total cost is Rp. 335.350.000.

3.5. Inventory simulation on three different inventory scenarios

Based on the simulation results, it can be seen that the inventory model simulation results are more optimal than the existing methods on Coca id, as evidenced by the bullwhip effect, profit, total cost, and profit. According to the table above, the proposed new inventory policy and design had a positive impact, increasing the value of the bullwhip effect from 1.67 to 1, indicating that there is no bullwhip effect or no intersection between demand and ordering of goods, while the total costs increased. Rp. 314,400,000 to Rp. 335,350,000, while profit increases from Rp. 74,400,000 to Rp. 101,450,000.

4. Conclusion

Based on the simulation results, it can be seen that the inventory model simulation results are more optimal than the existing methods on Coca id, as evidenced by the bullwhip effect, profit, total cost, and profit. According to the table above, the proposed new inventory policy and design had a positive impact, increasing the value of the bullwhip effect from 1.67 to 1, indicating that there is no bullwhip effect or no intersection between demand and ordering of goods, while the total costs increased. Rp. 314,400,000 to Rp. 335,350,000, while profit increases from Rp. 74,400,000 to Rp. 101,450,000.

References

[1] F. Constantino, G. Di Gravio, A. Shaban, and M. Tronci, “SPC-Based Inventory Control Policy to Improve Supply Chain Dynamics,” *Int. J. Eng. Technol.*, vol. 6, pp. 418–426, 2014.

[2] A. Tanweer, Y.-Z. Li, G. Duan, and J.-Y. Song, “An Optimization Model for Mitigating Bullwhip-effect in a Two-echelon Supply Chain,” in *Procedia - Social and Behavioral Sciences*, B. Mao, Z. Tian, Z. Gao, H. Huang, and X. Feng, Eds., 2014, pp. 289–297. doi: 10.1016/j.sbspro.2014.07.206.

[3] I. Kholidasari, J. R. A. Bidiawati, and M. E. Sari, “The Evaluation of Bullwhip Effect on Distribution System of a Supply Chain using Centralized Demand Information Method,” in *IOP Conference Series: Materials Science and Engineering*, Padang: IOP Science, 2018, p. 012051. doi: 10.1088/1757-899X/602/1/012051.

[4] R. B. Handfield and E. L. Nichols, *Supply Chain Redesign: Transforming Supply Chains into Integrated Value Systems*. New Jersey: FT Press, 2022.

[5] H. L. Lee, V. Padmanabhan, and S. Whang, “Information Distortion in a Supply Chain: The Bullwhip Effect,” *Manage. Sci.*, vol. 43, no. 4, pp. 546–558, 1997.

[6] D. Simchi-Levi, P. Kaminsky, and E. Simchi-Levi, *Designing and Managing the Supply Chain: Concepts, Strategies, and Case Studies*, 3rd ed. McGraw-Hill/Irwin, 2008.

[7] J. Heizer and B. Render, *Principles of Operations Management: Sustainability and Supply Chain Management*, 9th ed. Pearson, 2014.

[8] F. Constantino, G. Di Gravio, A. Shaban, and M. Tronci, “Exploring the Bullwhip Effect and Inventory Stability in a Seasonal Supply Chain,” *Int. J. Eng. Bus. Manag.*, vol. 5, 2013, doi: 10.5772/56833.

[9] I. N. Pujawan and Mahendrawati, *Supply Chain Management*, 3rd ed. Yogyakarta: Penerbit ANDI, 2017.

[10] S. Kianfar, A. Saeidi, N. Nasr, and M. R. A. Jokar, “Measuring the Bullwhip Effect in Order-up-to Policies with Continuous and Periodic Review: A System Dynamics Simulation Approach,”

[11] M. Mratsenkova and K. Vaseliva, “Application of Anylogistix in Transport Chain Management,” in *Proceedings of University of Ruse*, 2020, pp. 28–32.

EPI International Journal of Engineering
Volume 8, Number 1, February 2025, pp. 50-61
DOI: 10.25042/epi-ije.022025.07

*p*ISSN 2615-5109
*e*ISSN 2621-0541

Thermal Performance of De'diba Kulong Ruma Bulongan for Residents Comfort

Icha Anggraini[a,]*, Ria Wikantari[b,], Baharuddin Hamzah[c]

[a]Department of Architecture, Faculty of Engineering, Hasanuddin University. Email: anggrianiichadesign@gmail.com
[b]Department of Architecture, Faculty of Engineering, Hasanuddin University. Email: rwikantaria@gmail.com
[c]Department of Architecture, Faculty of Engineering, Hasanuddin University. Email: baharsyah@yahoo.com

Abstract

The Bulungan Stilt House which in local language is called De'diba Kulong Ruma Bulongan has various floor heights of around 30cm, 50cm and 100cm. The difference in stilted floor height is expected to yield different thermal performance that affects occupant comfort. This study aims to: (1) explain the architectural characteristics of De'diba Kulong Ruma Bulongan and the existing conditions of thermal comfort of the occupants, and (2) analyze the effect of the floor height of De'diba Kulong Ruma Bulongan on the thermal comfort based on measurements and occupant perceptions, (3) explain the floor height performance on occupant thermal comfort as a function of climatic and environmental conditions. This research is quantitative, with a survey method using both qualitative and quantitative data. Data were collected through observation, thermal measurements, and distribution of questionnaires to 43 respondents who lived in 9 samples of Bulungan stilt houses. The analysis technique used PMV and PPD through the CBE thermal comfort tools, as well as cross-tabulation of questionnaire data. The results of the analysis of the psychrometric chart and the effective temperature chart at 13:00–14:00 WITA show that the highest average effective temperature in all measured stilt houses is in the range of 25.5-29°C. PMV analysis using the CBE thermal comfort tool shows that houses on stilts are most compliant with Ashrae 55 at a height of 100cm with PMV = 0.02 and PPD feel 5 % of a neutral value with an operating temperature of 25.5 - 27°C. Questionnaire analysis shows the most comfortable thermal reception according to the respondent's characteristics, namely occupants who are women, elderly (> 54 years old), and those who wear long loose gowns called gamis. The analysis of the occupants' perception shows that the most comfortable thermal reception at the four measurement points of the house on stilts is a house on stilts with a height of subsequently 100, 50, and 30 cm. This study concludes that the floor height affects thermal comfort in which the higher the stilted floor height in the architecture of the De'diba Kulong Ruma Bulongan the more comfortable for the occupants. This study also verifies that thermal comfort is influenced by climatic and environmental conditions.

Keywords: House on stilts, vernacular architecture, floor height, effective temperature, PMV, PPD, Ashrae 55 2020

1. Introduction

The dwelling house is a residential building or dwelling for primary needs which is essentially a place of return, rest, family gathering, sheltered from the scorching sun, rain, and other disturbances which offers comfort and safety to its occupants. The homes of Indonesians are generally adaptive buildings that consume less energy because they depend on the universe, and space efficiency can provide natural comfort for residents. It can be said that the comfort of the occupants of a dwelling house is better if the thermal performance of the space can meet the needs of a dwelling that realizes a safe and comfortable home. One of the indicators for analyzing the thermal performance of residential spaces is very closely related to the condition of residential buildings and the materials used.

*Corresponding author.
Jalan Poros Malino km. 6, Bontomarannu
Gowa, Indonesia, 92171

The form of local wisdom in the residential building architecture of the Bulungan community also has a legacy of past generations with local values, traditions, and cultural elements rich in local significance. From generation to generation, through trial and error, they have been preserved, giving rise to original works with a philosophy unanimously recognized as a comfortable home with cultural aspects, traditional values, and customs as well as the uniqueness to adapt to climate and environment. Bulungan community dwelling-house architecture has a characteristic in residential buildings, namely on a stage with the main material of wood which can become an icon of the capital of North Kalimantan province, in the Bulungan regency.

Bulungan Regency has a history of a sultanate that once triumphed, namely Bulungan Sultanate which is domiciled in Tanjung Palas. The glory of the Bulungan Sultanate has left a legacy in the form of original values, artifacts, documentation, and evidence in the Bulungan Sultanate Museum. One of its legacies is the richness of

traditional residential architecture with a vernacular conception in the form of a building on stilts developing in the Bulungan community. The physical form of the Bulungan Community Residential Building has similarities with the indigenous people of Bulungan Regency i.e. Dayak Tribe, Bulungan Tribe, and Tidung Tribe i.e. stilt houses.

Regional conditions and features of climatic and environmental adaptation affect the distinctiveness of residential buildings in the form of buildings on stilts. The Bulungan stilt house has a height of 30cm, 50cm, and 100cm on the stilt houses. This Bulungan stilt house is a residential architecture located in Bulungan Regency, the hallmark of this stage is used by residents. According to Bulungan traditional leader Datuk Abdul Hamid, the stilt house in the regional language term Bulungan can be known as De'diba Kulong Ruma Bulongan which means stilt house in Bulungan regency. De'diba Kulong Ruma Bulongan or the stilt house of the Bulungan community has been passed down from generation to generation through a process that the community says has adapted to the climate and environment which refers to a system of passive design to achieve thermal comfort for occupants.

Koppen climate distribution in the Kalimantan region affects the climate and environment of Bulungan Regency i.e. tropical rainforest (Af). This humid tropical climate with tropical rainforests or humid tropics covers the area around the equator characterized by precipitation (rain) and high humidity with almost always high temperatures in summer, little wind, moderate to strong, and little heat exchange due to high humidity in research by Lippsmeier in Sarjono [1]. According to Syafriny [2], in this humid tropical climate, thermal comfort has relatively high air temperature and humidity, causing situations that are sometimes thermally uncomfortable for humans.

The topography of the Bulungan region is also mostly forests and rivers with low soil types or tends to be flat with tidal river characteristics such that when heavy rainfall coincides with river tides, the Residential lands are often affected by flooding. And other conditions that cause thermal comfort problems in stilt houses are climates and environments with extreme weather conditions where the hottest temperature can also turn into heavy rain. High humidity with heavy rainfall causes soil features to be easily wet or waterlogged on the soil surface. On the other hand, he can feel a strong heat with the highest temperature during the day which can cause discomfort.

According to Gross in Angkasa [3], the Benefits of stilt houses include flood protection, maximization of views, expansion of ventilation, aesthetics, and application of sustainability principles. The house on stilts also allows narrow areas to be maximized with the bottom or under the house providing a ventilation function for the floor and the scenography also enhances the aesthetics. The space of the stilt house can be used for activities or to maximize the flow of wind into the house. It can be further classified as a traditional tropical house as a form of response to warm natural conditions to allow residents to get some fresh air in his research Suharjanto [4].

The Bulungan stilt house has different soffit heights ranging from 30 cm, 50 cm, and 100 cm which can also affect the thermal comfort of the occupants. The thermal performance of the various Bulungan community houses on stilts should ensure a comfortable temperature for the occupants. Because the comfort of a home is a psychological need that affects the health of the human mind, feelings, and body.

In addition, the stage form or under it can also be used as a unique or characteristic house in Bulungan Regency, North Kalimantan, which is aesthetically pleasing and suitable for residential purposes. Based on the above description, research is needed to reveal the state of the thermal environment and the level of thermal comfort experienced by the occupants. The results of this study serve as the basis for planning a comfortable stilt house for the residents of Bulungan Regency, North Kalimantan Province.

State of the art in this study we have chosen the case of houses on stilts but there are still few people who research the thermal comfort of houses on stilts under the house which is 100 cm high. This research uses a direct measurement method with a study of the literature. The perception of occupant satisfaction is very important to test the level of thermal comfort in a house on stilts which is strongly influenced by the height of De'diba Kulong Ruma Bulongan which is 100 cm. By using occupant perception to test the thermal comfort of this stilt house, it is hoped that the level of validity or accuracy of the thermal comfort rating can be a standard of measurement in further studies.

Research by A. Sholehah & Wulandari [5], conducted observations on sembau house construction to discover and learn local wisdom values of house construction seen from house layout. With the method of observation and interviews to produce a spatial arrangement in the construction of the sembau house. In further research, R. D. C. Sholehah [6] continued his research on the study of the construction of sembau houses based on the cultural traditions of the community and the elements of the physical system of these traditions and cultures. In sembau house research, the researcher uses sembau house as information about the De'diba Kulong Ruma Bulongan being researched. Wahyudi [7] also investigated thermal comfort in the North Kalimantan region by conducting direct field surveys or observing building shape and the shape of roof openings on longhouses and then taking direct measurements. At several points measuring temperature, humidity, and air movement. According to Soeroto [8], The house on stilts is guided by the traditional wisdom which calls for harmony between the macro-cosmos and the micro-cosmos; and therefore reflects the values of friendship and harmony with nature.

The Bulungan Stilt House in Fig. 1 shows the condition and characteristics of the buildings in the Bulungan Regency area which can be classified according to the height of 30 cm, 50 cm, and 100 cm from the flat ground surface. The house on stilts has similarities with the facade of the building, namely on the porch, the main door, windows, and ventilation (wind) with wide openings. The

main material of the wooden structure. The floors and walls are also made of wood. The thermal performance of Bulungan Stilt House is influenced by climatic and environmental conditions. These thermal conditions can have an impact on the comfort of the occupants.

Figure 1. Location photo of the Bulungan stilt house

2. Research Method

The location and research object of De'diba Kulong Ruma Bulongan or the stilt house in Fig. 2 with a height of 30 cm, 50 cm, and 100 cm are located in the regency of Bulungan, in the province of Kalimantan of the North.

Figure 2. Location of research sites description of the location and purpose of the stage house research

This research is mixed-method qualitative and quantitative with a paradigm of positivism [9]. The data collection technique is based on observation, thermal measurement, and the distribution of questionnaires to 43 samples of inhabitants in 9 stilt houses in Bulungan. The data was then analyzed using PMV and PPD analysis techniques through the CBE comfort thermal tools and crosstab analysis for the questionnaire results.

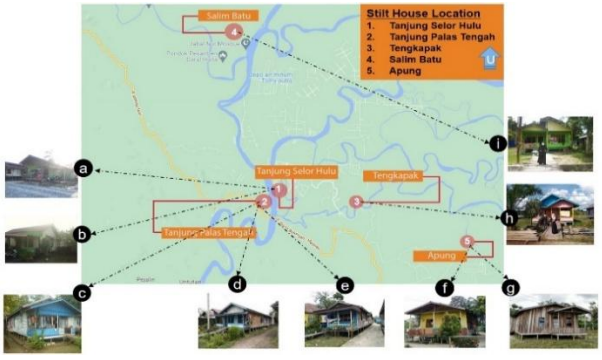

Figure 3. Location of sample stilt house

The researcher took data on the research object of De'diba Kulong Ruma Bulongan or the stilt house in Fig. 3 with direct field measurements in January, February, and March 2022. The conditions and characteristics of this Bulungan stilt house have similarities or similarities with the building facade and space layout. With the height of the stilt houses measuring 30 cm, 50 cm, and 100 cm, the measurements were taken at 1:00 p.m. – 2:00 p.m. WITA (60 minutes) in sunny weather with the measuring instrument used, namely Lutron LM 8000 4 In 1 placed ±80 cm above. The measurements will be compared to the standard Ashrae 55 [10], standard conditions of thermal comfort SNI 03-6572. Meanwhile, the air humidity for tropical areas according to SNI 03-6572-2001 is about 40% - 50%. A good air speed according to SNI 03-6572-2001 is 0.25 m/s with subject comfort and human behavior that adapts to local climatic conditions with the Fanger [11] with parameters based on the perception of air. ASHRAE and Bedford thermal comfort sensation scale [12].

The perception of occupants is the people who live in the house and so on. Architecture is essentially a space or an environment for humans. Dwelling houses are identical to the existence of humans inhabiting them for activities, communicating physically and psychologically as residents. The human as an inhabitant is an integral part of the home, of the intertwined culture and environment by Rapoport [13]. The human relationship with the house is one of interdependence, that is, humans affect the house, and vice versa, the house affects humans.

The adaptive theory assumes that people consciously or unconsciously respond to a given thermal environment in which they are exposed to restore their thermal comfort [11]. The recent development of the adaptive theory of thermal comfort explains occupants' thermal comfort in different environmental contexts, particularly in naturally conditioned buildings, from the point of view of the adaptive approach [14].

Newmark [15] stated that in addition to being a basic need to stay alive, it is also a basic need for security, a symbol of status, way of life, existence, and self-realization of residents. The presence of humans as inhabitants in the process of living or inhabiting creates a space with fully human values such as the behavior of the occupants. Human behavior as a resident greatly determines the quality and form of the house and its environment by Bell, Fischer, and Loomis [16].

3. Results and Discussion

3.1. Description of condition and characteristics the Ruma Bulungan

De'diba Kulong Ruma Bulongan or stilt house Bulungan due to its geographical location and topography has a humid tropical climate and is located between rivers, vacant land, and even virgin forest which creates buildings in the form of houses on stilts. Gross in Angkasa [3] concludes that the function of stilt houses is for buildings on loose ground, uneven land contours, river banks, swamps, and elevated areas and can maximize views, extend ventilation from below, add aesthetics, and apply the principles of sustainable development using natural

ventilation and the use of materials found in nature and the environment.

The conditions and characteristics of the De'diba Kulong Ruma Bulongan or Bulungan Stage House have similarities with the facade of the building, the spatial layout is almost the same as the original form of the Bulungan traditional house, and the houses of the indigenous people as a reference for researchers, namely dwelling houses still maintained. "De'diba Kulong Ruma Bulongan" is a Bulungan stilt house that is wide and square extend the rear with a porch on a typical building façade with ample natural ventilation on the main door, windows, and vents that work to catch the air entering the house.

The material of Bulungan stilt houses is wood which has long adapted to the topography of Bulungan Regency. This wooden material comes in the form of ironwood planks on the walls and floors, which helps to maximize the flow of wind through the texture pores on the wooden wall planks and the lower floor planks. The air system of the stilt house can also get good and fresh air inside the house.

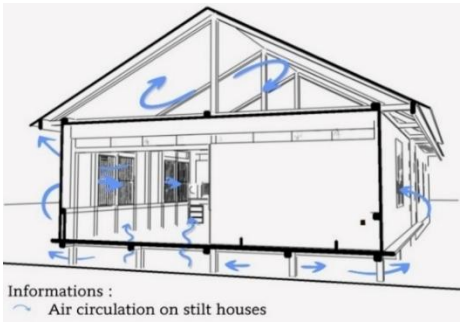

Figure 4. The air circulation system in the stilt house

The high thermal performance of De'diba Kulong Ruma Stage or Stilt House is influenced by the air circulation system or wind flow. Fig. 4 shows that air can flow in and out of windows, doors, and walls, the underside of the house, and turn in the roof openings.

Bulungan Stilt House or De'diba Kulong Ruma Bulongan has a simpler physical building than Bulungan Traditional House, Dayak Traditional House and Tidung Traditional House. According to the researchers' observations, the shape of the Bulungan stilt house is an elongated square without any special ornaments or patterns, colors, or meanings of the original culture or tradition. The three-tribe stilt houses adapt the environment to the space requirements as residential houses, both in traditional houses and De'diba Kulong Ruma Bulongan is believed to adjust the function of stilt houses as flood protection.

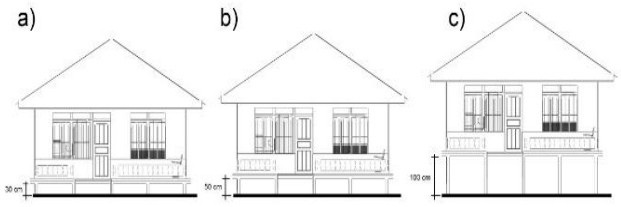

Figure 5. The height of the house on stilts

In Fig. 5, there are variations in the height of De'diba Kulong Ruma Bulongan, which are 30cm, 50cm, and 100cm from the surface of the flat ground having a stilt shape that has adapted to the local environment. According to Datuk Abdul Hamid (2019), the stilt houses functioned according to the livelihoods or needs of the residents, such as wood storage areas, cages, barns, and fishing boats.

The height of the stage is part of the subsoil which adapts to nature, and the environment, and avoids natural phenomena, namely flooding due to the overflow of river water and heavy rain or rain and soil wetting causing waterlogging of the soil surface.

Figure 6. Flooding on the stilt house

Fig. 6 shows that the Kayan River overflows from top to bottom when the river is at high tide and there is heavy rainfall. The high flow of river water at high tide can cross the periphery, drainage enters community settlements, and the tread condition is flat so that water overflows (often) causing of flooding Bulungan stilt houses.

Table 1. Description of research object house on stilts 30 cm high

No	Existing condition height of the house 30 cm	Information
1		The room with door openings, glazed windows, and ventilation left open. Orientation of the Building to the east
2		The room with door openings, glazed windows, and ventilation left open. Building orientation directly to the east
3		The room with door openings, glazed windows, and ventilation left open. Building orientation directly to the east

However, not only that, the thermal performance house on stilts is expected as a safe and comfortable residence, it must have a good performance for the comfort of the occupants. The thermal comfort from the height of the stilt

house can meet the climate and environment with the right design to avoid flooding at the highest temperature and humidity that can disturb residents so that it can offer thermal comfort for residents.

Table 1 shows that the height of 30 cm on the facade of the building and the opening planes of the doors, windows, and vents differ from houses 1, 2, and 3 in the East and West orientations.

Table 2. Description of research object house on stilts 50 cm high

No	Existing condition height of the house 30 cm	Information
1		Room with doors, windows, and ventilation openings left open. Building orientation facing to the west
2		Room with doors, windows, and ventilation openings left open. Orientation of the building direct to the southeast
3		Room with doors, windows, and ventilation openings left open. Orientation of the building direct to the south

Table 2 shows that the height of 50 cm has the same spatial arrangement and a different orientation from the sun. Orientation It can be seen on the floor plan which has openings in different directions.

Table 3. Description of research object house on stilts 100 cm high

No	Existing condition height of the house 30 cm	Information
1		Room with door openings, glazed windows, and ventilation left open. Building orientation directly to west
2		Room with door openings, glazed windows, and ventilation left open. Building orientation directly to west
3		Room with door openings, glazed windows, and ventilation left open. Building orientation directly to the east

Table 3 shows that the height of 100 cm on the facade of the building and the opening planes of doors, windows, and vents differ from houses 7, 8, and 9 in the East and West orientations.

The condition of the flat contour of the land and the ethnic value or the locality of the cultural traditions of the Bulungan people are associated with the stage elements in the stilt houses having the height of 30 cm, 50 cm, and 100 cm. The shape of the wide building extends rearwards according to the needs of the residential space with living rooms and family rooms connected without partitions where the facade of the building has a porch with openings for natural ventilation such as the main, door, windows and winds.

As for the embodiment of the Bulungan architectural building which is always applied to Bulungan regency community houses in Tables 1, 2, and 3, the stilt house building consists of three (3) parts, namely: Uma Ruma, Badan Ruma, Betis Ruma.

Figure 7. Bulungan stilt house division

De'diba Kulong Bulongan house or stilt house as figure 7 shows that there is a division of stilt houses in the Bulungan community. The stilt house division has an arrangement of the buildings of the traditional house in general, namely a traditional house with head, body, and leg elements, as follows:

1. Uma Ruma, namely the head or top of the house as a whole roof-to-ceiling structure (gypsum board);
2. Badan Ruma, namely the body or part of the house from the ceiling, walls, and floors that form spaces with partitions to become living rooms, family rooms, bedrooms, and others as required. The body or part of the wall has many doors, windows, and vents with wide openings to let air into and out of the building;
3. Betis Ruma, which is the foot or step of the house, serves to avoid the overflow of water from the Kayan River, heavy rainfall, and many swampy ground conditions that cause annual floods such as every 2 to 5 years, also protects against wild animals, reptiles and according to the beliefs of the ancient tribes of the interior. to avoid enemy attacks (foreigners), the results of an interview with Mr. Datuk Hamid.

From the results of field observations, it can be analyzed that De'diba Kulong Ruma or the Bulungan Community Stage House has a form of stilt house that takes the philosophy of the traditional forms of Bulungan, Dayak, and Tidung houses as natives of Bulungan Regency more simply without any ornaments or certain features, seen on the facade of the building as well as inside the building. The similarity of the Bulungan stilt

house is that the front of the building has a front terrace that is as wide as the building or part of the width of the building, the wide building extends to the back, all using materials in wood. The main door open and are wide, and the shutters, and ventilation is also wide using wood.

The room has a living room and a family room with wood plank walls with window openings and ventilation in every room. The floor is also made of wood planks covered with plastic carpets by residents. The Bulungan stilt house is a single square building that extbackwardwards. With this type of roofing a zinc covering is used, planar or a building prism. This means that the physical form of the building of the Bulungan stilt house has similarities or similarities, namely that the main material used is the best quality wood, namely Ulin. On the facade of the building there is a wide porch, wide door openings and glass windows. Maximum use of ventilation with openings left open during the day [17]. In the body of the building, the walls and floors are made of wooden planks which are sealed together, then have zinc roofing the with the ceiling and without ceiling, planar roofing and prism roofing or zinc at roofing.

The notable difference is the height of the different stilt houses, namely 30 cm, 50 cm and 100 cm. The different heights of the stilt houses, will affect the thermal performance of the occupants of the circulation of temperature, ventilation, maximum natural lighting entering the Bulungan stilt house from the underside or the floor of the house in wooden planks. De'diba Kulong Ruma Bulongan which was used as a sample of stilt houses in this study was located in the Bulungan community with the criteria of stilt houses having similarities in building facade and spatial arrangement which were distinguished by the location and direction to or orientation of the building.

Bulungan stilt house settlements form the architecture of community houses with the particularity of having stilt house height of 30cm, 50cm to 100cm formed linearly following the early pre-colonial developments, namely Bulungan Sultanate government s It was then consolidated and became the Community Establishments of Bulungan Regency. Settlements were formed based on the Kayan River which was the source of life, transportation, facilities, and infrastructure in pre-colonial times, namely during the rule of Bulungan Sultanate. The residential development pattern develops linearly along the Kayan River and its spreading tributaries, clustering together to form houses on stilts around the river. Because the area is so large and there are still a lot of forests and the population is still small, there are still a lot of vacant land.

The conditions and characteristics of this Bulungan stilt house have similarities in the facade of the building extending to the rear, there is a wide terrace with door openings, glass windows, ventilation using materials in wood with openings that can be opened or closed on a large roof, frames, shutters and wide doors. Conditions and features are close to the river and there are vacant lands and a single building. With t environmental conditions often experience the phenomenon of flooding due to the widening of the river when the river is at high tide.

3.2. De'diba Kulong Ruma Bulongan's elevated analysis of thermal comfort variables that significantly affect occupant satisfaction

3.2.1. De'diba Kulong Ruma Bulongan with a height of 30 cm

The measurement results in Fig. 8 show that the temperature value of stilt house 001 is 1°C lower than that of stilt houses 002 and 003 influenced by the direction facing the facade and the floor plan has a different measuring point aperture.

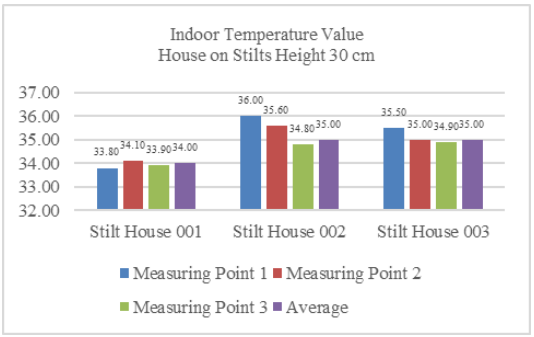

Figure 8. Average temperature value 30 cm high stilt house

The measurement results in Fig. 9 show that the highest humidity value of the stilt house 001 is 1% of the stilt house 002 and 4% of the stilt house 003 is affected by the location near the river.

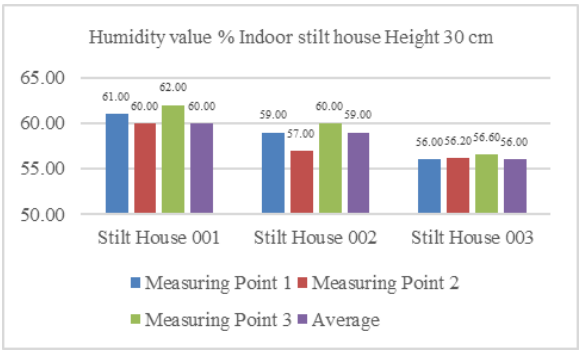

Figure 9. Average humidity value 30 cm high stilt house

The measurement results in Fig. 10 show that the wind speed values for stilt houses 001, 002 and 003 are influenced by location conditions and cardinal directions of airflow in the room of the house. on stilts with a house height of 30 cm. It is not felt because it does not exceed 0.15 m/s or 0.25 m/s.

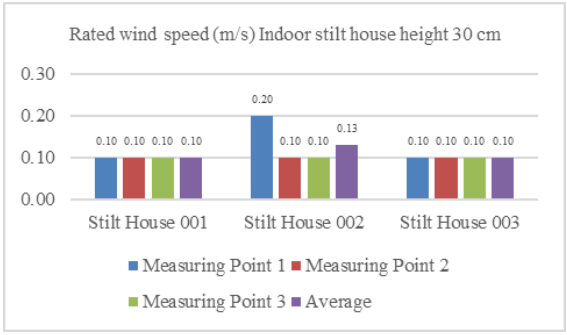

Figure 10. Average wind speed value 30 cm high stilt house

3.2.2. De'diba Kulong Ruma Bulongan with a height of 50 cm

The measurement results in Fig. 11 show that the temperature value of Stage House 005 is 2-4°C lower than that of Stage House 004 and 006 due to the direction of the facade facing the sun with the same layout with different locations. Stilt house 005 is near the river and some trees that affect different outcomes. The 004 stilt houses have openings on the north side but are very close to the river which reflects the heat directly into the house without being obstructed by tall vegetation, as in the 005 and 006 stilt houses which have openings on the south-west side and west, however, the heat of the sun is blocked by the trees on that side.

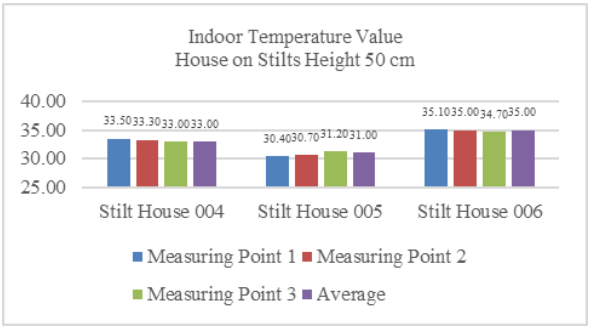

Figure 11. Average temperature value 50 cm high stilt house

The measurement results in Fig. 12 show that the humidity value of the stilt house 005 is 67% higher than that of the stilt houses 004 and 006. in the air of the stilt house.

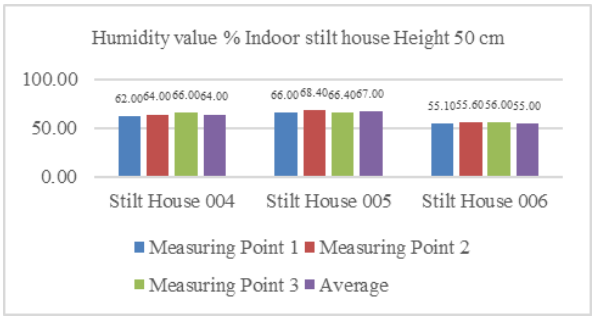

Figure 12. Average humidity value 50 cm high stilt house

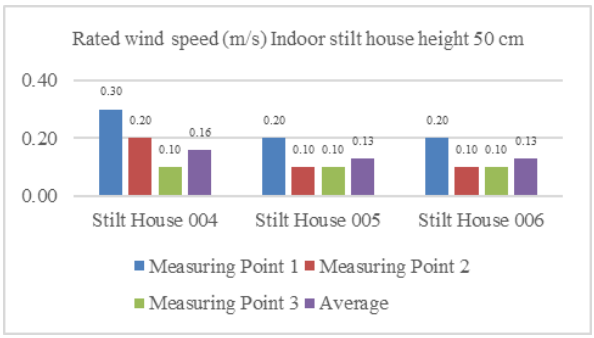

Figure 13. Average wind speed value 50 cm high stilt house

The measurement results in Fig. 13 show that the temperature value of the stilt house 004 is 3°C higher than that of the stilt house 005 and 006 influenced by the direction of the face and the layout of the floor plan. The floor has a different metering point aperture. The 004 stilt houses have an opening on the north side but are very close to the river so that the air enters the house directly without being obstructed by tall vegetation, as in the 005 and 006 stilt houses which have openings on the south side -west and west sides but are blocked by trees on that side.

3.2.3. De'diba Kulong Ruma Bulongan with a height of 100 cm

The measurement results in Fig. 14 show that the temperature values for the Stilt Houses 007, 008, and 009 have the same result of 31°C with the influence of the orientation facing the facade and the layout of the floor plan. floors having openings at different measuring points.

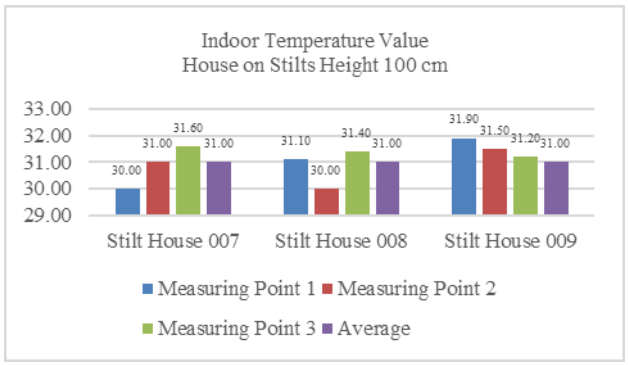

Figure 14. Average temperature value 100 cm high stilt house

The measurement results in Fig. 15 show that the humidity value of Stage House 009 is 5-9°C lower than that of Stage House 007 and 008 due to the direction facing the facade and the layout. of the floor plan with openings at various measurement points.

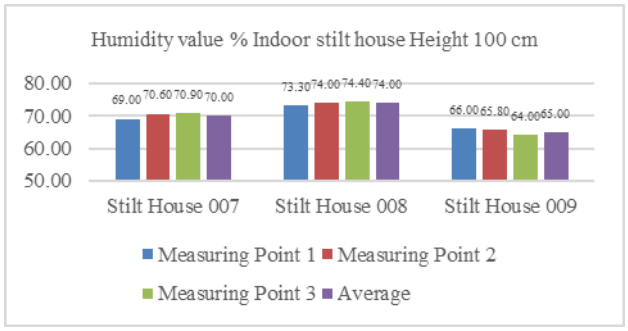

Figure 15. Average humidity value 100 cm high stilt house

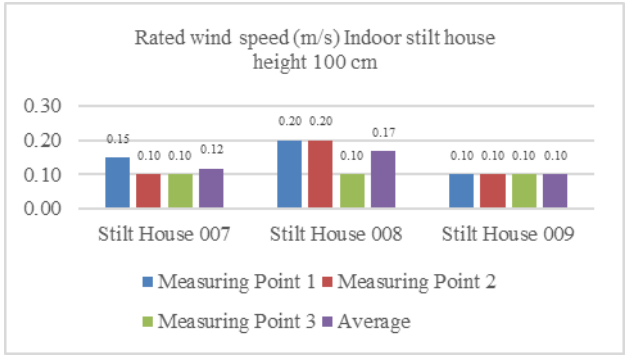

Figure 16. Average wind speed value 100 cm high stilt house

The measurement results in Fig. 16 show that the wind speed of the 009 stage house is 0.10m/s, which is not felt in the room, as well as the 007 stage house and the stage 008 is 0.12 to 0.17 m/s.

3.3. Bulungan stilt house effective temperature value analysis comparative results

3.3.1. Comparison of the average effective temperature of houses on stilts Height 30, 50, 100 cm

Fig. 17 shows that the average effective temperature of a 30 cm high stilt house is 27°C, a 50 cm high stilt house is 28°C, and a 100 cm high stilt house is 28°C - 29°C. The most comfortable thermal condition of a stilt house for residents is a stilt house with a height of 100 cm.

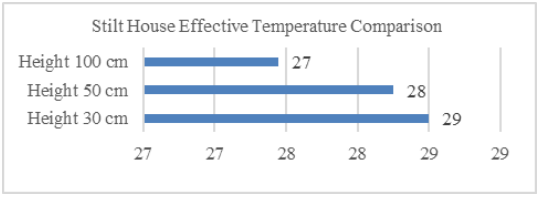

Figure 17. Comparison of effective temperatures of houses on stilts at 30, 50, 100 cm in height

3.3.2. Comparison of the average effective temperature of houses on stilts Height 30, 50, 100 cm

Fig. 18 shows that the average humidity of a stilt house with a height of 30 cm is 58%, a house on stilts with a height of 50 cm is 60% and a house on stilts with a height of 100 cm is 65%. The thermal conditions of houses on stilts for residents, and relative humidity for tropical areas according to SNI 03-6572-2001 is about 40% - 50%. A room with a solid capacity like a meeting room has a recommended relative humidity between 55% and 60%, namely on stilt houses with a height of 30 cm and 50 cm.

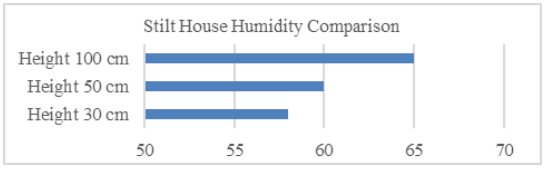

Figure 18. Humidity comparison of houses on stilts with a height of 30, 50, 100 cm

3.3.3. Comparison of the average effective temperature of houses on stilts Height 30, 50, 100 cm

Fig. 19 shows that the average wind speed of a 30 cm high stilt house is 0.11 m/s, a 50 cm high stilt house is 0.13 m/s and a on piles 100 cm high is 0.14 m/s. The thermal state of the house on stilts for residents with the wind speed according to SNI 03-6572-2001 is 0.25 m/s. The airspeed can be made higher than 0.25m/s depending on the dry air temperature conditions in the room. With the highest average effective temperature of all Bulungan stilt houses in the range of 25.5-29°C. So the air pressure is felt as static or airflow which can barely be felt in the room on a stilt house.

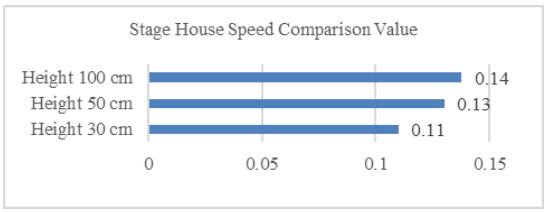

Figure 19. Comparison of wind speeds in a house on stilts at an altitude of 30, 50, 100 cm

3.4. Analysis of the thermal comfort of the occupants via the thermal comfort tool CBE (Ashrae 55)

3.4.1. De'diba Kulong Ruma Bulongan with a height of 30 cm

Fig. 20 shows that the thermal comfort of the measurement data of house 001 on stilts does not respect the Ashrae 55-2020 standard, PMV = 0.83 and PPD = 19% SET = 27.8°C where the individual feels a bit warm.

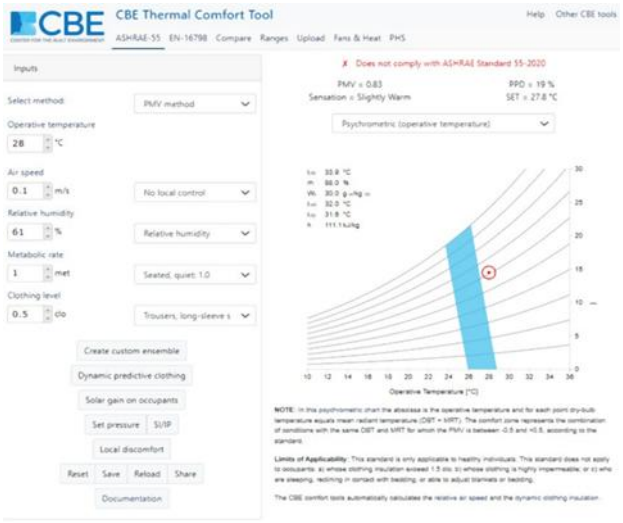

Figure 20. CBE occupant of stilt house 001

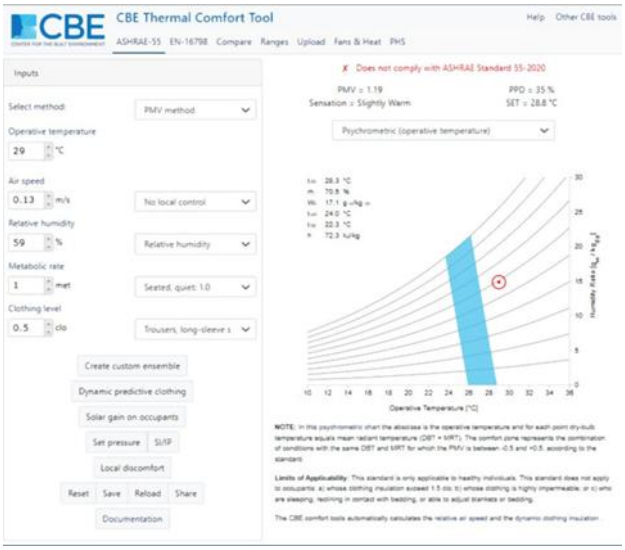

Figure 21. CBE occupant of stilt house 002

Fig. 21 shows that the thermal comfort measurement data of Stilt House 002 does not meet the Ashrae 55-2020

standard, PMV = 1.19 and PPD = 35% SET = 28.8° where the individual feels a bit hot.

Fig. 22 shows that the thermal comfort measurement data for Stilt House 003 does not meet Ashrae 55-2020 standards, PMV = 0.78 and PPD = 18% SET = 27.5° where the individual feels a bit hot.

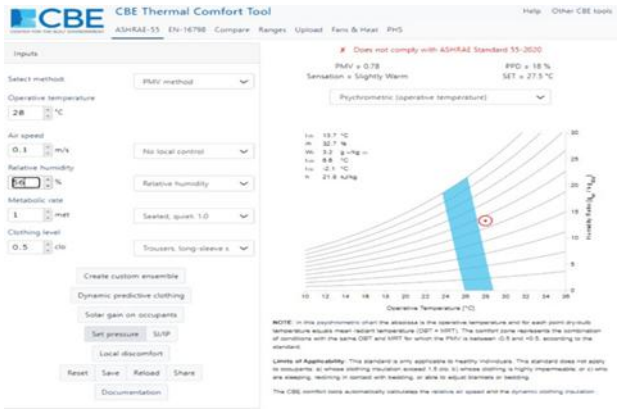

Figure 22. CBE occupant of stilt house 003

3.4.2. De'diba Kulong Ruma Bulongan with a height of 50 cm

Fig. 23 shows that the thermal comfort of the measurement data of house 004 on stilts does not respect the Ashrae 55-2020 standard, PMV = 0.74 and PPD = 17% SET = 27.5°C where the individual feels a bit warm.

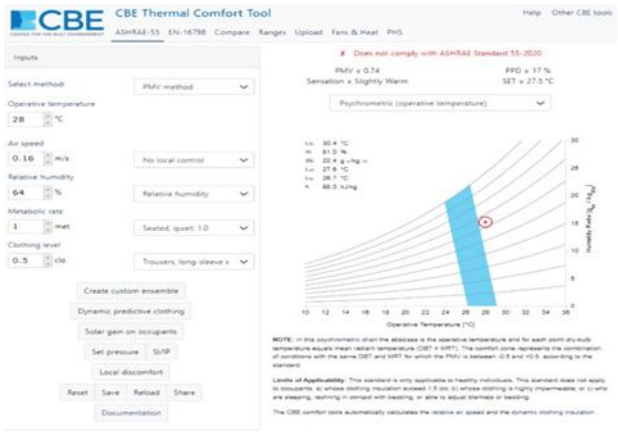

Figure 23. CBE occupant of stilt house 004

Figure 24. CBE occupant of stilt house 005

Fig. 24 shows that the thermal comfort measurement data for Stilt House 005 meets the Ashrae 55-2020 standard with PMV = 0.46 and PPD = 9% SET = 26.6°C, where the individual feels neutral.

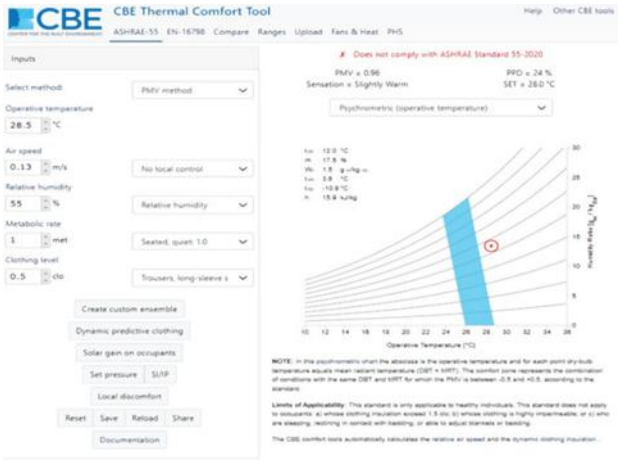

Figure 25. CBE occupant of stilt house 006

Fig. 25 shows that the thermal comfort of the stilt house 006 measurement data meets the Ashrae 55-2020 standard with PMV = 0.96 and PPD = 24% SET = 28°C, where the individual feels a little hot.

3.4.3. De'diba Kulong Ruma Bulongan with a height of 100 cm

Figure 26. CBE occupant of stilt house 007

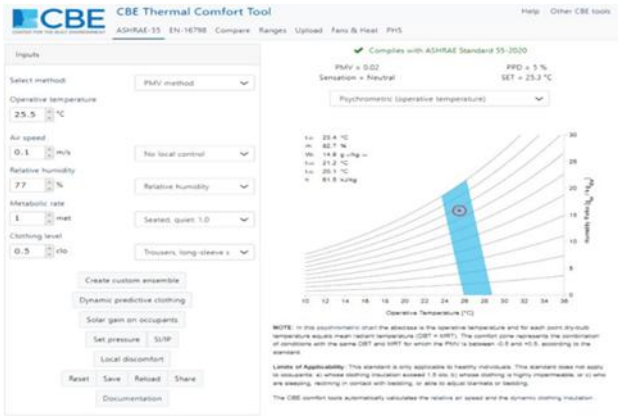

Figure 27. CBE occupant of stilt house 008

Fig. 26 shows that the thermal comfort of the stilt house 007 measurement data meets the Ashrae 55-2020 standard with PMV = 0.46 and PPD = 9% SET = 26.8°C where the individual feels neutral.

Fig. 27 shows that the thermal comfort measurement data of stilt house 008 meets the Ashrae 55-2020 standard with PMV = 0.02 and PPD = 5% SET = 25.3°C, where the individual feels neutral.

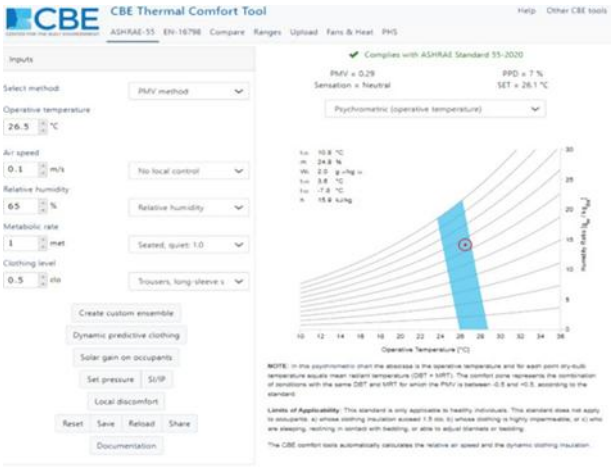

Figure 28. CBE occupant of stilt house 009

Fig. 28 shows that the thermal comfort of the stilt house 009 measurement data meets the Ashrae 55-2020 standard with PMV = 0.29 and PPD = 7% SET = 26.1°C, where the individual feels neutral.

3.5. Comparison of average results analysis of thermal comfort measurements according to the Ashrae 55

3.5.1. The average effective temperature of the stilt house

The average effective temperature of a 30 cm high stilt house is 27°C, a 50 cm high stilt house is 28°C, and a 100 cm high stilt house high is 29°C. The most comfortable thermal condition of a stilt house for residents is in a stilt house with a height of 100 cm.

3.5.2. The average stage house humidity value

The average humidity of a 30cm high stilt house is 58%, a 50cm high stilt house is 60%, and a 100cm high stilt house high is 65%. The thermal conditions of houses on stilts for residents, the relative humidity for tropical areas according to SNI 03-6572-2001 is about 40% - 50%. A room with a solid capacity like a meeting room has a recommended relative humidity between 55% and 60%, namely on stilt houses with a height of 30 cm and 50 cm.

3.5.3. Stage house average wind speed

The average wind speed of a 30 cm high stilt house is 0.11 m/s, a 50 cm high stilt house is 0.13 m/s and a on piles 100 cm high is 0.14 m/s. The thermal state of the house on stilts for residents with the wind speed according to SNI 03-6572-2001 is 0.25 m/s. The airspeed made higher than 0.25m/s depending on the dry air temperature conditions in the room.

The results of the analysis show that the correlation between the measurement results is directly addressed using the effective temperature and in the CBE analysis the thermal comfort tools are compared to the perceptions of the inhabitants of the stilt house at a height of 100 cm with a sense of net worth that can be felt by residents. Air circulation through the opening with the direction facing the opening also affects the thermal performance of the stilt house for the comfort of the occupants. With a height of 100cm, it can meet the thermal comfort standard for a Bulungan stilt house rather than a height of 50 cm and 30 cm.

3.6. Thermal comfort analysis based on occupant perception

3.6.1. Perception of comfort according to the gender on occupant perception

In this case, Fig. 29 shows there are differences in male and female respondents which the acceptance of the thermal conditions of the stilt houses of the female respondents is better than that of the male respondents. Male respondents are hardly too far away from feeling the thermal performance of stilt houses. Based on the measurement point, the highest level of comfort perception is in the living room, followed by the family bedroom and the intermediate bedroom. Meanwhile, the lowest perceived level of comfort is on the terrace of the house.

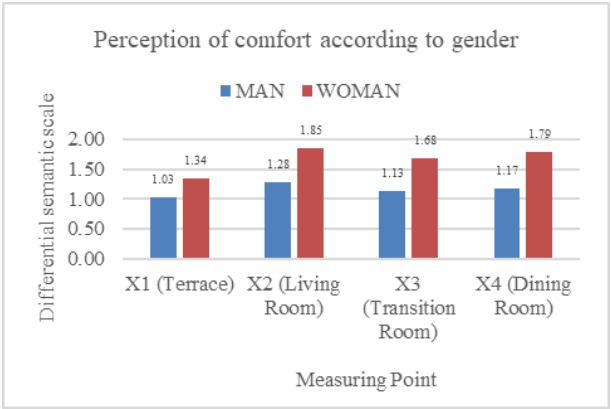

Figure 29. Perception of thermal comfort of occupants of Stage House Bulungan by gender

3.6.2. Perception of comfort according to age on occupant perception

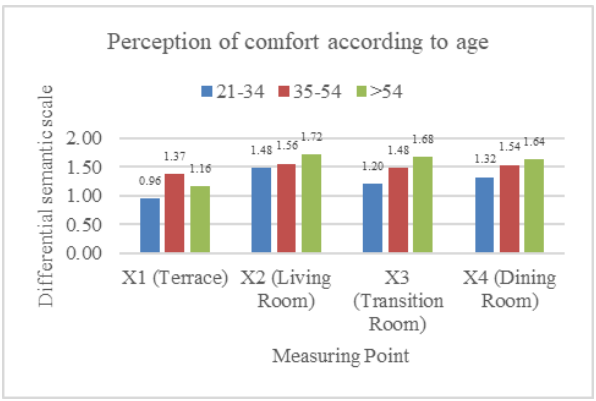

Figure 30. Perception of the thermal comfort of the occupants of the Bulungan Stage House according to age

Based on Fig. 30, shows that the results of the distribution of questionnaires regarding the respondents' acceptance of the thermal conditions of houses on stilts are classified by age at four measurement points, namely the terrace, the living room, the room, intermediate and the family room. The oldest age group (>54 years) shows in this case a better acceptance of thermal conditions, followed by the adult age group (35-54 years), while the lowest level of perception is that of adolescent respondents (21-34 years old). According to the point of measurement, the highest level of perceived comfort is found in the living room, followed by the family room and the intermediate space. Meanwhile, the lowest perceived level of comfort is on the terrace of the house.

3.6.3. Perception of comfort based on clothing insulation

The results of the questionnaire in Fig. 31 show that the acceptance of thermal comfort by the respondent according to the type of clothing worn at four measurement points, namely the terrace, the living room, the intermediate bedroom and the family room, the results show that most of the measuring points are at a rather comfortable and comfortable level in the dresses. Judging by the type of clothing worn, Gamis in this case shows the best acceptance of thermal conditions, followed by negligee and batik.

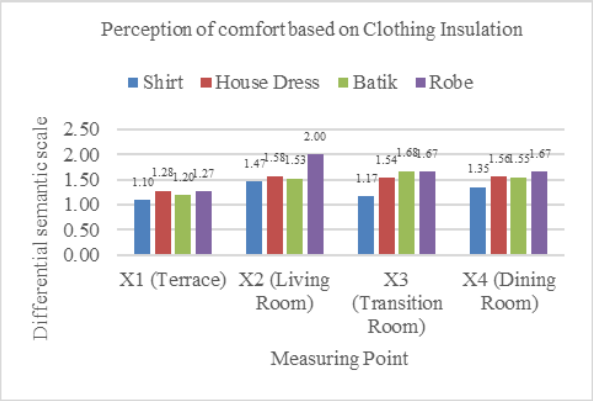

Figure 31. Perception of the thermal comfort of the occupants of the Bulungan stilt house according to the insulation of clothing

The lowest level of perception is that of respondents who wear t-shirts. The gamis is carried by the age group > 54 years where the previous measure shows the highest satisfaction among all age categories. Meanwhile, t-shirts are mostly worn by teenagers whose previous body measurements show the lowest comfort level of all age categories. According to the location of the measurement point, the highest level of perceived comfort is found in the living room, followed by the family room and the intermediate space. Meanwhile, the lowest perceived level of comfort is on the terrace of the house.

3.6.4. Perception of comfort based on stage height

Fig. 32 shows that De'diba Kulong Ruma Bulongan or Bulungan stilt house was made by collecting questionnaire data which used as respondents composed of 31 men and 37 women to determine the perceptions of the residents. Occupants of houses on stilts on the based on the results of a questionnaire relating to the acceptance by the respondents of the thermal comfort according to the heights of the floor at four points of measurement, namely the terrace, the living room, the intermediate room and the family room, it was found that most of the measuring points were at a comfortable level, except on the terrace of the house whose height of 30 cm is at a rather comfortable level. The highest comfort perception at 3 (three) measurement points in the house is a height of 100 cm, followed by 50 cm and 30 cm.

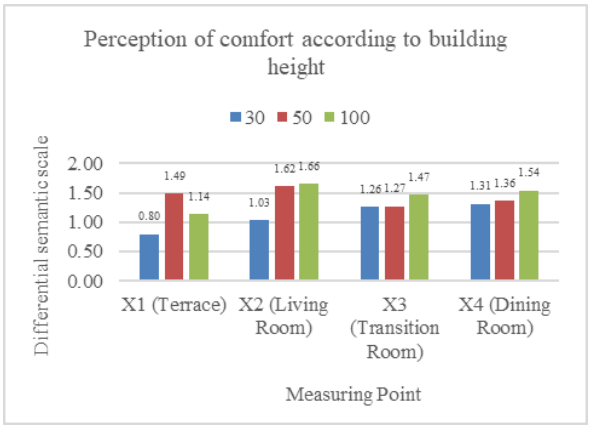

Figure 32. Perception of the thermal comfort of the occupants of the houses on stilts in Bulungan according to the height of the building

While on the terrace of the house, the highest perception of comfort is at a height of 50 cm, followed by 100 cm and 30 cm. Depending on the location of the measurement points, the living room at a height of 50 and 100 shows the most comfortable perception of the occupants, while the terrace at a height of 30 cm shows the lowest perception.

5. Conclusion

Based on the results of the study, the architecture of De'diba Kulong Ruma Bulongan represents a traditional stilt house located in a riverside environment surrounded by open land, including community land, forest areas, and uncultivated land. The building orientation generally faces west or east, with a mass composition extending toward the rear and displaying characteristic elements of the head, body, and legs on the façade. The spatial arrangement consists of a terrace, living room, middle bedroom, and family room. The house also features a wide porch, large main door openings, broad windows, and ventilation openings that support natural air circulation. The lower construction system uses wooden supporting poles with floor heights of approximately 30 cm, 50 cm, and 100 cm above ground level.

The findings indicate that the height of the stilt floor significantly affects the thermal comfort of the occupants. A floor height of 30 cm was perceived as uncomfortable, while a height of 50 cm was considered somewhat comfortable or slightly warm. In contrast, a height of 100 cm provided a neutral and comfortable thermal condition for the occupants. The perception analysis further revealed that elderly women experienced the highest level of comfort in the stilt house. Furthermore, the thermal performance of De'diba Kulong Ruma Bulongan is

strongly influenced by floor height, which is closely related to the local climate and environmental conditions. Simulation results conducted over a 24-hour period, particularly during daytime hours from 10:00 a.m. to 3:00 p.m., showed that the house still experienced uncomfortable temperature levels due to high air temperatures, especially between 1:00 p.m. and 2:00 p.m.

References

[1] A. B. Sardjono, "Respon Rumah Tradisional Kudus terhadap Iklim Tropis," *Modul*, vol. 11, no. 1, pp. 7–16, 2011, doi: 10.14710/mdl.11.1.2011.%p.

[2] R. Syafriny and Sangkertadi, "Perbandingan Pengaruh Suhu Lingkungan pada Kenyamanan Termis di Ruang Luar dan Ruang Dalam di Iklim Tropis Lembab bagi Manusia Beraktifitas Moderat," *Media Matrasain*, vol. 9, no. 1, pp. 26–35, 2012, doi: 10.35793/matrasain.v9i1.668.

[3] Z. Angkasa, "Penerapan Konsep Arsitektur Rumah Panggung di Lingkungan Perkotaan," *Arsir J. Arsit.*, vol. 1, no. 2, pp. 175–183, 2017, doi: 10.32502/arsir.v1i2.880.

[4] G. Suharjanto, "Membandingkan Istilah Arsitektur Tradisional Versus Arsitektur Vernakular: Studi Kasus Bangunan Minangkabau dan Bangunan Bali," *ComTech Comput. Math. Eng. Appl.*, vol. 2, no. 2, pp. 592–602, 2011, doi: 10.21512/comtech.v2i2.2808.

[5] Sholehah, Antariksa, and L. D. Wulandari, "Tatanan Spasial pada Bangunan Rumah Sembau Suku Bulungan di Tanjung Palas, Kalimantan Utara," *J. Perspekt. Arsit.*, vol. 9, no. 1, pp. 8–20, 2014, doi: 10.36873/jpa.v9i01.8945.

[6] Sholehah and R. D. Christyanti, "Tradisi Budaya pada Sistem Fisik Bangunan Rumah Sembau Suku Bulungan di Tanjung Palas Kalimantan Utara," *PROKONS J. Tek. Sipil*, vol. 10, no. 2, pp. 100–108, 2016.

[7] E. Wahyudi, "Pengaruh Bentuk Bukaan Atap Bangunan terhadap Tingkat Kenyamanan Termal pada Rumah Panjang Suku Dayak Brusu Kecamatan Sekatak Kalimantan Utara," *Borneo Eng. J. Tek. Sipil*, vol. 2, no. 2, pp. 94–104, 2018, doi: 10.35334/be.v2i2.617.

[8] M. Soeroto, *Dari Arsitektur Tradisional Menuju Arsitektur Indonesia*, Cetakan 1. Jakarta: Ghalia Indonesia, 2003.

[9] J. W. Cresswell, "Qualitative, Quantitative, and Mixed Methods Approaches," pp. 3–5, 2017.

[10] ASHRAE, "Thermal Environmental Conditions for Human Occupancy," Atlanta, ANSI/ASHRAE Standard 55-2004, 2004.

[11] J. F. Nicol and M. A. Humphreys, "Adaptive Thermal Comfort and Sustainable Thermal Standards for Buildings," *Energy Build.*, vol. 34, no. 6, pp. 563–572, 2002, doi: 10.1016/S0378-7788(02)00006-3.

[12] ASHRAE, *ASHRAE*. Atlanta US, 2017.

[13] M. J. Rapoport *et al.*, "The Relationship between Cognitive Performance, Perceptions of Driving Comfort and Abilities, and Self-Reported Driving Restrictions among Healthy Older Drivers," *Accid. Anal. Prev.*, vol. 61, pp. 288–295, 2013, doi: 10.1016/j.aap.2013.03.030.

[14] G. S. Brager and R. de Dear, "A Standard for Natural Ventilation," *ASHRAE J.*, vol. 42, no. 10, pp. 21–27, 2000.

[15] T. L. Conklin, "Self-Sufficiency Programs in Hampton Public Housing," Virginia Polytechnic Institute and State University (Virginia Tech), 1994.

[16] S. A. Indriyati, "Adaptation Behaviour of Residents Living in a High-Density Housing in Jakarta." Citeseer, 2004.

[17] H. B. Rijal, M. A. Humphreys, and J. F. Nicol, "Development of a Window Opening Algorithm Based on Adaptive Thermal Comfort to Predict Occupant Behavior in Japanese Dwellings," *Japan Archit. Rev.*, vol. 1, no. 3, pp. 310–321, 2018, doi: 10.1002/2475-8876.12043.

EPI International Journal of Engineering
Volume 8, Number 1, February 2025, pp. 62-67
DOI: 10.25042/epi-ije.022025.08

*p*ISSN 2615-5109
*e*ISSN 2621-0541

Characteristics of Filament From Extrusion Result of Low-Density Polyethylene Plastic Waste using Extrusion Method for 3D Printing Filament Applications

Muhammad Ali Chandra[a,*], Onny Sutresman[b], Fauzan Djamaluddin[c]

[a]Department of Mechanical Engineering, Faculty of Engineering, University of Hasanuddin. Email: muhammadalichandra@gmail.com
[b]Department of Mechanical Engineering, Faculty of Engineering, University of Hasanuddin. Email: onny.sutresman@gmail.com
[c]Department of Mechanical Engineering, Faculty of Engineering, University of Hasanuddin. Email: fauzanman77@yahoo.com

Abstract

Low-Density Polyethylene (LDPE) plastic is a material that is widely used by the industry as packaging. However, the manufacturing industry players do not place environmental issues as the main focus in the supply of products. This study aims to analyze the characteristics of LDPE plastic waste that is formed into filaments for 3D printing filament applications. The research variables analyzed were the temperature of the test sample at 170 °C, 180 °C, 190 °C, 200 ºC, 210 °C, and 220 °C. The filament analysis process is to form LDPE plastic waste into 3D printing filaments using a plastic waste extrusion machine. The hardness test was then carried out using a digital Shore A Durometer Hardness tool. Furthermore, a microstructure test was also carried out using SEM (Scanning Electron Microscope). The results of the hardness test obtained show that the specimen temperature of 210 °C has the highest hardness value, which is in the range of 83–89.5 HA. In the meantime, specimens at 180 °C had the lowest hardness values, ranging from 59.5 to 71.5 HA. In addition, the SEM test resulted in the sample surface not being very flat at temperatures of 170 °C, 180 °C, and 190 °C, while the sample surface was quite flat at temperatures of 200 °C, 210 °C, and 220 °C.

Keywords: Low-density polyethylene; plastic waste; scanning electron microscope; shore a durometer

1. Introduction

Many plastics produced and used by humans end up in nature, causing damage to living things and the environment [1]. However, the handling of plastic waste has not been given much attention by several manufacturing industries that produce goods. The reason is that the players in the manufacturing industry do not place their main focus on environmental issues. In addition, some industries only use plastic as an ingredient in production without thinking about recycling it into new products. This results in the absence of plastic waste handling by the industry itself. Even though the level of plastic waste produced in the world continues to increase, reaching around 381 million tons in 2015 [2].

A Plastic extruder machine is a machine that serves to extrude plastic into solid filaments. After extruding plastic, many benefits can be utilized from plastic, for example in the blow molding extrusion process which makes it into hollow plastic products such as bottles, tubes, and gallons [3]. The plastic extrusion process is a widely recognized technique in the polymer industry [4].

From this extrusion technique, the industry has developed an extruder machine for plastics. By relying on heating from the barrel and lead screw, the plastic can be melted and delivered to the end of the barrel. To produce good-quality plastic products, the hot temperature in the barrel is very influential. Therefore, temperature control on the engine is very necessary because each type of plastic has a different heat character [5]. One of the uses of extrusion machines is that the results of the extrusion produce 3D printing filaments. 3D printing filament made from plastic waste is one solution for the manufacturing industry to reduce the presence of plastic waste today [6].

Hardness testing is a test indicator to determine the hardness of a material. One of the hardness testing tools for plastic materials that can be used is the Shore a Durometer. There are eight types of durometer scale classification, namely A, B, C, D, DO, O, OO, and M. The determination of the scale used depends on the type of material and the level of hardness of the material [7].

A Scanning Electron Microscope (SEM) is an electron microscope designed to directly observe the surface of solid objects. SEM testing is intended to determine the particles in the sample and the surface flatness of the sample. The combination of high magnification, large depth of field, good resolution, and

*Corresponding author. Tel.: +62-852-35809-787
Sultan Alaudin 2 Residence
Makassar, Indonesia, 90221

the ability to know the composition and crystallographic information makes SEM widely used for research and industrial purposes [8].

To get the performance level of the extrusion machine process as expected, it is considered necessary to analyze the plastic waste category of low-density polyethylene on the extruder machine by producing 3D printing filaments so that the exact control parameters of the melt extrusion machine can be known and are expected to improve performance.

2. Research methods

Low-density polyethylene (LDPE) plastic is commonly used to make goods that require flexibility but are strong. This type is indestructible but safe for storing food (food grade). Commonly used for food wrap, bread wrap, and dry-cleaning bags, The level of hazard posed is low, but the difficulty of decomposing with nature is categorized as moderate [9]. Fig. 1 shows the LDPE Plastic (a) and Shredded plastic result (b).

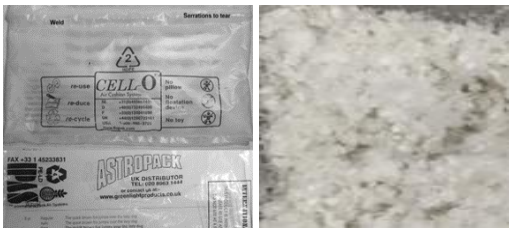

(a) (b)

Figure 1. (a) LDPE plastic; (b) Shredded plastic result

The filament of LDPE plastic waste is physically white, as shown in Fig. 2. The shape of LDPE plastic waste is classified as irregular and also a sponge. The shape is caused by the process of making it using a chopping machine.

The results were then extruded using an extruder machine with a motor speed of 72 rpm and a rolling speed of 54 rpm at a nozzle size of 1.75 mm. Six samples were made for each extruder machining process with various variables. The variables in the analysis are temperature, 170 °C, 180 °C, 190 °C, 200 °C, 210 °C, and 220 °C. The results of the extrusion can be seen in Fig. 2.

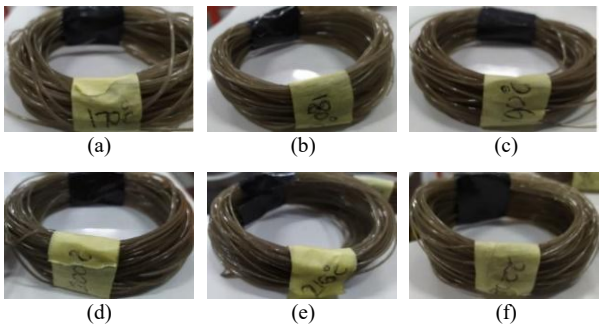

(a) (b) (c)

(d) (e) (f)

Figure 2. Samples of LDPE plastic (a) 170 °C, plastic (b) 180 °C, (c) 190 °C, (d) 200 °C, (e) 210 °C, (f) 220 °C

Samples of LDPE plastic products have different dimensions depending on the nozzle diameter of the extrusion machine. The nozzle diameter on the extrusion machine used is 1.75 mm. Changes in diameter after undergoing the machining process on the extrusion machine are shown in Table 1.

Table 1. Machining process data on extrusion machine

No.	Temperature (°C)	Extrusion time (minutes)	Nozzle diameter (mm)	Sample diameter (mm)
1	170	29.06	1.75	1.6
2	180	29.04	1.75	1.4
3	190	29.02	1.75	1.4
4	200	28.57	1.75	1.3
5	210	28.49	1.75	1.2
6	220	28.01	1.75	1.1

From Table 1 increasing temperatures (170 °C, 180 °C, 190 °C, 200 °C, 210 °C, and 220 °C) will reduce machining process time and decrease sample diameter. The largest diameter value is at a temperature of 170 °C. 1.6 mm with a time of 29.06 minutes, and the smallest diameter value is at a temperature of 220 °C, which is 1.1 mm with a time of 28.01 minutes. As a result, at a temperature of 220 °C, the diameter of the samples is significantly smaller. This is because the heat input is getting larger. Furthermore, thermal softening occurs, where the plastic melts faster.

The test sample that has been obtained is then subjected to a hardness study to determine the hardness of LDPE plastic waste after extrusion. A durometer, also known as ashore, is used to perform an International Standard Test. This test uses a digital Shore A Durometer Hardness test tool to determine the hardness value of a material. In this case, the ability of the material to be loaded with an iron indenter measuring 0.79 mm and having a geometric shape in the form of a flat cone point, with a hardness range of 0 to 100 HA. Durometers have various types of scales where the use of the scale is based on the type of specimen being tested and the level of hardness of the specimen being tested.

The available durometer scale in the materials laboratory is shore A, B, and D. Shore A is used for specimens with hardness values between 20 to 90, such as soft rubber and natural rubber. On the other hand, shore B and shore D are used for specimens with hardness values above 90. In this study, the shore used was shore A because the specimen tested had a hardness value below 90. The assumption that can be made is based on research conducted by Cheung and Zhang that the material used for orthotic shoe insoles usually has a hardness value of between 30 to 50 The unit of hardness value in this study is HA which means the Hardness of Shore A or hardness value using Shore A. Fig. 3 shows the LDPE Plastic shore a durometer hardness testing.

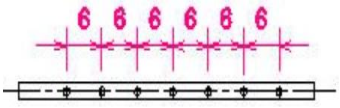

Figure 3. LDPE plastic shore a durometer hardness testing (ASTM D2240)

Hardness value data collection on the results of the LDPE plastic waste sample is studied by testing the hardness at 7 points along the horizontal line of the specimen. As shown in Figure 4, the distance from the point to the next point is 6 mm. The change in these properties will not be significant if it is not accompanied by changes in the microstructure of the LDPE plastic. To find this, a scanning Electron Microscopy test analysis was used. And the detector used for analysis is the backscatter electron because this detector can distinguish different phases/elements by showing differences in color intensity.

A scanning electron microscope (SEM) is a type of electron microscope that is used to look at the surface of solid objects. SEM magnification ranges from 10–3,000,000 times, depth of field ranges from 4–0.4 mm, and resolution ranges from 1–10 nm. SEM is widely used for research and industrial reasons because it combined high magnification, large depth of field, good resolution, ability to know composition, and crystallographic information [10].

3. Results and discussion

3.1. Shore a durometer hardness testing

The results of the hardness test were carried out on samples of LDPE plastic waste. The results of the test on temperature variations using the hardness of Shore A or hardness values using Shore A are presented for each specimen. A hardness test is carried out on the horizontal plane with 7 points. The specimen with the highest hardness was at a temperature of 210 °C with an average hardness of 86.57 HA. The specimen with the lowest hardness was at a temperature of 180 °C with an average hardness of 66.07 HA. Table 2 shows the result of the hardness test.

Fig. 4 shows the overall hardness distribution of temperature variations. It can be seen that the maximum temperature that occurs in the extrusion process of LDPE plastic waste affects the maximum hardness value. The higher the maximum temperature, the more even the distribution of hardness values. This can be seen at temperatures of 210 °C and 220 °C.

Fig. 5 shows that the hardness of the 180 °C specimens has the lowest hardness value compared to the 170 °C and 190 °C temperature specimens. The highest hardness value for specimens at 170 °C is 76.5–8.5 HA. On the other hand, the specimen temperature is 190 °C with a hardness value of 66.5–78.5 HA.

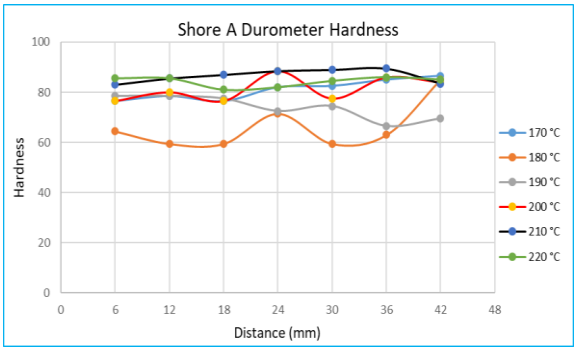

Figure 4. LDPE plastic hardness distribution

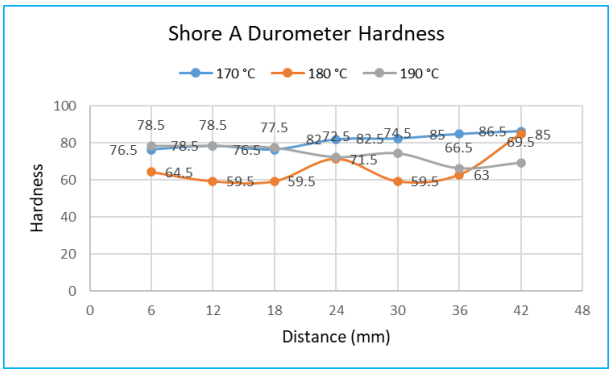

Figure 5. LDPE plastic hardness distribution at temperatures 170 ºC, 180 ºC, and 190 ºC

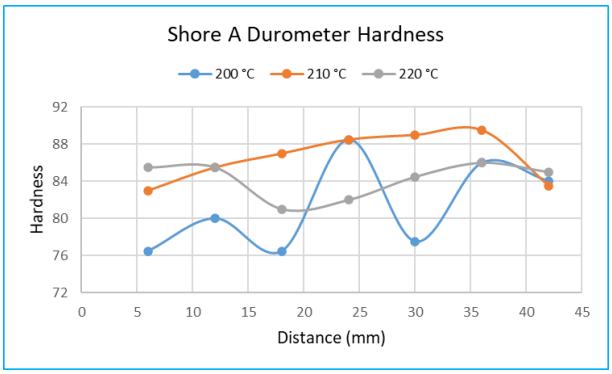

Figure 6. LDPE plastic hardness distribution at temperatures 200 ºC, 210 ºC, and 220 ºC

Fig. 6 shows that the hardness of the 210 °C specimens has the highest hardness value range compared to the 200 °C and 220 °C temperature specimens. Specimen hardness at a temperature of 210 °C, which ranges from 83 to 89.5 HA. Meanwhile, at 200 °C, the highest hardness is in the range of 76.5–86 HA. Similarly, the specimen temperature was 220 °C and the highest hardness ranged from 81–85.5 HA. Table 2 shows the hardness test result data on LDPE plastic waste samples.

The hardness of the specimen temperature at a temperature of 210 °C is very high due to a decrease in the temperature of the amorphous content in the material. According to Asror M. F., amorphous content is brittle and hard [11]. From the graph of the hardness distribution of Shore A Durometer, the high temperature in the process of making LDPE plastic waste extrusion specimens greatly affects the hardness value obtained. The higher the extrusion process temperature, the lower the hardness value.

This is due to the difference in hardness values in each test because of a speed that is too slow, which causes the material to freeze first. In addition, this is caused by the uneven distribution of temperature. Another variable is that many possible extrusion processes in the extrusion machine, such as Nozzle temperature, coolant, workbench temperature, as well as nozzle path, and speed are important for processing variables that affect the performance of the final molded part.

Table 2. Hardness test results data for LDPE plastic waste samples

Point number	Point distance (mm)	Hardness (HA)					
		170 °C	180 °C	190 °C	200 °C	210 °C	220 °C
1	6	76.5	64.5	78.5	76.5	83	85.5
2	12	78.5	59.5	78.5	80	85.5	85.5
3	18	76.5	59.5	77.5	76.5	87	81
4	24	82	71.5	72.5	88.5	88.5	82
5	30	82.5	59.5	74.5	77.5	89	84.5
6	36	85	63	66.5	86	89.5	86
7	42	86.5	85	69.5	84	83.5	85
Average		81.07	66.07	73.93	81.29	86.57	84.21

3.2. Microstructure testing using SEM

There are elements that makeup LDPE plastic, such as calcium (Ca), silicon (Si), and oxygen. This is due to the migration process of atoms in the material in gas, liquid, and solid conditions at hot temperatures, which is called diffusion [12]. Through the diffusion of LDPE liquid plastic, it is possible to produce a new bonding phase in other elements. Morphological analysis using SEM in the extrusion process with a temperature of 170 °C for 29.06 minutes is shown in Fig. 7.

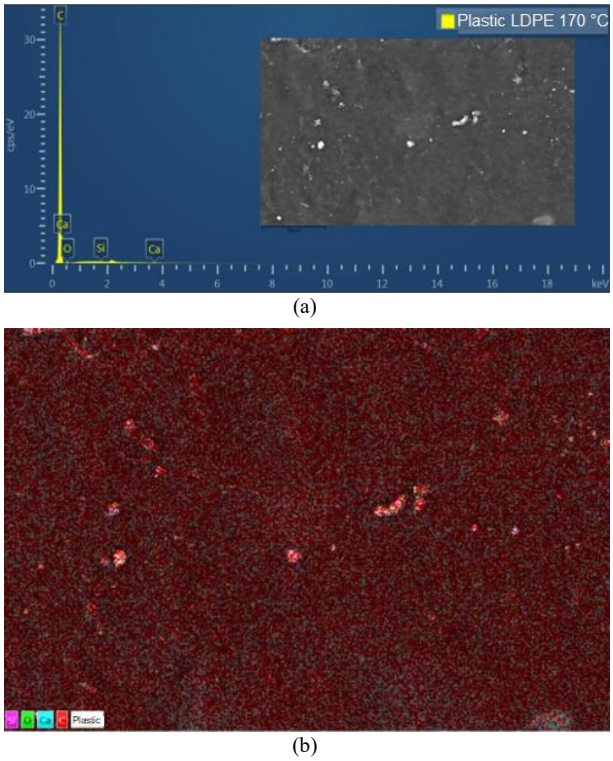

(a)

(b)

Figure 7. EDX analysis results at a temperature of 170 °C (a) Composition LDPE 170 °C, (b) EDS layered 170 °C

Fig. 8 shows the presence of other elements such as sodium (Na), aluminum (Al), and magnesium (Mg) in the EDX SEM test at 500X magnification and the presence of sodium and aluminum only.

Figs. 8 and 9 show the high amounts found in the element carbon, which is the main building block of plastics. The presence of other elements at temperatures of 180 °C and 190 °C is due to the possibility of mixing other materials from waste containing elements of magnesium, aluminum, and sodium during the LDPE plastic waste counting process until the end of mixing in the extruder machine.

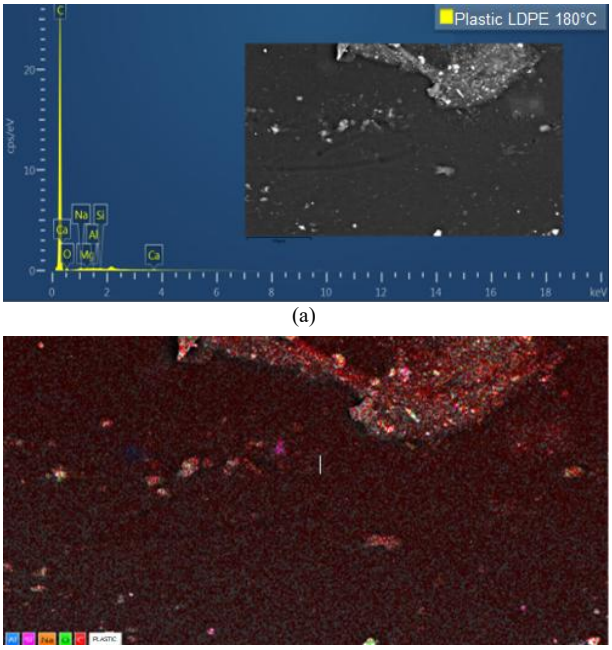

(a)

(b)

Figure 8. EDX analysis results at a temperature of 180 °C; (a) Composition LDPE 180 °C; (b). EDS layered 180 C

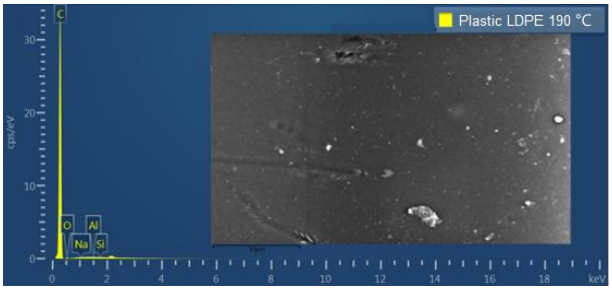

Figure 9. EDX analysis results at a temperature of 190 °C

The observation of the microstructure using SEM for LDPE with a magnification of 500 times, as shown in Fig. 10, it appears that the plastic particles bind to each other. But here, it looks like space or air cavities (pores).

In Fig. 11, the results of the EDX analysis at a temperature of 210 °C allow it to produce a new bonding

phase in other elements, new nuclear nucleation, and the presence of empty spaces (pores).

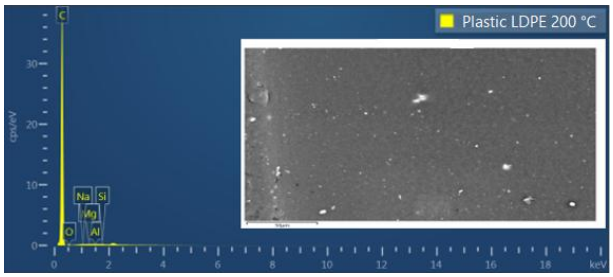

Figure 10. EDX analysis results at a temperature of 200 °C

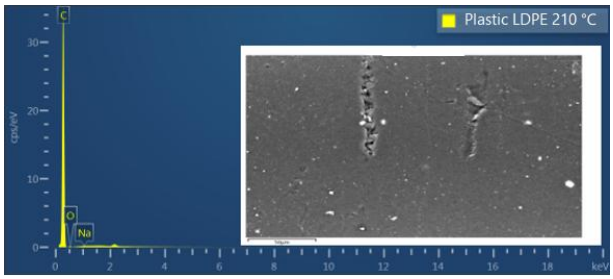

Figure 11. EDX analysis results at a temperature of 210 °C

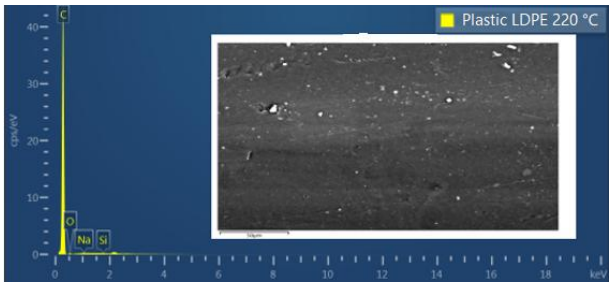

Figure 12. EDX analysis results at a temperature of 220 °C

The presence of empty spaces (pores) shown in Fig. 12 occurred during the extrusion process. In addition, the occurrence of unwanted oxidation cannot be avoided. In addition, it shows that high amounts are found in the element carbon as the main constituent material, along with other materials such as oxygen (O), sodium (Na), and silicon (Si). Based on the results of macrostructural photo testing on the extrusion results of LDPE plastic waste, obtained data on the area (plastic deformation) using image J software, on specimens at 170 °C, 180 °C, 190 °C, 200 °C, 210 °C, and 220 °C. In general, it has additional grooves that are different from other specimens. The pictures of the microstructure of LDPE plastic waste can be seen in Fig. 13.

The filament strengthening of the elements is homogeneously distributed over the entire surface, but there are also clearly visible morphological differences between different temperatures. The possible formation of these different phases is influenced by the rate of diffusion, which is explained by Fick's law. It explains that as the temperature increases, the rate of diffusion also increases.

As a result, the diffusion that occurs between the carbon matrix and other elements, such as liquid, occurs completely. After extrusion molding on samples, LDPE plastic shows good bonding to other elements, which melt well and permeate each other [13].

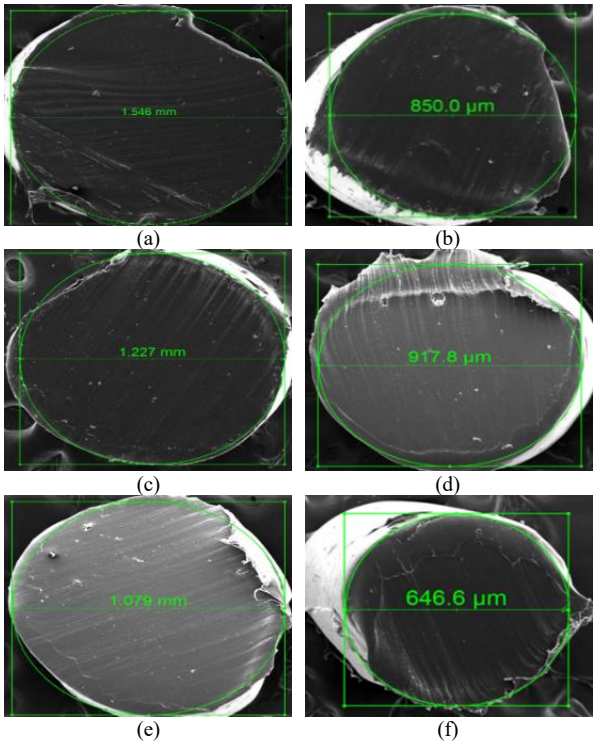

Figure 13. Microstructure using SEM in temperature of (a) 170 °C; plastic (b) 180 °C; (c) 190 °C; (d) 200 °C; (e) 210 °C; (f) 220 °C

In addition, as can be seen in Fig. 13, the diameter size of LDPE plastic is different for each temperature variation. The different diameters formed were caused by the heat generated by the extrusion process of the LDPE plastic sample. In addition, other parameters are the addition of the load (compressive force) and the speed and heating that occur in the engine and nozzle. These parameters resulted in softening, which undergoes deformation and forms a diameter. These different diameter shapes indicate that a disturbance occurs during the extrusion process. This is most likely due to the partial cooling of the melted LDPE plastic waste as it travels from the extruder head to the nozzle itself [13].

Figure 14 shows the surface of LDPE semi-micro plastic with a different surface for each variation of the test.

At temperature variations of 170 °C, 180 °C, and 190 °C, the surface looks not so flat, while at temperatures of 200 °C, 210 °C, and 220 °C, it looks like a neat surface. The presence of different-sized granules in each variation of the test (differences in surface morphology) because the complex viscosity describes the presence of flow resistance in a material [14]. The viscosity at higher temperatures also contributes to a constant increase in the melt flow of the material. Therefore, it can be concluded that the physical state of the polymer depends on the temperature. The polymer determines its response to heat, which is very important for the extrusion molding parameters [15].

It also shows morphologically that a small amount of crystal nucleation occurs before the polymer melt enters

the print head nozzle section. However, this is most likely due to the partial cooling of the LDPE plastic melt as it travels from the extruder head to the nozzle and cannot be attributed to the nucleation effect itself.

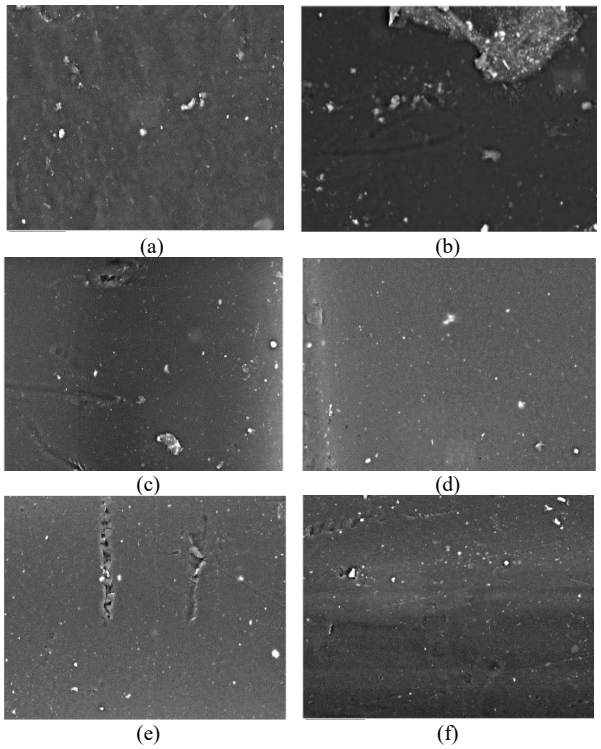

Figure 14. SEM-micro plastic LDPE (a) 170 °C; plastic (b) 180 °C; (c) 190 °C; (d) 200 °C; (e) 210 °C; (f) 220 °C

Extrusion nozzle temperature, coolant speed, and nozzle path and speed are important processing variables that affect the performance of the final molded part.

4. Conclusion

The specimen temperature of 210 ℃ had the highest hardness value, which was in the range of 83 – 89.5 HA, while the specimen temperature of 180 ℃ has the lowest hardness value ranging from 59.5 to 71.5 HA. The higher the temperature, the higher the hardness value in the manufacturing process (extrusion). Higher extrusion nozzle temperatures lead to better melt fluidity and formability of the impression material. Higher temperatures produce more energy which increases infiltration and diffusion between deposited filaments. The high temperature in the LDPE Plastic Waste Extrusion process; greatly affects the hardness value, but if the higher temperature also allows a decrease in the hardness value, this is due to the many process parameters that affect the printing machine, (waste extrusion process) namely nozzle temperature, speed cooling of the rolling, as well as the path and speed of the nozzles. Extrusions are important processing variables that affect the performance of the final molded part.

References

[1] C.-F. Chow, W.-M. W. So, T.-Y. Cheung, and S.-K. D. Yeung, “Plastic Waste Problem and Education for Plastic Waste Management,” *Emerg. Pract. Scholarsh. Learn. Teach. a Digit. Era*, pp. 125–140, 2017, doi: 10.1007/978-981-10-3344-5_8.

[2] R. Geyer, J. R. Jambeck, and K. L. Law, “Production, use, and fate of all plastics ever made,” *Sci. Adv.*, vol. 3, no. 7, Jul. 2017, doi: 10.1126/sciadv.1700782.

[3] L. Techawinyutham, J. Tengsuthiwat, R. Srisuk, W. Techawinyutham, S. Mavinkere Rangappa, and S. Siengchin, “Recycled LDPE/PETG blends and HDPE/PETG blends: mechanical, thermal, and rheological properties,” *J. Mater. Res. Technol.*, vol. 15, pp. 2445–2458, Nov. 2021, doi: 10.1016/j.jmrt.2021.09.052.

[4] L. B. Variya, M. Bhavik, P. Harshil, P. Jenish, and G. Hardik, “Plastic Extruder Machine,” vol. V, no. 02, pp. 53–54, 2018.

[5] M. L. Sonjaya and M. F. Hidayat, “Construction and Analysis of Plastic Extruder Machine for Polyethylene Plastic Waste,” *EPI Int. J. Eng.*, vol. 3, no. 2, pp. 132–137, Jan. 2021, doi: 10.25042/epi-ije.082020.07.

[6] D. Vaes and P. Van Puyvelde, “Semi-crystalline feedstock for filament-based 3D printing of polymers,” *Prog. Polym. Sci.*, vol. 118, p. 101411, 2021, doi: 10.1016/j.progpolymsci.2021.101411.

[7] N. V. Raghavaiah, “Methodology of RMA-4 Rubber Hardness Testing using IRHD and Shore-A Methods,” *Int. J. Res. Eng. Sci. Manag.*, vol. 2, no. 6, pp. 515–516, 2019.

[8] O. P. Choudhary and P. Ka, “Scanning Electron Microscope: Advantages and Disadvantages in Imaging Components,” *Int. J. Curr. Microbiol. Appl. Sci.*, vol. 6, no. 5, pp. 1877–1882, May 2017, doi: 10.20546/ijcmas.2017.605.207.

[9] N. Mills and M. Jenkins, *Plastics Microstructure and Engineering Applications*, 3rd ed. Oxford: Butterworth-Heinemann - Elsevier, 2005.

[10] P. P. Pednekar, S. C. Godiyal, K. R. Jadhav, and V. J. Kadam, “Mesoporous silica nanoparticles: a promising multifunctional drug delivery system,” in *Nanostructures for Cancer Therapy*, Elsevier, 2017, pp. 593–621. doi: 10.1016/B978-0-323-46144-3.00023-4.

[11] M. F. A. dan H. S. S. Tomo, “Pengaruh suhu proses dan tekanan injection moulding terhadap kekuatan benturan dan kekerasan pada material High density polyethylene. Prosiding symposium nasional polimer IV Sentra Teknologi Polimer (STP)- BPPT, 188-192.,” *Pros. Simp. Nas. Polim.*, vol. IV, pp. 188–192, 2003.

[12] W. D. Callister Jr. and D. G. Rethwisch, *Material Science and Engineering an Introduction*, 10th ed. United States of America: John Wiley & Sons, Inc, 2018.

[13] Y. Tao, M. Liu, W. Han, and P. Li, “Waste office paper filled polylactic acid composite filaments for 3D printing,” *Compos. Part B Eng.*, vol. 221, no. May, p. 108998, 2021, doi: 10.1016/j.compositesb.2021.108998.

[14] P. WANG, B. ZOU, S. DING, L. LI, and C. HUANG, “Effects of FDM-3D printing parameters on mechanical properties and microstructure of CF/PEEK and GF/PEEK,” *Chinese J. Aeronaut.*, vol. 34, no. 9, pp. 236–246, Sep. 2021, doi: 10.1016/j.cja.2020.05.040.

[15] P. Olesik, M. Godzierz, and M. Kozioł, “Preliminary Characterization of Novel LDPE-Based Wear-Resistant Composite Suitable for FDM 3D Printing,” *Materials (Basel).*, vol. 12, no. 16, p. 2520, Aug. 2019.